Chem Soc Rev

Research progress of perovskite materials in photocatalysis- and photovoltaics-related energy conversion and environmental treatment

Journal:	*Chemical Society Reviews*
Manuscript ID:	CS-SYN-02-2015-000113.R2
Article Type:	Review Article
Date Submitted by the Author:	09-Apr-2015
Complete List of Authors:	Wang, Wei; Curtin University, Chemical Engineering Shao, Zongping; nanjing tech univ, chemical engineering; curtin univ, chemical engineering

SCHOLARONE™
Manuscripts

Chemical Society Reviews RSCPublishing

REVIEW ARTICLE

Research progress of perovskite materials in photocatalysis- and photovoltaics-related energy conversion and environmental treatment

Wei Wang[a] and Zongping Shao*[a,b]

Cite this: DOI: 10.1039/x0xx00000x

Received 00th January 2012,
Accepted 00th January 2012

DOI: 10.1039/x0xx00000x

www.rsc.org/

Meeting the growing global energy demand is one of the important challenges of the 21st century. Currently over 80% of the world's energy requirement is supplied by the combustion of fossil fuels, which promotes global warming and has deleterious effects on our environment. More seriously, fossil fuels are non-renewable energy and will eventually be exhausted due to the high consumption rate. A new type of alternative energy that is clean, renewable and inexpensive is urgently needed. Several candidates are currently available, such as hydraulic power, wind force and nuclear power. Solar energy is particularly attractive because it is essentially clean and inexhaustible. A year's worth of sunlight provides more than 100 times the energy of the world's entire known fossil fuel reserves. Photocatalysis and photovoltaics are two of the most important routes for the utilization of solar energy. However, environmental protection is also critical to realize a sustainable future, and water pollution is a serious problem of current society. Photocatalysis is also an essential route for the degradation of organic dyes in wastewater. A type of compound with the defined structure of perovskite (ABX_3) was observed to play important roles in photocatalysis and photovoltaics. These materials can be used as photocatalysts for water splitting reaction for hydrogen production and photo-degradation of organic dyes in wastewater as well as for photoanodes in dye-sensitized solar cells and light absorbers in perovskite-based solar cells for electricity generation. In this review paper, the recent progress of perovskites for applications in these fields is comprehensively summarized. A description of the basic principles of water splitting reaction, photo-degradation of organic dyes and solar cells as well as the requirements for efficient photocatalysts is first provided. Then, emphasis is placed on the designation and strategies for perovskite catalysts to improve their photocatalytic activity and/or light adsorption capability. Comments on current and future challenges are also provided. The main purpose of this review paper is to provide a current summary of recent progress in perovskite materials for use in these important areas and to provide some useful guidelines for future development in these hot research areas.

1. Introduction

A sustainable energy supply and environmental protection are two of the most important issues in the development of our future world. Our current society relies too heavily on fossil fuels for its energy supply, and the low-efficiency power generation from burning fossil fuels produces a large amount of carbon dioxide, which causes a significant greenhouse effect. In addition, the sulfur and nitrogen impurities in fossil fuels will eventually be converted into SO_x and NO_x during combustion, which is released into the atmosphere and causes significant environmental problems. As non-renewable natural resources, fossil fuels will not be sustainable by the next century due to the high consumption rate. To achieve the sustainability of our society, the development of alternative renewable energies to replace fossil fuels is of great importance. Among these alternative energy sources, solar energy is particularly attractive due to its abundance, easy accessibility and cleanliness. In fact, there are approximately 3,850,000 exajoules (EJ) of solar power irradiating the Earth per year. If only 1% of the solar energy could be utilized, it would meet the energy demand of human beings at the current consumption rate of energy. The widespread utilization of solar energy may then increase the world's energy security by enhancing sustainability, reducing pollution, lowering the costs of mitigating climate change and reducing the dependence on fossil fuels. Recently, the direct utilization of solar energy, such as solar heating, solar photovoltaics and photocatalysis and solar thermal electricity, has attracted considerable and increasing attention.[1-5] However, to date, humans consume only 539 EJ globally per year, which

is only approximately 0.014% of the total solar energy reaching the Earth. It is thus necessary to develop new approaches that can directly utilize solar energy with improved efficiency. However, organic waste pollution has become a serious problem because many organic wastes are toxic, resulting in a detrimental effect to the ecological environment. The conversion of wastewater into harmless and readily disposable water is of significant importance for a sustainable future.

Photocatalysis and photovoltaics are two of the most important routes for the utilization of solar energy, and photocatalysis is also an important route for the degradation of organic wastes in water into harmless substances. The photocatalytic activity depends on the capability of the catalyst to create electron-hole pairs, which generate free radicals capable of undergoing secondary reactions. The discovery of water electrolysis by TiO_2 resulted in several potential practical applications using photocatalysis such as the conversion of water into hydrogen by photocatalytic water splitting and the decontamination of water using photocatalysis.[6-9] The efficiency of photocatalysis for both hydrogen production from water electrolysis and organic degradation strongly relies on the catalyst itself. Recently, excellent catalysts were developed to increase the efficiency of organic reduction through photocatalysis and hydrogen production from water electrolysis.[10-13] Some perovskites were observed to exhibit high activity for photocatalysis, both in wastewater treatment and water electrolysis.[14-17]

Photovoltaic is a method for converting solar radiation into electricity using semiconductors with a photovoltaic effect. The first solar cell was constructed in 1883, and the silicon solar cell was created in 1954 with efficiencies of 4.5-6%. The field of solar cells can be divided into three generations. The first generation of solar cells was based on a single p-n junction of crystalline Si with a maximum conversion efficiency of 25% in the lab, but the theoretical limit of the energy conversion efficiency (η) is 31% for single-crystalline Si cells and was predicted by a thermodynamic calculation performed by Shockley and Queisser (S-Q).[18] Although exhibiting a relatively high efficiency, these materials suffer from high manufacturing and installation costs. The second generation of solar cells included the use of amorphous silicon, polycrystalline silicon or microcrystalline silicon, cadmium telluride or copper (gallium) indium selenide/sulfide. These solar cells were significantly less expensive than single-crystalline solar cells due to reduced materials and processing costs and increased manufacturing throughput. The efficiencies of these cells were generally lower than those of the first-generation solar cells.[2,19] The third generation of solar cells, developed over the last decade, aim at conversion efficiencies beyond the S-Q limit of 31%.[20-23] The third-generation solar cells are broadly defined as semiconductor devices, which could be configured as thin films deposited on supporting substrates or as nanocrystal quantum dots. The third-generation solar cells aim at maintaining high solar energy conversion efficiencies at lower costs using cost-effective fabrication techniques such as spin coating, spray coating and printing because manufacturing solar cells using conventional semiconductors such as single-crystal silicon is expensive and energy consuming. In the third-generation solar cells, dye-sensitized solar cells (DSSCs) have recently attracted increasing attention; these solar cells achieve optical absorption and the charge separation processes through the association of a sensitizer as a light-absorbing material with a wide band gap (BG) semiconductor of nanocrystalline morphology. Compared with a silicon-based solar cell, the price could be significantly reduced. In DSSCs, the photoanode is highly important, which is determined by the band gap energy (E_{bg}) of the semiconductors, placing a fundamental upper limit on the solar energy conversion efficiency. Recently, a type of compound with the defined structure of perovskite, which was initially named for the mineral $CaTiO_3$, was observed to play important roles in photocatalysis and photovoltaics. These materials can be used as photocatalysts for the water splitting reaction to produce hydrogen and the photo-degradation of organic dyes in wastewater as well as for photoanodes in DSSCs and light absorbers with the development of a certain type of solar cell, called a perovskite-based solar cell.

In this review paper, the recent progress in perovskites for applications in photocatalysis and photovoltaics reactions is comprehensively summarized. Emphasis is placed on the designation and strategies of the perovskite catalysts to improve the photocatalytic activity and/or light adsorption capability. In Section 1, a brief introduction of photocatalysis and photovoltaics reactions is presented. In Section 2, the operation principles and mechanism of the water splitting reaction, the degradation of organic dyes and perovskite-based solar cells as well as the origin and structural properties of the perovskite materials is presented. In Section 3, the recent developments and strategies about design the perovskite catalysts for photocatalysis reactions, such as the water splitting reaction and degradation of organic dyes under visible light, is extensively reviewed. In Section 4, the application of perovskites in photovoltaics devices, mainly as light absorbers and photoanodes in solar cells, is described. We focus not only on the design of the catalysts that have recently been studied in depth but also on the relationship between the photocatalytic activity and the solid-state properties. The methodologies used to improve the photoactivity and light-adsorption capability of the perovskites, such as A-site and/or B, X-site doping and composite catalysts, are extensively reviewed. Finally, in Section 5, some conclusions are derived and perspectives for the research in perovskite materials in the photocatalytic and photovoltaic reactions are suggested. This review aims to provide some useful guidelines for the further development of highly active and visible-light sensitive perovskite materials for various photocatalysis and photovoltaics reactions by directly utilizing solar energy.

2. Fundamental understanding

2.1 Photophysics and photochemistry in environmental treatment and energy conversion

2.1.1 Water splitting reactions

Hydrogen is believed to be one of the most important clean fuels for the future. The success of a so-called hydrogen economy relies heavily on finding an effective route for the mass production of hydrogen with practical importance. The photocatalytic water splitting reaction using sunlight has been extensively exploited as a potential route for the mass production of hydrogen from renewable sources (solar energy and water) over recent decades,[24-26] as stimulated by the first discovery in 1967 of Honda and Fujishima, who demonstrated that overall water splitting can be achieved using a photoelectrochemical cell consisting of a single-crystalline TiO_2 (rutile) anode and a Pt cathode under ultraviolet (UV)

 This journal is © The Royal Society of Chemistry 2012

irradiation and an external bias. To date, many metal oxide photocatalysts capable of splitting water under UV light irradiation have been discovered.[27-30] In the earlier reviews of the water splitting reaction using semiconductor catalysts, some basic principles were demonstrated.[3,31,32] Fig. 1 presents a schematic illustration of the basic principle of the water splitting reaction on a heterogeneous photocatalyst.[31] In these photocatalytic materials, electrons in the valence band (VB) are excited to the conduction band (CB) by irradiating light with energy equivalent to or larger than the BG; subsequently, electron-hole pairs are formed. These photo-generated electrons and holes could directly contribute to the reactions of reducing protons to generate H_2 and oxidizing H_2O to produce O_2, respectively.[3,31,32]

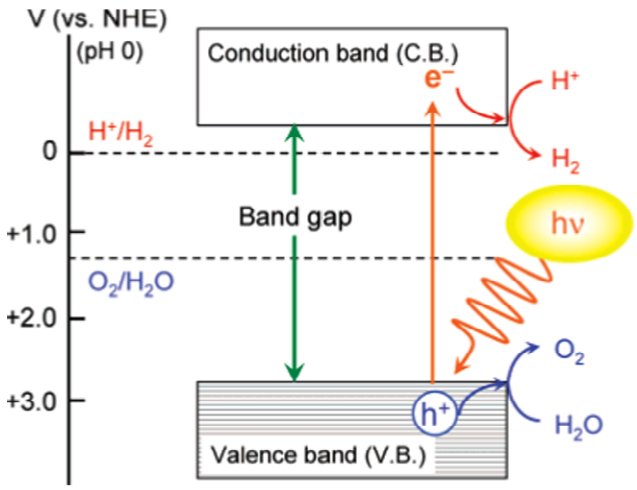

Fig. 1 Basic principle of overall water splitting on a heterogeneous photocatalyst. Reproduced with permission from ref. 31. Copyright 2007, American Chemical Society.

To facilitate the water splitting reaction, the bottom of the CB and the top of the VB must be lower and higher than the oxidation-reduction potentials (ORPs) of H^+/H_2 (0 V vs. normal hydrogen electrode (NHE)) and O_2/H_2O (+1.23 V vs. NHE), respectively. Therefore, the minimum photon energy thermodynamically required to drive the reaction is 1.23 eV, which corresponds to a wavelength of approximately 1000 nm in the near-infrared region (λ=1240/E_{bg}). However, in experiments for many metal oxides, where the VB is mainly composed of O 2p orbitals, the top of the VB takes its position at a potential much higher than +1.23 V vs. NHE. Therefore, the ORPs of H^+/H_2 and O_2/H_2O are likely to be sandwiched between the top of the VB and the bottom of the CB, as illustrated in Fig. 1. The requirement for the much greater photon energy than the BG of the photocatalyst is due to the existence of an activation barrier in the charge-transfer process between the photocatalyst and water molecules. In addition, these materials can respond only to UV light because of the much wider BG. As the main component of the solar spectrum (approximately 50%) consists of visible photons ($400 < \lambda < 800$ nm), a primary goal of the photocatalytic water splitting reaction is to efficiently utilize visible light.

The photocatalytic water splitting can be morphologically divided into two types, i.e., using particulate photocatalysts and photoelectrochemical cells with photocatalytic electrodes. Since the development of the first photoelectrochemical cell by Honda and Fujishima, which was comprised of TiO_2 and Pt electrodes, numerous photoelectrochemical cells have been designed specifically for the efficient utilization of solar energy. As illustrated in Fig. 2a, electrons and holes are generated by irradiating the TiO_2 electrode with UV light;[33] the photogenerated electrons then reduce water to form H_2 on a Pt counter electrode while holes oxidize water to form O_2 on the TiO_2 electrode with some external bias by a power supply or pH difference between the electrolyte region near the cathode and anode. In another study, Anpo and co-workers succeeded in the separative evolution of H_2 and O_2 using a two-compartment cell (Fig. 2b) under light irradiation using a TiO_2 thin-film photocatalyst to avoid the possible explosion of the generated H_2 and O_2 in the same chamber.[34] However, due to the lack of suitable photoelectrode materials with appropriate BG and stability, the systems proposed to date have been developed into complicated integrated multilayer and tandem systems, which could increase the overall cost of the water splitting system.[35]

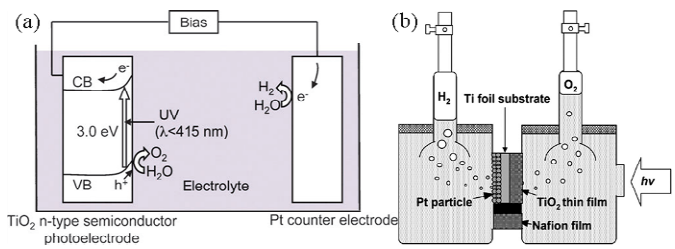

Fig. 2 (a) Honda-Fujishima effect-water splitting using a TiO_2 photoelectrode. Reproduced with permission from ref. 33. Copyright 2009, Royal Society of Chemistry. (b) H-Type glass container for the separate evolution of H_2 and O_2 using a TiO_2 thin film photocatalyst device (TiO_2 side, 1.0 M NaOH aq.; Pt side, 0.5 M H_2SO_4 aq.). Reproduced with permission from ref. 34. Copyright 2007, Elsevier Inc.

However, many solid materials have also been developed to date as photocatalysts for water splitting. Sunshining at photocatalyst powders dispersed in a water pool leads to the cogeneration of hydrogen and oxygen. Compared with the photoelectrochemical cell configuration, the pulverized photocatalyst systems are advantageous for the large-scale application of solar water splitting due to their simplicity. Thus, the design of pulverized photocatalysts is of great importance to achieve the water splitting reaction for near-future practical applications.

To develop suitable catalysts for the water splitting reaction, the steps involved in the water splitting reaction with the semiconductor photocatalysts should be well understood. It is generally accepted that there are three steps in the reactions, which have been well described in some excellent reviews.[3,31,32] As illustrated in Fig. 3, the three steps are as follows: (1) the photocatalyst absorbs photon energy equal or greater to the E_{bg} of the catalyst and generates photoexcited electron-hole pairs in the bulk; (2) the photo-excited carriers separate and migrate to

the surface without recombination; and (3) the adsorbed species are reduced and oxidized by the photogenerated electrons and holes to produce H_2 and O_2, respectively. The first two steps are highly dependent on the structural and electronic properties of the photocatalyst.[31] In general, high crystallinity has a positive effect on activity because the density of defects, which act as recombination centers between photogenerated carriers, decreases with increasing crystallinity. The third step is affected by the amount of active sites and the activation energy for gas evolution. Sometimes, this step is promoted by the presence of a solid co-catalyst, which is typically a noble metal or metal oxide deposited onto the photocatalyst surface as a dispersion of nanoparticles. It is thus important to carefully design both the bulk and surface properties of the material to obtain high photocatalytic activity for this reaction.

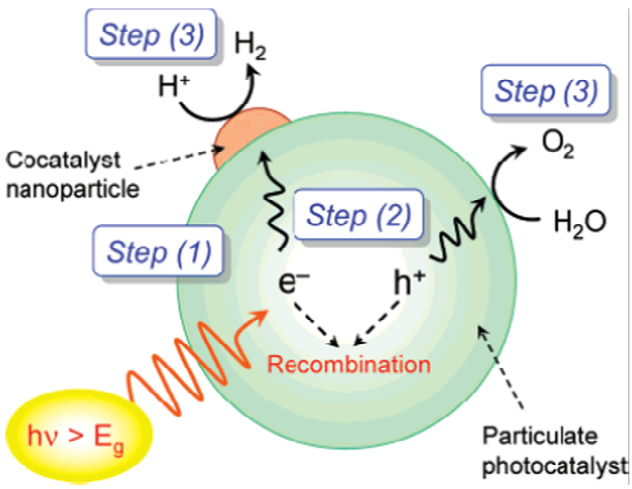

Fig. 3 Processes involved in photocatalytic overall water splitting on a heterogeneous photocatalyst. Reproduced with permission from ref. 31. Copyright 2007, American Chemical Society.

2.1.2 Degradation of organic dyes in wastewater treatment

The increasing demand and shortage of clean water sources due to the rapid development of industrialization, rapid population growth and long-term droughts have become important issues worldwide. Various practical strategies and solutions have been adopted to yield more viable water resources. The recycling of wastewater is considered key to solving the problem of water shortage. However, the presence of toxic organic compounds, such as organic dyes, phenols and pesticides, in wastewater and the associated environmental hazards have recently raised numerous concerns.[36-38] In this review paper, we will focus on only the degradation reactions of different dyes in the wastewaters because organic dyes are one of the largest groups of pollutants released into wastewaters from textile and other industrial processes. The removal and degradation of organic dyes has been a matter of considerable interest, and some purification methods have been developed. Traditional physical techniques, such as adsorption on activated carbon, ultrafiltration, coagulation by chemical agents and ion exchange on adsorbents, have been widely used for the removal of dye pollutants.[39,40] However, these methods succeed only in transferring organic compounds from water to another phase, creating secondary pollution. Additional steps, such as a further treatment of solid wastes and regeneration of the adsorbent, are required, which will add additional cost to the purification process. Furthermore, Forgacs et al. noted that traditional wastewater treatment technologies are ineffective for handling dye wastewater because of the chemical stability of these pollutants.[41] The heterogeneous photocatalytic oxidation process, using semiconductor catalysts such as TiO_2 and UV or visible light, has demonstrated promising results for the degradation of organic dyes and produces more biologically degradable and less toxic substances. Tremendous efforts have been devoted to the use of photocatalysis in the removal of dyes from wastewaters.[42-46]

The photocatalytic oxidation process is activated by the absorption of a photon with sufficient energy (equal or greater to E_{bg} of the semiconductor catalyst), and then, a charge separation occurs due to the promotion of an electron (e^-) from the VB of the semiconductor catalyst to the CB. Thus, a hole (h^+) in the VB is generated.[4] In this reaction, h^+ and e^- are powerful oxidizing and reductive agents, respectively. The positive hole oxidizes either the pollutant directly or water to produce OH· radicals and the electron in the CB reduces the oxygen adsorbed on the photocatalyst.[4] The activation of the semiconductor by light can be represented by the following steps, as proposed by Chong et al.:[4]

Photoexcitation:

$$photocatalyst + h\nu \rightarrow e^- + h^+ \quad (1)$$

Charge-carrier trapping of e^-:

$$e^-_{CB} \rightarrow e^-_{TR} \quad (2)$$

Charge-carrier trapping of h^+:

$$h^+_{VB} \rightarrow h^+_{TR} \quad (3)$$

Electron-hole recombination:

$$e^-_{TR} + h^+_{VB}(h^+_{TR}) \rightarrow e^-_{CB} + heat \quad (4)$$

Photoexcited e^- scavenging:

$$(O_2)_{ads} + e^- \rightarrow O_2^{\bullet -} \quad (5)$$

Oxidation of hydroxyls:

$$OH^- + h^+ \rightarrow OH\bullet \quad (6)$$

Photodegradation of organic by OH·:

$$organic + OH\bullet \rightarrow CO_2 + H_2O \quad (7)$$

Direct photoholes:

$$organic + h^+ \rightarrow Intermediates / CO_2 + H_2O \quad (8)$$

Protonation of superoxides:

$$O_2^{\bullet -} + OH\bullet \rightarrow HOO\bullet \quad (9)$$

This journal is © The Royal Society of Chemistry 2012

Co-scavenging of e^-:

$$HOO\bullet + e^- \rightarrow HO_2^- \quad (10)$$

Formation of H_2O_2:

$$HO_2^- + H^+ \rightarrow H_2O_2 \quad (11)$$

The illumination of the photocatalytic surface with sufficient energy leads to the formation of a positive hole (h^+) in the VB and an electron (e^-) in the CB, as demonstrated in Eq. 1.[4] The e^-_{TR} and h^+_{TR} in Eq. 4 represent the surface-trapped VB electron and CB hole, respectively, as described in Eqs. 2 and 3.[4] In the absence of electron scavengers, the photoexcited electron recombines with the VB hole in nanoseconds (ns) with simultaneous dissipation of heat energy, as shown in Eq. 4.[4] The recombination of the electron and hole must be prevented as much as possible for a photocatalyzed reaction to be favored. The ultimate goal of the process is to have a reaction between the activated electrons with an oxidant to produce a reduced product and a reaction between the generated holes with a reductant to produce an oxidized product. Thus, the presence of electron scavengers is vital for prolonging the recombination and successful functioning of photocatalysis. In the degradation of organic pollutants, the hydroxyl radical, which is generated from the oxidation of adsorbed water, where it is adsorbed as OH^-, is the primary oxidant; the presence of oxygen can prevent the recombination of an electron-hole pair while allowing the formation of a superoxide radical ($O_2^{\cdot-}$), as indicated in Eq. 5.[4] This $O_2^{\cdot-}$ radical can be further protonated to form the hydroperoxyl radical ($HO_2\cdot$), and subsequently H_2O_2, as shown in Eqs. 9 and 10, respectively.[4] The $HO_2\cdot$ radical formed was also reported to exhibit the scavenging property, and thus, the co-existence of these radical species can doubly prolong the recombination time of the h^+_{TR} in the entire photocatalysis reaction.[4] Although the h^+_{TR} has been widely studied for its capability of oxidizing organic species directly, this possibility has remained inconclusive. In the photocatalytic degradation of pollutants, when the reduction process of oxygen and the oxidation of pollutants do not advance simultaneously, an electron would accumulate in the CB, which causes an increase in the rate of recombination of $e^-$and h^+. Thus, to obtain the photo-catalyzed reaction, the e^--h^+ recombination must be prevented as much as possible.

2.1.3 Solar cells

Photovoltaics or solar cells are devices that directly convert the solar energy into electric power. Efficient solar devices rely on matching their light absorption spectrum to the AM1.5G spectrum irradiated on the earth surface. AM1.5G is defined by a broadband solar spectrum, spanning from 280 nm in the UV region to 2500 nm in the mid-infrared region. The power conversion efficiency (PCE) η of these devices can be given by

$$\eta = \frac{V_{oc} J_{sc} FF}{P_{inc}}, \quad (12)$$

where P_{inc} is the incident solar power on the device, V_{oc} is the open-circuit voltage, J_{sc} is the short-circuit current density, and FF is the fill factor. The short-circuit current density J_{sc} is the current density derived at zero voltage, whereas the open circuit voltage V_{oc} is the maximum voltage that a solar cell can generate.

The invention of DSSCs with a PCE of approximately 7% in 1991 triggered studies on the physics and device technologies of DSSCs.[20] A PCE as high as 12% has been achieved using a porphyrin-sensitized mesoporous TiO_2 photoanode and cobalt redox electrolyte.[47] However, the commercialization of electrolyte-containing DSSCs has been hindered due to the leakage of the liquid electrolyte. Substitution of the liquid electrolytes with solid hole transporting materials (HTMs) leads to a solvent-free solid-state sensitized heterojunction solar cell. This device is usually fabricated using a dye-sensitized mesoporous TiO_2 film as an electron transporting layer and a HTM as a hole-transporting layer. The PCEs of inorganic chalcogenide- or organic dye-based solid-state DSSCs are approximately 6-7%;[48,49] whereas, some reports on solid-state DSSCs based on perovskite $CH_3NH_3PbI_{3-x}Cl_x$ (x = 0 or 1) sensitizers have high PCEs greater than 11%, promising further breakthroughs in this field.[50,51] The different structures of the perovskite-based solar cells are displayed in Fig. 4.[52] The first version of the perovskite solar cell is sensitized solar cells based on the nanodot morphology, which is the same mechanism as DSSCs. (Fig. 4a). All-solid-state perovskite $CH_3NH_3PbI_3$ sensitized solar cells with 2,2′7,7′-tetrakis-(*N*,*N*-di-*p*-methoxyphenyl amine)-9,9′-spirobifluorene (spiro-MeOTAD) as HTMs have achieved a PCE of up to 9.7%. In this configuration, the concentration of the deposited perovskite is relatively low, and the HTM should be infiltrated into the pores of the TiO_2 film. The second version is the p-n junction solar cells, which were reported by Snaith and co-workers.[51] These researchers employed Al_2O_3 as a scaffold to support the perovskites and spiro-MeOTAD. A thin layer of perovskite was formed on the surface, and the HTM infiltrated into the pores of the Al_2O_3 film (Fig. 4b). However, the above two configurations suffer from the pore filling of the HTM. A more advanced configuration has been proposed, where the pores of the mesoporous oxide film are filled with perovskite instead of HTM (Fig. 4c). In this configuration, a thin capping layer (over layer) of perovskite is recommended to contact the HTM. A mesoporous oxide film-free structure, or planar p-n junction, is proposed because perovskite is capable of transporting electrons and holes (Fig. 4d).

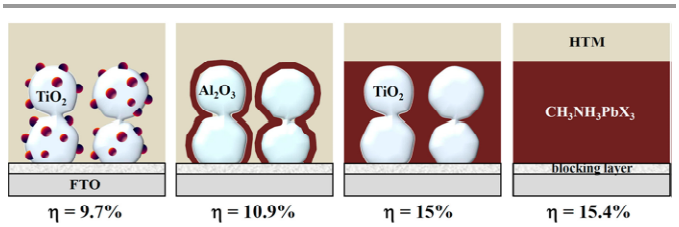

Fig. 4 Structural progress in the perovksite-based solid-state solar cell from a perovskite dot deposited on TiO_2 with a PCE of 9.7% to a planar p-n junction with PCE of 15.4%, via the meso-superstuructured scaffold Al_2O_3 concept with a PCE 10.9% and perovskite-infiltrated nancomposite with PCE of 15%. Reproduced with permission from ref. 52. Copyright 2014, American Chemical Society.

Organometallic perovskite solar cells have developed rapidly in the past two years. However, the understanding of the working principles and mechanisms has not grown at the same pace. It is necessary to understand the mechanisms that govern the carrier separation, transport, extraction and their recombination. To have a clear understanding of the working principles and mechanism of charge accumulation in these devices, impedance spectroscopy measurements were performed. In DSSCs, no charge accumulation in the dye (absorber) was detected. Charge accumulation in the high density of states (DOS) of a $CH_3NH_3PbI_3$ perovskite absorber was observed by extracting the capacitance of the samples in nanostructured TiO_2 and ZrO_2 electrodes.[53] DSSCs and bulk heterojunction organic solar cells take advantage of a nanostructured morphology that facilitates rapid charge separation of photogenerated carriers to different materials. Ultrafast charge injection from the absorber to electron and hole transport materials avoids recombination of electron-hole pairs and produces long diffusion lengths for effective charge collection. At the beginning of its discovery, the perovskite solar cell was a TiO_2 sensitized cell; thus, it was believed that electrons would be injected into the wide BG metal oxide as the main transport pathway. However, the observation of significant efficiencies in perovskite solar cells with no electron transporting material,[51,54] or even in a thin film configuration,[55,56] indicates that a perovskite solar cell can work in a different configuration than a DSSC. These results strongly indicate that photogenerated electrons and holes coexist in the $CH_3NH_3PbX_3$ absorber material and travel to the selective contacts, where they are separately collected. In this sense, some important parameters for cell performance in terms of the BG energy assigned to the optical absorption ability and diffusion length (L_d) of electrons and holes should be carefully identified in working devices, constituting a step forward in the further optimization of the solar cells.

2.2 Perovskite materials

Perovskite initially referred to a mineral composed of calcium titanate with a chemical formula of $CaTiO_3$. Later, this material lent its name to the class of compounds that have the same type of crystal structure as $CaTiO_3$. The general chemical formula for perovskite compounds is ABX_3, where A and B are two cations of different sizes, and X is an anion that bonds to the A and B cations. The ideal perovskite-type ABX_3 structure has cubic symmetry with space group *Pm3m*. In this structure, the B cation is 6-fold coordinated, and the A cation is 12-fold cuboctahedral coordinated, surrounded by an octahedron of the X anions.

A wide variety of compositions and constituent elements essentially keep the basic structure unchanged, and more than 90% of metal elements can be successfully incorporated into the perovskite lattice. In the ABX_3 structure, the A cation is typically larger than the B cation, and the properties of the perovskite are determined by the cations occupying its A- and B-site lattice. For the halide perovskite structure, ABX_3 (where X is F, Cl, Br, or I), monovalent and divalent cations are usually stabilized in the A and B sites, respectively.

In the ideal perovskite structure with a cubic symmetry, where the atoms are connected with one another, the B-X distance is equal to $a/2$ (a is the cubic unit cell parameter), whereas the A-X distance is ($a/\sqrt{2}$), and the following relationship between the ionic radii holds: $r_A + r_X = \sqrt{2}(r_B + r_X)$, where r_A, r_B and r_X are the ionic radii of A, B and X site elements, respectively. The relative ionic size requirements for stabilizing the cubic structure are quite stringent; therefore, slight buckling and distortion can produce several lower-symmetry distorted versions, in which the coordination numbers of the A cations, B cations or both are reduced. However, the cubic structure could be retained in the ABX_3 compounds even if the above equation is not precisely obeyed. Goldschmidt first introduced a tolerance factor (t) to evaluate the deviation from the ideal structure, which is defined by the following equation: $t = (r_A+r_X)/\sqrt{2}\,(r_B+r_X)$.[57]

It has been generally accepted that perovskites can be stabilized when t ranges between 0.76 and 1.13. However, it has also been argued that perovskite structures are not stable, even in the most favorable range of $0.8 < t < 0.9$.[58] It has been indicated that perovskite stability cannot be predicted solely based on a tolerance factor. An additional consideration for perovskite formability is the octahedral factor (μ), $\mu = r_B/r_X$, which was then proposed.[59] For the alkali metal halide perovskite, formability was determined from the t-μ mapping, where the perovskite was stabilized for a tolerance factor ranging between 0.813 and 1.107 and an octahedral factor ranging from 0.442 and 0.895.[59] For example, the ionic radii of r_A in the $APbX_3$ perovskite are estimated based on the effective ionic radii,[52] where the A cation radii range from ~160 picometers (pm) to ~250 pm. The t values for $CH_3NH_3PbX_3$ were calculated at 0.85, 0.84 and 0.83 for X = Cl, Br, and I, respectively, based on the radii of $CH_3NH_3^+$ = 180 pm, Pb^{2+} = 119 pm, Cl^-= 181 pm, Br^- =196 pm and I^- = 220 pm. It was observed that the t value of most cubic perovskites is between 0.8 and 0.9;[60] thus, $CH_3NH_3PbX_3$ perovskites are expected to have a cubic structure. A tolerance factor larger than unity implies that the A cations are too large for the compound to adopt the ideal cubic perovskite structure; instead, hexagonal perovskites, in which octahedra share faces and form chains along the hexagonal c-axis, are often formed. The hexagonal perovskites are less common than the cubic perovskites and are stabilized by the formation of metal-metal bonds between the B cations of the BX_6 octahedra.

Substitution at both A and B sites may change the composition and symmetry of the perovskite and create cation or oxygen vacancies, which have a major effect on the band structures and photocatalytic and photovoltaic behaviors of these materials. Moreover, many other properties such as adsorption properties can also be designed by substitution on both A and B sites. In addition, doping of the X site could also affect the structure and BG of perovskites. Therefore, perovskites with photocatalytic activity can be easily tuned using many methods including doping functional elements to

This journal is © The Royal Society of Chemistry 2012

the A, B site and/or X site as well as changing the crystallite size of the sample.

3. Perovskite materials as catalysts for photocatalytic reactions

TiO_2 compounds are widely used as catalysts for photocatalysis reactions; however, due to their wide BG, only UV light can be utilized. The development of new photocatalysts with reduced BGs to successfully utilize visible light, which is the main part of solar light, is of great importance. Perovskite has recently attracted increasing attention for the water splitting reaction and degradation of organic dyes.[61-65] Based on the steps of the degradation reactions of organic pollutants, similar to the water splitting reaction, the key to improve the photocatalytic activity is to suppress electron-hole recombination and to tailor the BG because the BG width is one of the most critical properties of photocatalytic materials and determines the amount of solar energy to be absorbed and that is available for conversion. In this section, a brief description of band gap engineering and suppressing electron-hole pair recombination strategies are presented and the detailed investigation of perovskite design based on above strategies for water splitting reaction and degradation of organic dyes were also conducted.

3.1 Strategies to design perovskite materials for the water splitting reaction and degradation of organic dyes

3.1.1 Band gap engineering

The strategies to engineer the BG energy include applying donor-acceptor coincorporation, using 4d and 5d cations as donors with higher atomic d orbital energies to guarantee that the conduction-band maximum (CBM) energy level is not lowered and high electron mobility is maintained, and incorporating 2p or 3p anions with higher atomic p orbital energies than that of O to raise the valence-band maximum (VBM) for reducing the BG energy. The doping of foreign elements into UV-active metal oxides is a conventional method employed for the preparation of visible-light-responsive photocatalysts. In such doped photocatalysts, however, dopants in the photocatalyst act not only as visible-light absorption centers, with an absorption coefficient dependent on the density of dopants, but also as recombination sites between photogenerated electrons and holes.

In the UV-active photocatalysts, the bottoms of the CBs, which consist mainly of empty transition-metal d orbitals, are located at a potential slightly more negative than 0 V, and the tops of the VBs, consisting of O 2p atomic orbitals, are more positive than 3 V. As mentioned above, such a large BG makes the material unable to harvest visible light, nevertheless suggesting that the photocatalysts have enough potential to oxidize water, judging from the difference between the oxidation potential of H_2O into O_2 (1.23 V vs. NHE) and the VB edge potential (3 V vs. NHE). Therefore, if other elements (e.g., N 2p) having atomic orbitals with a potential energy higher than O 2p atomic orbitals are introduced, new VBs can be formed instead of pure O 2p atomic orbitals, which results in a decrease in E_{bg} without affecting the CB level, thus producing a visible-light-driven photocatalyst with band edge potentials suitable for the water splitting reaction. It was observed that for the Ta-N system, if 3.1% O was replaced by N, the VBM was shifted up by 0.34 eV and the CB also increased by 0.05 eV; thus, the BG was reduced by 0.29 eV.[66] Various elements, such as Zn, N etc., are used to dope prisitine perovskite to reduce the BG.[67,68] In addition, the structure of the perovskite could also affect the BG energy.[69]

3.1.2 Suppressing electron-hole pair recombination

As mentioned above, the recombination of photo-generated electron-hole pairs could decrease the photoactivity of the catalysts. Thus, the recombination process should be suppressed as much as possible. There are several strategies to suppress this recombination, such as a smaller particle size to reduce the diffusion length and a nanostructured morphology. A site doping for the perovskite could yield a reduction in the particle size as well as nanostructuring.[70]

The preparation methods also have a strong effect on the nanostructure of perovskite materials. The commonly used solid-state reaction method requires annealing at high temperature for a long time with frequent intermediary grindings, which results in poor homogeneity and high porosity as well as difficulties in the control of the particle size of perovskite. Several wet chemical methods have been proposed to improve the homogeneity and reproducibility of the powders and to reduce the preparation temperature, such as sol-gel and hydrothermal methods.[71,72] These advanced preparation technologies are expected to be used for the development of highly active and visible-light-driven perovskite photocatalysts.

3.2 Water splitting reaction

Recently, perovskites have been widely used as the catalysts for water splitting reactions using solar energy.[67,92-94] The catalytic activity of a perovskite is mainly determined by the B-site element(s). There are two main groups of elements that can act as active cation components (B site) in a perovskite photocatalyst. The first group includes Ti^{4+}, Nb^{5+}, Ta^{5+}, W^{6+}, Zr^{4+} and Ce^{4+} elements with empty d orbitals, and the elements such as Ga^{3+}, In^{3+}, Ge^{4+}, Sn^{4+} and Sb^{5+} in the second group with filled d orbitals have also been considered to be good catalysts for the water splitting reaction.[31,32] In this section, we will focus on the design of perovskite catalysts using proposed strategies for the water splitting reaction to achieve UV and visible lights. Shown in Fig. 5 are schematics of the high-level summary of Section 3.

3.2.1 Band gap engineering

3.2.1.1 Selection and doping process of B site elements

Recently, there have been many reports about pristine and doped perovskite photocatalysts, such as Ti, Ta, and Nb-based perovskite oxides for water splitting reaction under UV and visible lights.[67,73-75] However, the undoped titanates always had larger E_{bg}, which limited their applications in the visible-light-driven water splitting reactions. For example, several metals such as Rh, Mn, Ru and Ir were used to dope $SrTiO_3$ to give visible light responses for H_2 or O_2 evolution reactions.[76]

Although $SrTiO_3$ with a BG of 3.2 eV could not absorb visible light, $SrTiO_3$ doped with Rh, Ir, Ru and Mn exhibits absorption in the visible light region, as observed in Fig. 6. The visible light responses were due to the electronic transition from donor levels formed with dopants to the CBs of the host photocatalysts. Among the various doped photocatalysts, Rh-doped $SrTiO_3$ exhibited the highest activity among the doped photocatalysts for H_2 evolution under visible light irradiation.[76] In this case, the dopant exists as a trivalent ion (Rh^{3+}) on the B-site (Ti^{4+} site), which forms a donor level at a lower potential than the top of the VB composed of O 2p orbitals, and the apparent BG consequently became narrowed.

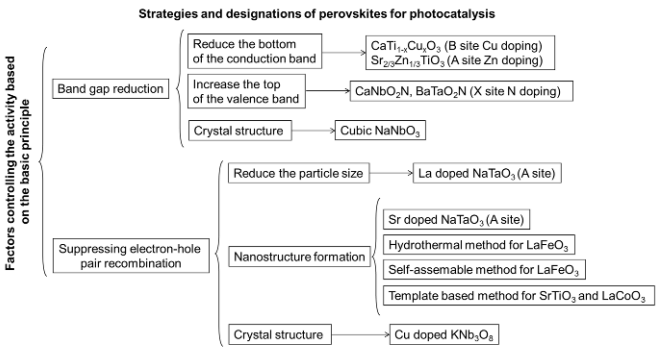

Fig. 5 The schematics of the high-level summaries of Section 3.

In addition to $SrTiO_3$, some other titanates also attracted considerable attention by doping suitable elements such as Cu, Sc, Cr and Fe in the B site.[75,77,78] $CaTiO_3$ is one of the best-known wide gap insulating oxides with a BG of approximately 3.5 eV. However, careful doping by Cu element in the B site could make it conductive. $CaTi_{1-x}Cu_xO_3$ (x=0.01, 0.02, 0.03 and 0.04) compounds were prepared by the sol-gel method coupled with the ultrasonic technique and used as catalysts for the H_2 evolution reactions under UV light.[75] It was observed that 2 mol.% Cu^{2+}-doped $CaTiO_3$ exhibited the highest activity for the water splitting reaction. The excessive Cu^{2+} doping became the recombination centers for photogenerated charges; therefore, the photocatalyst activity of hydrogen production decreased. The photocatalytic activity of doped $CaTiO_3$ for H_2 evolution under UV light was increased dramatically by approximately 8-fold compared with that of pure $CaTiO_3$. However, the addition of Cu also led to the absorption of visible light on the $CaTiO_3$, which could be attributed to the transition from the donor levels formed by Cu^{2+} to the CB of copper-doped $CaTiO_3$, as evidenced by density functional theory (DFT) calculations.[75] Yun et al. studied the stability, electronic structure and photocatalytic properties of the Sc-doped Sr_2TiO_4 using first-principles calculations based on DFT.[77] The BG of $Sr_2Sc_{0.125}Ti_{0.875}O_4$ narrowed by approximately 0.25 eV compared with that of undoped Sr_2TiO_4, resulting in the red-shift of the absorption spectra edge. In particular, the dispersion of the CBs and VBs of $Sr_2Sc_{0.125}Ti_{0.875}O_4$ was enhanced after the doping, which was preferable for the photocatalytic performance. In addition, a new weak absorption appeared in the visible light region, which somehow contributed to the photocatalytic activity of $Sr_2Sc_{0.125}Ti_{0.875}O_4$. Hwang et al. also studied the effect of B-site metal dopants on the band structure of the layered perovskite $La_2Ti_2O_7$ and observed that only Cr and Fe exhibited intense absorption in the visible light region due to the decreased BG by the B site doping.[78] In addition, these two catalysts produced H_2 photocatalytically by the water splitting reaction under visible light irradiation.

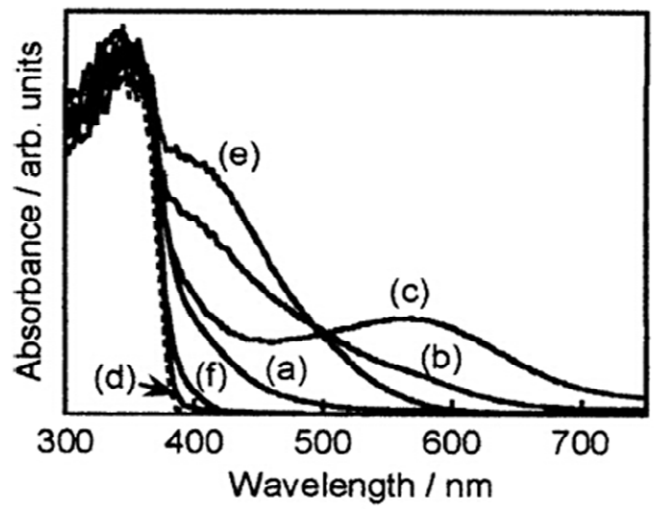

Fig. 6 Diffuse reflectance spectra of $SrTiO_3$:M(0.5%). M = (a) Mn, (b) Ru, (c) Rh, (d) Pd, (e) Ir, and (f) Pt. A broken line represents a spectrum of nondoped $SrTiO_3$. Reproduced with permission from ref. 76. Copyright 2004, American Chemical Society.

3.1.1.2 Selection and doping process of A-site elements

In addition to B-site doping of titanates, Zn^{2+} was also used as an A-site dopant to modify $SrTiO_3$ and $BaTiO_3$ perovskites ($Sr_{2/3}Zn_{1/3}TiO_3$ and $Ba_{5/6}Zn_{1/6}TiO_3$) to enhance the photoactivity for water splitting reactions by reducing E_{bg}.[67] It was observed that the top of the VBs dominantly consisted of the O 2p orbital, whereas the bottom of the CBs was composed of the Ti-3d orbital and Zn-3d orbital. Furthermore, with the increase of the Zn content, the contribution of the Zn-3d orbital to the CBs increased; thus, the BG narrowed for Zn-doped $SrTiO_3$ and Zn-doped $BaTiO_3$, and the BG values decreased with increased concentration of Zn atoms.[67] This study demonstrated that the partial doping of the A site with Zn ions could change the crystal and band structures and significantly promoted the carrier mobility of the catalysts to result in good photocatalytic activities.[67] Specifically, the BGs for Zn ions doped at the Sr or Ba sites with different concentrations were all narrowed with respect to pure $SrTiO_3$ or $BaTiO_3$. The reduced BG values were 0.675, 0.555 and 0.526 eV by doping Zn at the Sr site with molar ratios of 1/3, 1/6 and 1/10, respectively, whereas the reduced BG values were 0.169, 0.118 and 0.087 eV with doping of Zn at the Ba site with molar ratios of 1/3, 1/6 and 1/10, respectively.

Some researchers have also investigated the A-site cation in tantalate and niobate systems for the optimization of E_{bg} for realizing water splitting reaction under visible light irradiation.

This journal is © The Royal Society of Chemistry 2012

For example, the band structures of perovskite-type materials $ATaO_3$ (A=Li, Na, K, Ag) were studied by Kato et al.[74] It was observed that the E_{bg} of $AgTaO_3$ was 3.4 eV, lower than those of $LiTaO_3$ (4.7 eV), $NaTaO_3$ (4.0 eV) and $KTaO_3$ (3.6 eV). The authors considered that the differences in BG were not determined by the Ta-O-Ta bond angle in the perovskite because the Ta-O-Ta bond angle in $KTaO_3$ was closer to 180°, which was beneficial for the reduction of E_{bg}. A hybrid orbital of Ag 4d and O 2p forming a VB at a more negative level than O 2p orbitals should be attributed to the smaller BG of $AgTaO_3$. In addition, $AgTaO_3$ exhibited reasonable photocatalytic activity for the water splitting reaction. Machida et al. studied the effect of dual doping at the A site on the band structure and photocatalytic activity for the water splitting reaction for the layered perovskite $MLnTa_2O_7$ (M = Cs, Rb, Na, and H; Ln = La, Pr, Nd, and Sm).[79] The optical E_{bg} was dependent on the lanthanide, Ln, but negligibly affected by the monovalent interlayer cations, M. The effect of Ln can be explained by the shift of the Ln 4f levels from the CB edge to the VB edge with an increasing number of Ln 4f electrons. In contrast, the photocatalytic activity was strongly affected by not only Ln but also M; the highest activity was attained by a series of M = Rb with a sequence of Ln: Nd > Sm > La > Pr. Similar results were obtained by Machida et al. in the $RbLnTa_2O_7$ system.[80] Yin et al. developed a series of photocatalysts by changing the ionic radius in the A-site cations in $MIn_{0.5}Nb_{0.5}O_3$ (M = Ca, Sr, and Ba) with the ABO_3-type perovskite structure.[81] It was observed that the larger ionic radius in the A-site cations led to a smaller BG and that $BaIn_{0.5}Nb_{0.5}O_3$ had the smallest BG. $BaIn_{0.5}Nb_{0.5}O_3$ photocatalysts exhibited the best photocatalytic activities for water splitting under visible light irradiation due to the small BG. Although the photocatalytic activities of these photocatalysts under visible light irradiation are relatively low, it is an effective route to design new photocatalysts.

3.1.2.3 Selection and doping process of X-site elements

In addition to the A/B site doping of perovskite oxides, doping at the O site with N^{3-} to form oxynitrides was also considered as an effective approach to enhance the activity for the water splitting reaction under visible light.[68,82,83] In these materials, the N 2p orbitals form a new VB, thus reducing the E_{bg}. $LaMO_2N$ (M = Ti, Zr), $LaMON_2$ (M = Nb, Ta), and $AEMO_2N$ (AE = Ca, Sr, Ba; M = Nb, Ta) are well-known perovskite oxynitrides. Most of these materials can absorb light with wavelengths up to 600 nm or longer; furthermore, BG is flexible in a wide range from the UV to the near-IR region by forming solid solutions with other perovskite oxides and oxynitrides. The superior chemical and thermal stabilities of the oxynitrides made them attractive for applications as visible-light-responsive photocatalysts for the water splitting reaction. For example, tantalum oxynitride series $ATaO_2N$ (A = Ca, Sr, and Ba) and $PrTaON_2$ are promising candidates for the photocatalytic splitting of water under visible light. It was observed that $BaTaO_2N$, $SrTaO_2N$ and $CaTaO_2N$ have cubic, tetragonal and orthorhombic symmetries, respectively, whereas $PrTaON_2$ is orthorhombic and isostructural with $CaTaO_2N$. The corresponding structures are shown in Fig. 7.[82] Smaller A-site cations lead to more octahedral tilting and less dispersed CBs and thus a higher energy for the CB edge. Increasing the nitrogen content leads to an upward shift in the position of the VB edge. All the proposed catalysts have CB edges that lie above the reduction potential for water and are therefore suitable for the photocatalytic production of hydrogen, whereas the VB edges lie near the oxidation potential of water.

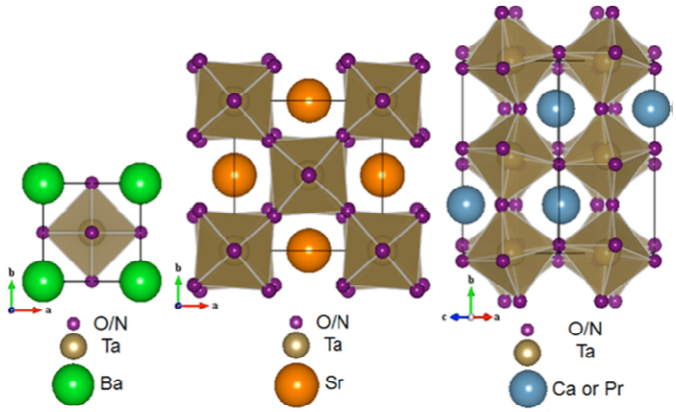

Fig. 7 Structures of cubic $BaTaO_2N$, tetragonal $SrTaO_2N$, and orthorhombic $CaTaO_2N$ or $PrTaON_2$. Reproduced with permission from ref. 82. Copyright 2013, American Chemical Society.

Some perovskite-type niobium oxynitrides ($CaNbO_2N$, $SrNbO_2N$, $BaNbO_2N$, and $LaNbON_2$) prepared by heating the precursors under a flow of NH_3 at an appropriate temperature are also examined for hydrogen and oxygen evolution from water under visible light. These materials possess visible-light absorption bands between 600-750 nm, depending on the A-site cations in the structures.[68] Fig. 8 presents the UV/Vis diffuse reflectance spectra (DRS) of the samples. All the samples absorbed light in the visible region, and the estimated BGs decreased in the order Ca>Sr>Ba, most likely resulting from a change in the distortion of NbO_xN_y blocks in the perovskite structure because of the increasing A-site cation size.[68] As the distortion was reduced, the delocalization of the excited energy increased, resulting in a smaller BG.

Among the prepared samples, $CaNbO_2N$ exhibited the highest activity for both H_2 and O_2 evolution, producing 1.0 mmol h^{-1} of H_2 and 31.2 mmol h^{-1} of O_2. No continuous N_2 evolution was observed, indicating that $CaNbO_2N$ was stable under both water reduction and oxidation conditions.[68] However, $SrNbO_2N$ demonstrated a low O_2 evolution rate and no H_2 evolution, whereas $BaNbO_2N$ and $LaNbON_2$ produced no gas evolution under visible light. Although $BaNbO_2N$ and $LaNbON_2$ had smaller BGs, allowing more absorption of the solar spectrum, these materials no activity for the water reduction or oxidation. This phenomenon could be attributed to the fact that the small BGs of $BaNbO_2N$ and $LaNbON_2$ led to an insufficient overpotential for the surface chemical reactions to occur. It is also considered that defect sites in the crystal structure may have acted as recombination centers for photogenerated electrons and holes, thus leading to negligible activity.

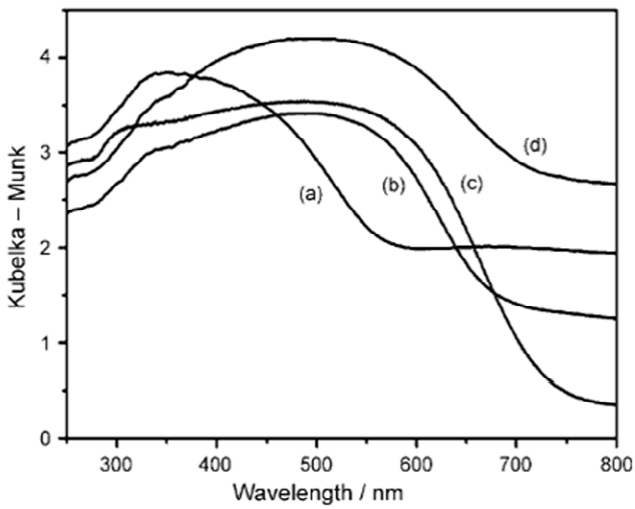

Fig. 8 UV/Vis diffuse reflectance spectra of perovskite-type niobium oxynitrides: a) $CaNbO_2N$; b) $SrNbO_2N$; c) $BaNbO_2N$; d) $LaNbON_2$. Reproduced with permission from ref. 68. Copyright 2011, Wiley-VCH Verlag GmbH & Co. KGaA, Weinheim.

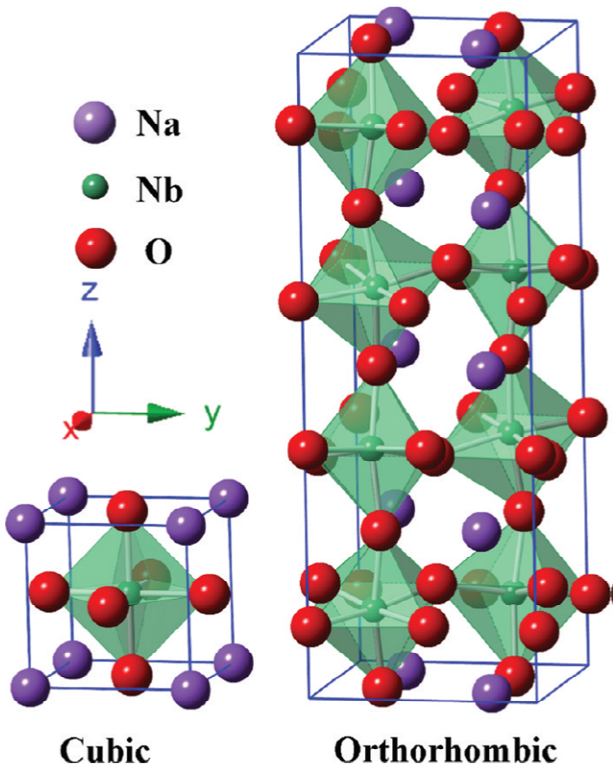

Fig. 9 Schematic crystal structures of cubic and orthorhombic $NaNbO_3$. Reproduced with permission from ref. 69. Copyright 2012, American Chemical Society.

3.1.2.4 Crystal structure of the perovskite photocatalysts

The crystal structure also had an effect on the BG of the perovskite. For example, Li et al. have studied the effect of crystallographic symmetry (cubic and orthorhombic, shown in Fig. 9) on the electronic structure and photocatalytic activity of $NaNbO_3$ for the water splitting reaction.[69] The cubic phase $NaNbO_3$ oxide exhibited a narrower BG (3.29 eV) than the common orthorhombic $NaNbO_3$ (3.45 eV).[69] The photocatalytic H_2 evolution activity over cubic $NaNbO_3$ was approximately twice that of the orthorhombic $NaNbO_3$. The DFT calculation indicated that the higher activity over cubic $NaNbO_3$ could be attributed to its unique electronic structure of high symmetry, which was beneficial for electron excitation and transfer, which suggested that a higher symmetry of the perovskite improved the photoelectron excitation and transfer, offering a new approach to enhance the photocatalytic activity in some other perovskite photocatalysts.

3.2.2 Suppressing electron-hole pair recombination by reducing particle size and/or nanostructuring

3.2.2.1 A-site doping process

Doping of a foreign element into a photocatalyst is one of the strategies that can affect the morphology (particle size and surface structure) of photocatalysts to achieve visible light. Considerable efforts have been devoted to the doping of some UV light sensible photocatalysts such as $NaTaO_3$ to reduce the wide BG to less than 3 eV, making these materials capable of adsorbing visible light.[70,84,85] For example, a highly active La-doped $NaTaO_3$ photocatalyst was successfully developed for the water splitting reaction.[70,84,85] Kudo et al. observed that the doping changed the morphology of the $NaTaO_3$ particle shown in Fig. 10.[84] The decrease in the particle size and the formation of the characteristic surface nanostep structure yielded the excellent photocatalytic performance. More specifically, the particle size of La-doped $NaTaO_3$ was 0.1-0.7 μm, whereas that of non-doped $NaTaO_3$ was 2-3 μm. In addition, the surface of non-doped $NaTaO_3$ was smooth, whereas La-doped $NaTaO_3$ had surface nanostructures with sizes of 3-15 nm. The decrease in the particle size and the formation of characteristic surface nanostep structure yielded excellent photocatalytic performance.

Iwase et al. also observed that the photocatalytic water splitting reaction over $NaTaO_3$ was drastically enhanced by doping the Na site with Ca, Sr, and Ba;[85] these doping processes resulted in reduced $NaTaO_3$ particles. Moreover, surface nanostep structures were constructed on the doped $NaTaO_3$ catalysts. It was observed that the surface morphology was affected by the amounts of Sr and Ba. Fig. 11 presents the SEM images of various doped $NaTaO_3$; the particles of the doped catalysts were well-crystallized. The particle sizes (0.1–0.5 μm) of the Sr-, Ca- and Ba-doped $NaTaO_3$ materials (5 mol.%; (Figs. 11f–h) were remarkably smaller than those of the undoped $NaTaO_3$ powder (2–3 μm; Fig. 11a). Although the surface nanostep structures did not appear at Sr doping levels of 0.1 and 0.5 mol.%, the particle size decreased and the crystallinity increased compared with the values for undoped $NaTaO_3$, as illustrated in Figs. 11a–c. The surface nanostep structure, however, was created on the $NaTaO_3$ surface at Sr doping levels equal to or greater than 1 mol.% (Figs. 11d–f). The surface nanostep structures were created by Ba doping levels equal to or greater than 1 mol.%, as observed for Sr-doped $NaTaO_3$, while they were also constructed with 0.5 mol.% of Ca doping. The threshold amount of dopant for the creation of the surface nanostep structures was dependent on

 This journal is © The Royal Society of Chemistry 2012

the dopant. X-ray photoelectron spectroscopy (XPS) measurements suggested that the surface nanostep structures were constructed by the doping of alkaline-earth metal ions inside the $NaTaO_3$ particles. Photoluminescence measurements revealed that a small amount of doped Sr promoted the charge separation, whereas a large amount of doped Sr stimulated the formation of charge recombination centers due to the formation of significant amounts of defects. The photocatalytic performance was determined by balancing these positive and negative effects.

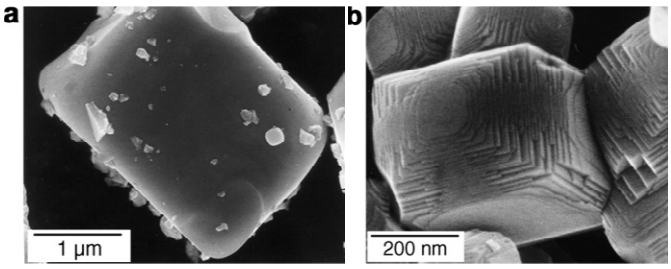

Fig. 10 Scanning electron microscope (SEM) images of (a) non-doped $NaTaO_3$ and (b) La-doped $NaTaO_3$. Reproduced with permission from ref. 84. Copyright 2007, Elsevier Inc.

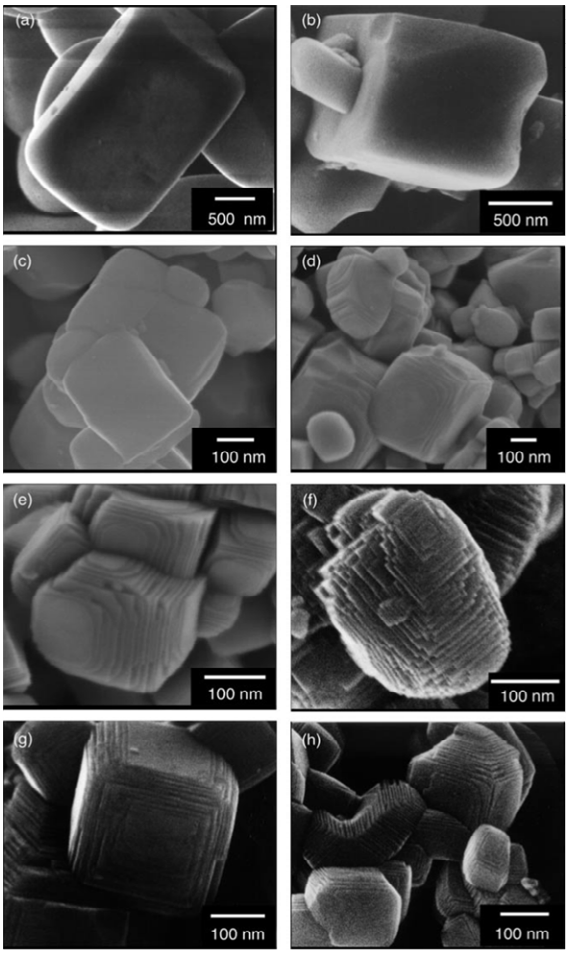

Fig. 11 SEM images of a) nondoped $NaTaO_3$, and $NaTaO_3$ doped with b) 0.1 mol% Sr; c) 0.5 mol% Sr; d) 1 mol% Sr; e) 2 mol% Sr; f) 5 mol% Sr;g) 5 mol% Ca; and h) 5 mol% Ba. Reproduced with permission from ref. 85. Copyright 2009, Wiley-VCH Verlag GmbH & Co. KGaA, Weinheim.

3.2.2.2 Preparation methods

As mentioned above, the preparation methods had a strong effect on the nanostructure of the perovskite. In addition to the commonly used solid-state reaction method, several wet chemical methods have been proposed to improve the homogeneity and reproducibility of the powders and to reduce the preparation temperature, such as sol-gel and hydrothermal methods. Tijare et al. used a sol-gel method to synthesize $LaFeO_3$ perovskite catalysts,[86] which exhibited an optical BG of 2.07 eV with the absorption spectrum predominantly in the visible region of the spectrum. This photocatalyst exhibited high visible light activity for an ethanol-assisted water splitting reaction with H_2 generation of 3315 mmol g^{-1} h^{-1}, which is quite comparable to several other potential semiconductor-based photocatalysts and much higher than the reported values for the same composition. The improved photocatalytic activity for the sol-gel-derived $LaFeO_3$ should be due to its higher surface area and nanosized particle morphology. Smaller particles are expected to have a smaller period for migration of the photogenerated change to the surface, thereby reducing the possibility of charge recombination, one of the major bottlenecks in such photocatalysts.

A comparative study of alkali tantalate $ATaO_3$ and niobate $ANbO_3$ (A = Na and K) powders with perovskite structures, synthesized using the hydrothermal method, as the catalysts for the water splitting reaction was conducted.[73] The BGs of the niobates were smaller than those of the tantalates, whereas the tantalates exhibited higher activity than niobates, especially for $NaTaO_3$ with a cubic crystalline structure.[73] A fast and facile process for the preparation of perovskite $NaTaO_3$ nanocrystals with Ta_2O_5 and NaOH as starting materials using a microwave-assisted hydrothermal (MHT) technique was reported by Shi et al.[87] By pretreating the Ta_2O_5 powder using ball milling, pure-phase $NaTaO_3$ was successfully synthesized under quite mild conditions in less than 3 hours through the formation of an intermediate pyrochlore $Na_2Ta_2O_6$ phase, whereas a much longer time, typically 24 hours, was required in a conventional hydrothermal (CHT) process. After cooperation with a NiO co-catalyst, the $NaTaO_3$ prepared by MHT exhibited photocatalytic activity for overall water splitting that was more than two times higher than that attained using the CHT method due to the good crystallinity and large surface area achieved in a short reaction time.[87]

Some new methods such as direct dehydration, nanosheet processing and template-based method have been used for the preparation of perovskite catalysts for the water splitting reaction. For example, $Sr_{0.5}TaO_3$ with a perovskite structure was prepared using layer-structured $H_2Sr_{1.5}Ta_3O_{10}$ by direct dehydration and nanosheet processing, and the photocatalytic activities of the obtained two structures were investigated for the evolution of H_2 and O_2 from distilled water under UV light irradiation.[88] As illustrated in Fig. 12, $Sr_{0.5}TaO_3$ was synthesized using two types of processes, direct dehydration of

$H_2Sr_{1.5}Ta_3O_{10}$ and soft chemical stacking of $(Sr_{1.5}Ta_3O_{10})^{2-}$ nanosheets obtained from $H_2Sr_{1.5}Ta_3O_{10}$ through nanosheet processing.[88] The average gas evolution rates were 66 μmol h^{-1} (H_2) and 16 μmol h^{-1} (O_2) for $Sr_{0.5}TaO_3$ prepared by direct dehydration, whereas those obtained by nanosheet processing were 126 μmol h^{-1} (H_2) and 33 μmol h^{-1} (O_2).[88]

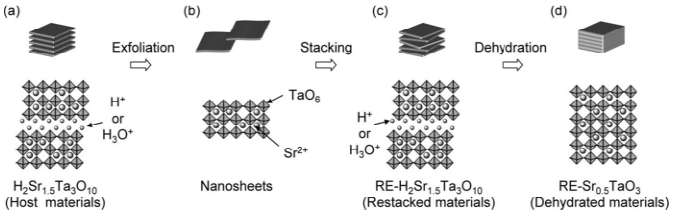

Fig. 12 Schematic structural drawing of the transformation from host materials $H_2Sr_{1.5}Ta_3O_{10}$ to dehydrated materials RE-$Sr_{0.5}TaO_3$. Reproduced with permission from ref. 88. Copyright 2008, Wiley-VCH Verlag GmbH & Co. KGaA, Weinheim.

Nuraje et al. demonstrated a novel and general approach to synthesize perovskite nanomaterials in an aqueous system using the genetically engineered M13 virus with the preparation method shown in Fig. 13.[89] Carboxylate ions on the surface of the virus chelate with Ti^{4+} ions (shown in yellow) and electrostatically interact with Sr^{2+} ions (shown in blue). The filamentous body of the M13 virus comprises approximately 2700 identical copies of the major coat protein pVIII (Fig. 13). Genetically engineered viruses provided effective templates for perovskite nanomaterials. $SrTiO_3$ nanoparticles were successfully prepared using the virus templates and a smaller particle size and higher crystallinity compared with conventional techniques were obtained. This new method will extend the scope of biotemplated synthesis to ternary metal oxides as well as more complex materials. Furthermore, the virus-templated $SrTiO_3$ perovskite nanomaterials exhibited good photocatalytic performance for the water splitting reaction under UV and visible light irradiation.[89]

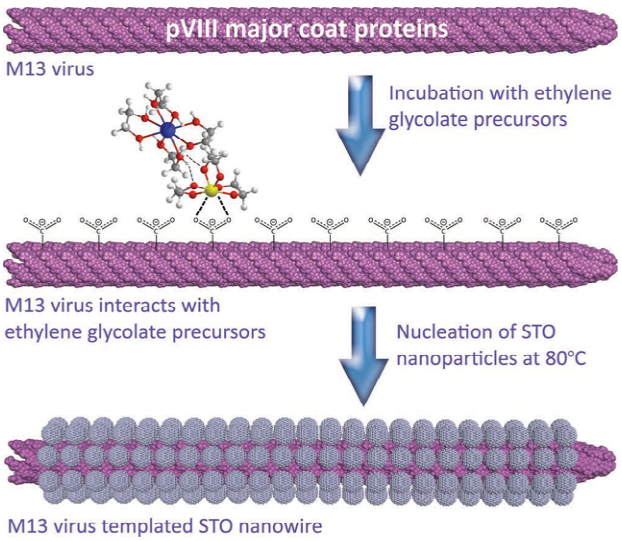

Fig. 13 Schematic of M13 virus-assisted synthesis of perovskite nanomaterials. Reproduced with permission from ref. 89. Copyright 2012, Wiley-VCH Verlag GmbH & Co. KGaA, Weinheim.

In addition to the main systems of titanates, niobates and tantalates for the water splitting reaction, some other $SrSnO_3$-based perovskite oxides have been used as photocatalysts due to their high photocatalytic activity, which could be attributed to the spatial structure of $SrSnO_3$. The three-dimensional network of corner-sharing SnO_6 octahedra can help charge carriers move more easily, and the octahedral tilting distortion had a positive effect on local charge separation.[90] $SrSnO_3$ nanoparticles with peanut-like morphologies were synthesized via a simple aqueous peroxide route.[91] These peanut-shaped $SrSnO_3$ were formed by the fusion of two or more nanoparticles with an average size of 45 nm, which exhibited a much higher photocatalytic activity than the $SrSnO_3$ powder synthesized via a solid-state reaction, which could be attributed to their higher structural order, higher surface area and smaller particle size.[91] It is reported for $SrSnO_3$ that the top of the VB is mainly composed of the O 2p orbital, whereas the bottom of the CB was mainly composed of the Sn 5s orbital. Therefore, the higher degree of order of the SnO_6 octahedra for $SrSnO_3$ nanoparticles is helpful for the migration of charge carriers without recombination.

3.2.2.3 Crystal structure of the perovskite photocatalysts

It has been reported that $NaTaO_3$ photocatalyst powders synthesized using a solid-state method usually formed the orthorhombic phase with a Ta-O-Ta bond angle of approximately 163°. Hu et al. compared the structures of $NaTaO_3$ powders synthesized from a sol-gel method and the conventional solid-state method.[92] The sol-gel method produced $NaTaO_3$ nanoparticles with high crystallinity at a temperature as low as 500 °C, whereas the solid-state method required a higher temperature of 1200 °C. Because of the temperature difference, the $NaTaO_3$ powders synthesized from the sol-gel and solid-state methods were of the monoclinic and orthorhombic phases, respectively.[92] The monoclinic $NaTaO_3$ has several advantages over the orthorhombic one for applications in photocatalytic reactions. Regarding the electronic structure, the monoclinic and orthorhombic phases have indirect and direct BGs, respectively. Because phonons are involved, the recombination rate for electron-hole pairs in sol-gel-prepared catalysts would be much smaller than that in a direct gap transition. In addition, the monoclinic phase was observed to have a larger number of effective states available for the photo-induced electrons and holes. The longer lifetime of the free electrons and holes is expected to increase the probability of their participation in water splitting. For the crystalline structure, the bond angle of Ta-O-Ta for the monoclinic phase was approximately 180°, a value ideal for delocalization of the excited energy in tantalate crystals. The larger surface area and the advantageous features in the electronic and crystalline structures for the monoclinic phase resulted in a remarkably higher photocatalytic activity for the sol-gel-synthesized $NaTaO_3$ than for the solid-state-synthesized material.

This journal is © The Royal Society of Chemistry 2012

Table 1 Photocatalytic activity of the selected perovskite-based photocatalysts for water splitting reaction.

No.	Photocatalyst	BG (eV)	O_2 evolution* Rate (μmol h^{-1} g^{-1})	O_2 evolution* Sacrificial reagent	H_2 evolution* Rate (μmol h^{-1} g^{-1})	H_2 evolution* Sacrificial reagent	Cocatalyst	Quantum yields	Preparation method	Light type	Ref.
1	$Sr_{2/3}Zn_{1/3}TiO_3$	3.15			732	Ethanol					
2	$Sr_{2/3}Zn_{1/3}TiO_3$	3.15	/	/	121	/	/	/	Sol-gel	UV	67
3	$Ba_{5/6}Zn_{1/6}TiO_3$	3.2			575	Ethanol					
4	$Ba_{5/6}Zn_{1/6}TiO_3$	3.2			29	/					
5	$CaNbO_2N$	2.0	10		312			1.1% at 420.5 nm			
6	$SrNbO_2N$	1.8	0	$AgNO_3$	15	Methanol	1 wt.% Pt	/	Polymerized complex	λ>420 nm	68
7	$BaNbO_2N$	1.7	0		0			/			
8	$LaNbON_2$	1.6	0		0			/			
9	Cubic $NaNbO_3$	3.29	/	/	423		/	/			
10	Orthorhombic $NaNbO_3$	3.45	/	/	241		/	/			
11	Cubic $NaNbO_3$	3.29	/	/	425	Methanol	0.5 wt.% Pt	/	Furfural alcohol derived polymerization−oxidation	λ>300 nm	69
12	Cubic $NaNbO_3$	3.29	/	/	520		1 wt.% Pt	/			
13	Cubic $NaNbO_3$	3.29	/	/	324		1.5 wt.% Pt	/			
14	$NaTaO_3$	4.0	0.78		10.3			/			
15	2 mol.% La doped $NaTaO_3$	4.09	1.7	$AgNO_3$	13.2	Methanol	/	56% at 270 nm	Solid state reaction (SSR)	λ>270 nm	70
16	$NaNbO_3$	3.08			950						
17	$KNbO_3$	3.14	/	/	100	Methanol	/	/	Hydrothermal	UV	73
18	$NaTaO_3$	3.96			36750						
19	$KTaO_3$	3.42			1040						
20	$CaTiO_3$				670.1					UV	
21	$CaTi_{0.98}Cu_{0.02}O_3$	/	/	/	5410.8	Methanol	NiO_x	/	Sol-gel coupled with ultrasonic dispersing technique		75
22	$CaTiO_3$				0					λ>400 nm	
23	$CaTi_{0.98}Cu_{0.02}O_3$				22.7						
24	Mn-doped $SrTiO_3$	2.7	9		0.67			/			
25	Ru-doped $SrTiO_3$	1.9	13	$AgNO_3$	5.7	Methanol	0.5 wt.% Pt	/	SSR	λ>440 nm	76
26	Rh-doped $SrTiO_3$	1.7	0		57.3			5.2 % at 420 nm and 6% at 365 nm			
27	Ir-doped $SrTiO_3$	2.3	1.3		27.7			/			
28	$RbLaTa_2O_7$	~3.9	3		6						
29	$RbPrTa_2O_7$	~3.6	<0.5	/	4.5	/	/	/	SSR	UV	79,80
30	$RbNdTa_2O_7$	~4.2	126.5		235						
31	$RbSmTa_2O_7$	~4.1	28.5		53						
32	2 mol.% Ca doped $NaTaO_3$	4.11	113		756						
33	2 mol.% Sr doped $NaTaO_3$	4.11	186	$AgNO_3$	830	Methanol	/	/	SSR	400 W Hg lamp	85
34	2 mol.% Ba doped $NaTaO_3$	4.09	160		696						
35	$NaTaO_3$	4.03	40		563						
36	$NaTaO_3$	4.0	~1000	/					MHT		87
37	$NaTaO_3$	4.0	~400						CHT		
38	$Sr_{0.5}TaO_3$	3.7	177	/	733	/	/	/	Direct dehydration	400 W Hg lamp	88
39	RE-$Sr_{0.5}TaO_3$	3.7	366		1400				Nanosheet processing		
40	$SrTiO_3$	/	/	/	300	Methanol	0.5 wt.% Pt	/	M13 virus template method	UV	89
41	$SrSnO_3$	4.04	/	/	57.3	/	/	/	Wet chemistry	UV	91
42	$SrSnO_3$	4.01			7				SSR		
43	$NaTaO_3$	4.1	~900	/	2050	/	/	/	SSR	400 W Hg lamp	92
44	$NaTaO_3$	4	6		13				Sol-gel		

* For clear comparison, the units of rates are also correlated to μmol h^{-1} g^{-1} by simple calculation.

The photocatalytic activities of the selected perovskite-based photocatalysts for water splitting reaction are listed in Table 1. As shown in this table, besides the choice of photocatalysts, the photocatalytic activity for water splitting reaction is also strongly dependent on the sacrificial reagent and the cocatalyst. On the whole, the addition of sacrificial reagent and the cocatalyst is helpful to improve the photocatalytic activity. Sometimes, the addition of excessive Pt cocatalyst of 1.5 wt.% could reduce the activity. A loading amount of 1.0 wt. % provided a proper cover ratio and size of cocatalyst and hence induced the highest H_2 evolution rate for the cubic $NaNbO_3$ photocatalyst. In addition, not all catalysts had high activity for both O_2 evolution and H_2 evolution reaction, and some of them showed high selectivity to the individual reaction. As shown in Table 1, $NaTaO_3$ is the most widely investigated photocatalyst and generally showed superior activity than $NaNbO_3$, $KNbO_3$ and $KTaO_3$. The effect of preparation methods and the selection of A-site elements for doping on the photocatalytic activity of $NaTaO_3$ have been intensively studied. Although nanostructure is formed in the A-site doped $NaTaO_3$ with improved activity, its BG kept unchanged, which may restrict its wide application in visible light-induced water splitting reaction. In the future, the co-doping of A-site by La, Sr, etc. and O site by N, S, etc. on $NaTaO_3$ should be an effective way to obtain both nanostructure and reduced BG. However, a reduced BG does not always bring about an improved activity. For example, $SrNbO_2N$, $BaNbO_2N$, $LaNbON_2$ with BGs lower than 2 eV showed almost no photocatalytic activity for water splitting reaction since the absolute energy position of the BG is also important for the water splitting reaction. For the $SrSnO_3$ catalyst prepared by wet chemistry method, doping in the O site should be a useful way to further enhance the activity by reducing the BG. Anyway, the doped perovskites always show low BG than the commercial TiO_2 and higher activity under visible light irradiation should be expected with perovskite catalysts. Advanced methods such as nanosheet processing, template-based methods, hydrothermal process and sol-gel process are beneficial for the achievement of high photocatalytic activity. However, nowadays, SSR is still the most investigated methods due to its convenience and more importantly, the universality. In the future, it is of great importance to improve the universality of these advanced technologies. In addition, in most of the studies mentioned in this review paper, the solar-energy conversion efficiency for this system was not presented and the presented values are very low, especially at visible light irradiation, which should be further improved in the future.

3.3 Degradation of organic dyes

As discussed previously, a semiconductor catalyst in the contaminated water can absorb solar energy to result in the formation of electron donor (reductive) sites and electron acceptor (oxidizing) sites, which facilitate the oxidation of the carbon-containing pollutants, which are oxidized into carbon dioxide, water and other anions such as nitrate, sulfate or chloride. In this section, we will focus on the material development of perovskite catalysts for the photocatalytic degradation of different dyes such as methyl orange (MO), methylene blue (MB) and rhodamine B (RB) based on the strategies for the designation of perovskite catalysts. The strategies for the development of the catalysts for degradation reactions of organic dyes are similar to those for the water splitting reaction, including band gap engineering and reducing the combination rate of the electron-hole pairs.

3.3.1 Band gap engineering

3.3.1.1 Selection and doping process of B-site elements

The undoped Ti-based perovskite always had large BGs due to the large difference of electronegativity between Ti and O. The replacement of Ti by another element with higher electronegativity such as Ni is an effective approach to reduce E_{bg}. For example, $LaNiO_3$ was synthesized using a sol-gel combustion technique for the degradation of the MO reaction under visible light.[93] The BG of $LaNiO_3$ was 2.26 eV, suggesting potential visible-light-induced photocatalytic activity, which was evaluated by the degradation of MO in water under visible light irradiation. It was observed that the photo-degradation of MO over $LaNiO_3$ was a zero-order reaction, that the rate constant k of $LaNiO_3$ was 0.152 (10^{-2} g L^{-1} h^{-1}) and that the degradation percentage after 5 h on the sample was approximately 74.9%, suggesting the effective degradation activity of MO on the $LaNiO_3$ catalysts.

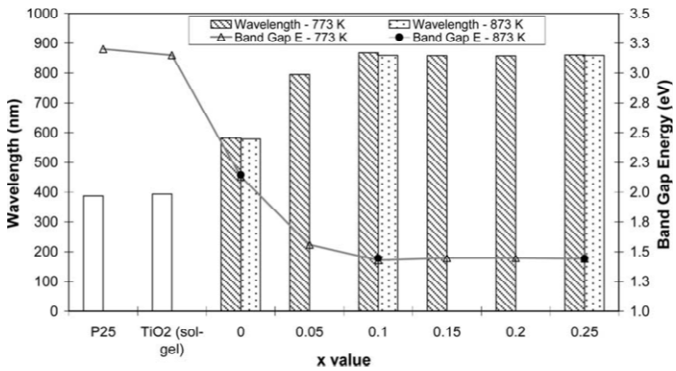

Fig. 14 Band-gap energy of various $CeCo_xTi_{1-x}O_{3+\delta}$ perovskites and TiO_2. Reproduced with permission from ref. 94. Copyright 2005, Elsevier Inc.

In addition to tailoring the B-site element, Fei et al. also studied the effect of partial substitution of the titanium cation on the photocatalytic oxidation activity for the degradation of Nile blue reaction in the $CeCo_xTi_{1-x}O_{3+\delta}$ perovskite system prepared using the sol-gel method.[94] Based on UV-vis diffuse reflectance measurements, it was observed that the perovskite catalysts exhibited significantly lower BG (1.45-2.15 eV) than P25 (3.2 eV); however, the E_{bg} remained almost unchanged at a doping level of $x > 0.1$, as shown in Fig. 14. The incorporation of 5 mol.% Co in the B site led to a reduction in BG from 2.15 eV to 1.57 eV. Using oxidative photodegradation of aqueous Nile Blue solution for activity evaluation, the

 This journal is © The Royal Society of Chemistry 2012

$CeCo_{0.05}Ti_{0.95}O_{3.97}$ perovskite was the best in the series with a conversion of 91% in the 3 hours' run and was also suitable for the solar photocatalysis because it could be activated by visible light ($\lambda < 785$ nm).

Su et al. applied a hydrothermal route for the dual substitutions of a single Cr dopant in a perovskite lattice of $NaTaO_3$ for the degradation of the MB reaction under visible light.[95] It was observed that the pure orthorhombic perovskite phase was retained regardless of the Cr^{3+} doping. The undoped $NaTaO_3$ had a BG of 4.13 eV (corresponding to a 300 nm absorption edge) with an excitation from O 2p to Ta 5d. Upon increasing the doping level of Cr^{3+}, a systematic redshift of the absorption edge and the appearance of two broad absorptions in the range 400–750 nm were observed with increased intensities. Furthermore, E_{bg} decreased from 4.13 eV for the undoped sample to 3.14 eV for the 6.39 mol.% Cr^{3+} doped sample. The absorption observed in the range of 400–500 nm was ascribed to the charge transfer from the 3d orbital of Cr^{3+} to the 5d orbital of Ta^{5+}, whereas that ranging from 550–750 nm corresponded to the d–d transition for Cr^{3+}.[96,97] The single or dual substitutions of Cr on the B site or both A site and B site depended on the doping level of Cr. Specifically, at a lower doping level of Cr^{3+} (2.47 mol.%), Cr^{3+} primarily occupied the Ta^{5+} (B site) sites, creating certain oxygen vacancies, resulting in no obvious impact on the lattice dimension but enhanced photocatalytic activities. With the further increase of the Cr^{3+} content, Cr^{3+} started to simultaneously substitute for both Na^{+} in 12-fold coordination sites and Ta^{5+} in 6-fold coordination states of the perovskite $NaTaO_3$. This dual substitution was further observed to yield a certain concentration of oxygen vacancies, a systematic decrease in lattice dimensions, an increased surface area and a decreased E_{bg}. However, the higher dopant concentration resulted in a significant decrease in the photocatalytic activity. A schematic diagram of the electronic intraband transitions of the Cr-doped $NaTaO_3$ could be speculated and is presented in Fig. 15.[95] Under visible light irradiation, electrons will be directly excited from the O 2p VB to the Ta 5d CB, corresponding to an excitation of 4.3 eV in the UV spectrum for pure $NaTaO_3$ (Fig. 15a). Accordingly, the excitation of O 2p to Ta 5d is expected to red shift due to the hybridization of Cr 3d and Ta 5d in the CB for the model of Cr@Na (Fig. 15c). In contrast, in the model of the dual substitution Cr@(Na, Ta), there may be two types of photoexcitation electrons under visible light irradiation (Fig. 15d), which may explain the two different absorptions in the long-wavelength visible region estimated from UV-vis reflectance spectra. The dual substitution yielded the mid-gap levels between the CB and VB, which resulted in the decrease in the BG energies, which is beneficial for visible-light absorption.

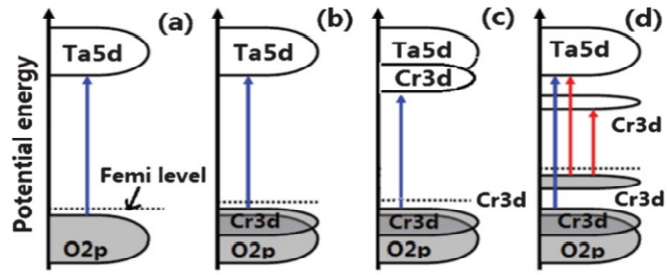

Fig. 15 A schematic diagram of the electronic intraband transition of (a) $NaTaO_3$, (b) Cr doped $NaTaO_3$ for Cr replacing Ta atom, (c) Cr doped $NaTaO_3$ for Cr replacing Na atom, (d) Cr doped $NaTaO_3$ for Cr replacing Ta and Na atoms. Reproduced with permission from ref. 95. Copyright 2012, Royal Society of Chemistry.

3.3.1.2 Selection and doping process of A-site and X-site elements

Some researchers have focused on the reduction of E_{bg} of the perovskites via selective A-site or X-site doping.[98,99] Lowering the band gaps was successfully achieved by Kumar et al. for the layered perovskite $K_2La_2Ti_3O_{10}$ because of incorporation of Sn^{2+} in the A site.[98] Visible light absorption was observed with an absorption edge red shift of approximately 100 nm from that of the parent $K_2La_2Ti_3O_{10}$. The narrowing of the BG by Sn^{2+} doping was estimated to be 2.67 eV versus 3.63 eV for the $K_2La_2Ti_3O_{10}$. The lowering of the BG can be related to the VB formation of Sn 5s and O 2p orbitals and with a CB resulting from Ti 3d orbitals. The $K_2La_2Ti_3O_{10}$ did not exhibit any visible absorption and was observed to decompose RB only under UV light. A much higher rate of degradation was observed for the Sn^{2+}-substituted sample under visible light irradiation.

Nitrogen doping has been known to shift the absorption edge toward higher wavelengths because of the contribution of N 2p orbitals to the VB comprised of O 2p orbitals, thereby moving the VB upwards. The nitrogen-doped $K_2La_2Ti_3O_{10-x}N_x$ photocatalyst was successfully prepared using conventional solid-state reactions and a wet chemical process.[99] After nitrogen doping, E_{bg} of $K_2La_2Ti_3O_{10}$ was decreased from 3.69 to 3.44 eV. The degradation of dyes under UV and visible light radiation was better with a $K_2La_2Ti_3O_{10-x}N_x$ photocatalyst than with a pure $K_2La_2Ti_3O_{10}$ photocatalyst. In addition, the $K_2La_2Ti_3O_{10-x}N_x$ photocatalyst exhibited significantly higher visible-light photocatalytic activity than pure TiO_2 (P25) in organic dye solution under visible light irradiation.

A noticeable lowering of E_{bg} has been achieved for the layered perovskite $K_2La_2Ti_3O_{10}$ as a result of the attempts made to incorporate N^{3-} ions. Nitrogen incorporation was attempted by the solid-state reaction of the parent oxide with urea at approximately 400 °C in air. Nitridation using urea resulted in not only nitrogen doping but also sensitization due to the presence of carbon nitride (CN) polymers, which resulted in visible light absorption. Simple doping of nitrogen under an ammonia atmosphere at 400 °C for 6 h in N-$K_2La_2Ti_3O_{10}$ resulted in a BG reduction from 3.63 eV ($K_2La_2Ti_3O_{10}$) to 3.59 eV (N-$K_2La_2Ti_3O_{10}$),[98] which is comparable to the earlier observed BG reduction of 3.69 eV ($K_2La_2Ti_3O_{10}$) to 3.44 eV

($K_2La_2Ti_3O_{10-x}N_x$).[99] However, CN polymers become incorporated as in the present case of CN-$K_2La_2Ti_3O_{10}$, whose UV-visible absorption spectra exhibited a larger red shift of approximately 100 nm. The BG was reduced to 2.92 eV for the CN polymer-incorporated nitrogen-doped $K_2La_2Ti_3O_{10}$. The noticeable reduction in the BG (0.71 eV) of CN-$K_2La_2Ti_3O_{10}$ could only be explained by the presence of CN polymers, rather than by simple doping of nitrogen for oxygen, suggesting a new route for the N doping for perovskites.

3.3.2 Reduction of the recombination rate of the electron-hole pair

3.3.2.1 A/B-site doping process

Many researchers have focused on developing highly active photocatalysts for the degradation of organic dyes using doping foreign elements at the A site or B site to reduce the recombination rate of electron-hole pairs by reducing the particle size.[64,65,100] Among the various doping processes, Sr and Mn were used to dope $BiFeO_3$ and $LaFeO_3$ perovskite catalysts at the A site and B site, respectively, which resulted in reduced particle sizes of the perovskite.[64,65] Using the A-site doping of Ca for $LaFeO_3$ catalysts ($La_{1-x}Ca_xFeO_3$, x=0.05-0.20) for the photocatalytic degradation of MB reaction as an example revealed that partial substitution of La^{3+} in $LaFeO_3$ with Ca^{2+} decreased the crystalline size and enhanced the visible light absorption and photocatalytic activity.[100] The 10 mol.% doping of Ca resulted in the best photoactivity among the various catalysts, and the degradation rate of MB improved from 48.9 to 77.5% after 1 hour operation with visible light after the 10 mol.% doping of calcium. Based on the results, we can see that $La_{0.9}Ca_{0.1}FeO_3$ exhibited a strong photocatalytic activity for the decomposition of MB under visible light irradiation. There are three factors that are related to the photocatalytic activity. First, the photocatalytic activity increases with increasing Ca concentration because the particle size decreases and the surface area increases, leading to an increase of the adsorption of pollutants on the photocatalyst. Second, when the La^{3+} ion was displaced by Ca^{2+} ion, Ca_{La}' donor centers and oxygen vacancies were formed. When the doping concentration was relatively low, the number of Ca_{La}' donor centers increased with the dopant concentration, resulting in an increase in the number of photoinduced electrons and an increase in the photocatalytic activity. However, when the doping concentration was too high, the dopant likely acted as an electron-hole recombination center and decreased the photocatalytic activity. Finally, the photocatalytic activity was also related to the photo absorption. It can be observed that the Ca-doped photocatalyst exhibited a larger light absorption capacity at $\lambda > 420$ nm than that of the undoped photocatalyst.

It was observed that the difference in the filled f shell of the A-site dopant also affected the recombination rate of the electron-hole pair of the perovskite catalysts. Li et al. studied the effect of the Ln element doping on the performance of $La_2Ti_2O_7$ perovskite for the photocatalytic degradation of MO reaction.[120] Nanocrystalline $La_{1.5}Ln_{0.5}Ti_2O_7$ (Ln = Pr, Gd, Er) was prepared using a polymeric complex method. Among the three doped perovskites, $La_{1.5}Gd_{0.5}Ti_2O_7$ exhibited the best photocatalytic activity, and it was assumed that the half-filled electronic configuration of Gd^{3+} promoted charge transfer and then enhanced the photocatalytic activity. The difference in the photocatalytic activity for $La_{1.5}Ln_{0.5}Ti_2O_7$ (Ln = La, Pr, Gd, Er) can be related to the different Ln 4f shell. Among the various dopants, Gd^{3+} is different from the other rare-earth ions because this ion has a half-filled f shell. The half-filled configuration of the metal ion is more stable, and this ion has a strong tendency to return to the original stable state when such a configuration is destroyed. This particular characteristic of the dopant ion with the half-filled electronic configuration can promote the charge transfer and efficiently separate the electron-hole pairs by shallowly trapping electrons.[101] Although other metal ions can also trap the photo-excited electrons, the detrapping is more difficult on these metal ions. Therefore, $La_{1.5}Gd_{0.5}Ti_2O_7$ exhibits higher efficiency in the separation and transfer of charge carriers and thus exhibits higher reactivity than other rare-earth $La_{1.5}Ln_{0.5}Ti_2O_7$ compounds (Ln = La, Er and Pr).

3.3.2.2 Preparation methods

Some researchers have observed that the preparation methods also have a strong effect on the photocatalytic activity of $LaFeO_3$ and $LaCoO_3$ perovskite catalysts for the degradation of organic dyes by reducing the possibility of the recombination of electron-hole pairs.[72,102-106] $LaFeO_3$ exhibits significant physical and chemical properties, making them of great importance for use in advanced technologies such as solid-oxide fuel cells, reforming catalysts and photocatalysis.[72,102,103] For the preparation of $LaFeO_3$, several wet chemical methods have been proposed to improve the homogeneity and reproducibility of the powders and to reduce the preparation temperature, such as sol-gel and hydrothermal methods. For example, $LaFeO_3$ nanoparticles were directly synthesized using a one-step microwave-assisted route without an additional high-temperature calcination process.[102] It was observed that the prepared $LaFeO_3$ was a single-phase perovskite with a sphere-like shape that exhibited strong visible-light absorption and an optical absorption onset of 525 nm, corresponding to a BG of 2.36 eV. These results demonstrated that $LaFeO_3$ was highly visible-light photocatalytic active for the degradation of MB. The degradation rate of MB was approximately 100% after 1 h operation with visible light, which was even much higher than the Ca-doped $LaFeO_3$ catalysts prepared by the reverse microemulsion method under the same conditions, suggesting the effective improvement in activity by adopting the microwave-assisted route. However, nanosized $LaFeO_3$ photocatalysts were also synthesized with a sol-gel method for the photo-degradation of the RB reaction under visible light irradiation. The activity of the as-prepared $LaFeO_3$ was much higher than that of commercial Degussa P25 TiO_2 under visible irradiation, and the degradation rate of RB on the $LaFeO_3$ after sintering at 500 °C was approximately 8 times higher than that of P25 TiO_2.

In addition to the aforementioned methods, the hydrothermal method has been widely used for the preparation of nanosized $LaFeO_3$ perovskite with the advantages of a well-controlled size, low temperature growth, cost effectiveness and

 This journal is © The Royal Society of Chemistry 2012

less complicated product. Thirumalairajan et al. successfully synthesized microspheres composed of $LaFeO_3$ nanoparticles with an orthorhombic structure via a citric-acid-assisted hydrothermal method.[103] The morphological analysis suggested that microspheres with diameters of 2-4 μm composed of nanoparticles with an average size of 85 nm were formed. The absorption edge at 600 nm emphasized the fact that $LaFeO_3$ could serve as a potential visible-light-driven photocatalytic catalyst for the degradation of RB aqueous solution with good photocatalytic activity. The formation mechanism of the $LaFeO_3$ microspheres is schematically illustrated in Fig. 16.[103] In the initial stage of the hydrothermal reaction, metal ions in the solution reacted with citric acid to form relatively stable distorted primary particles of $LaFeO_3$ under supersaturated condition, which decreased the free metal ion concentration in solution and resulted in the slow generation of primary particles. Generally, the Ostwald ripening process involves the formation of aggregates with primary crystallites through the crystallization process due to the energy difference. The formed $LaFeO_3$ nanoparticles aggregated together, driven by the minimization of the interfacial energy. The aggregated nanoparticles would act as primary cores that favor the homogenous assembly to produce larger self-assembled aggregates via the self-assembly process. The aggregated particles tend to form a spherical shape, as the aggregation speed of the nanoparticles from each direction to the core could be same. The effect of the reaction time and calcination temperature on the $LaFeO_3$ microsphere morphology also supports the finding that the Ostwald ripening effect is the essential mechanism.

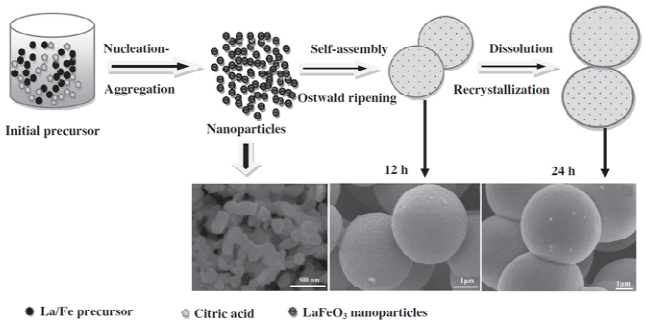

Fig. 16 Schematic representation of formation mechanism of $LaFeO_3$ microspheres. Reproduced with permission from ref. 103. Copyright 2012, Elsevier Inc.

$LaFeO_3$ nanostructures such as nanocubes, nanorods and nanospheres, tailored using different surfactants, were successfully synthesized using the hydrothermal process by Thirumalairajan et al.;[72] the authors considered that the possible growth mechanism of the formation of $LaFeO_3$ nanostructures was mainly based on the self-assembly growth mechanism occurring due to the localized Ostwald ripening process. The morphologies of the $LaFeO_3$ nanostructures synthesized by hydrothermal reactions with and without structure-directing agents are shown in Fig. 17.[72] The cube-like $LaFeO_3$ morphology was obtained by direct hydrothermal synthesis without the use of any structure-directing agents. These cube-like structures have sharp edges and a smooth surface, as illustrated in Fig. 17a. When urea was used as a structure-directing agent, nanorods of $LaFeO_3$ were obtained, as shown in Fig. 17b. The use of another structure-directing agent, citric acid, resulted in sphere-shaped nanostructures with an average size of 52 nm, as shown in Figs. 17c&d. The enhanced photocatalytic activity for the degradation reaction of RB on the $LaFeO_3$ nanospheres compared with other nanostructures and P25 TiO_2 can be ascribed to the high specific surface area, pore size distribution and smaller particle size.

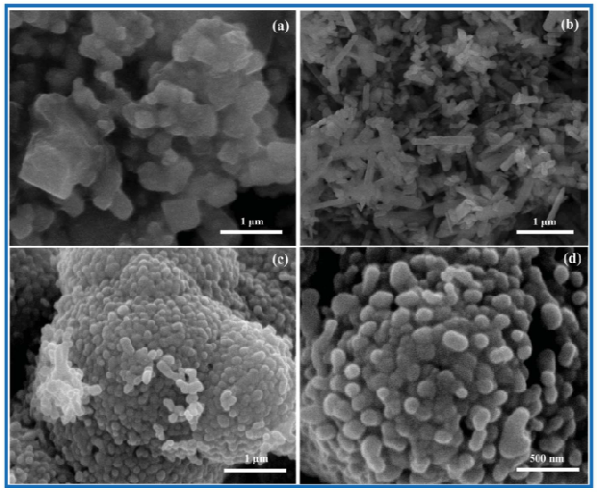

Fig. 17 SEM images of three different $LaFeO_3$ morphologies (a) nanocubes, (b) nanorods and (c and d) low and high magnifications of nanospheres. Reproduced with permission from ref. 72. Copyright 2013, Royal Society of Chemistry.

Completely replacing Fe with Co led to the formation of $LaCoO_3$ perovskite oxides, which have attracted considerable attention for the degradation of organic dye reactions.[104,105] Jung and Hong studied the photocatalytic activity for the decomposition of MO on $LaCoO_3$ oxides prepared using different methods, such as the microwave method, malic acid method, and solid-state reaction method, on the photocatalytic performance of the $LaCoO_3$ catalysts.[104] The $LaCoO_3$ catalyst prepared using the microwave-assisted process exhibited the highest activity at the same sintering temperature. Specifically, the rate constant k of $LaCoO_3$ prepared with the microwave-assisted process was 1.7 and 40 times higher than that of the catalysts prepared by the malic acid method and solid-state reaction method, respectively. Fu et al. reported a simple method to synthesize perovskite-type $LaCoO_3$ hollow nanospheres at a relatively low calcination temperature at 550 °C by utilizing the carbonaceous colloids as template and internal heat sources.[105] The formation process of perovskite-type $LaCoO_3$ hollow spheres, which can be divided into two steps, is illustrated in Fig. 18.[105] The carbonaceous colloid template is hydrophilic and negatively charged and is prepared from a saccharide solution and functionalized with OH and C@O groups with large surface area and nano-scale pores distributed uniformly on its surface. First, carbon@LaCo are formed through the surface-layer-adsorption process: the

functional groups and nano-scale pores in the surface layer are able to bind or capture La^{3+} and Co^{2+} cations through coordination or electrostatic interactions upon dispersal of the carbonaceous spheres in the solution with $[La^{3+}]:[Co^{2+}] = 1:1$. The sequential removal of the carbon cores, densification, cross-linking, and phase transformation of La and Co in the layer via a calcination process resulted in the formation of $LaCoO_3$ hollow spheres. It was also clearly demonstrated that the carbonaceous polysaccharide microspheres played a dual-functional role as templates and internal heat sources in the formation process, which could be attributed to the low-temperature formation of the perovskite-type structure at as low as 550 °C. The $LaCoO_3$ hollow spheres exhibited a broad and strong absorption at 220-550 nm regions with a narrow BG of 2.07 eV. The $LaCoO_3$ hollow nanospheres also exhibited excellent photocatalytic activity for the degradation of MB, MO and neutral red, which is comparable to P25 after 100 min reaction, making it a promising candidate for environmentally friendly applications such as the treatment of wastewater.

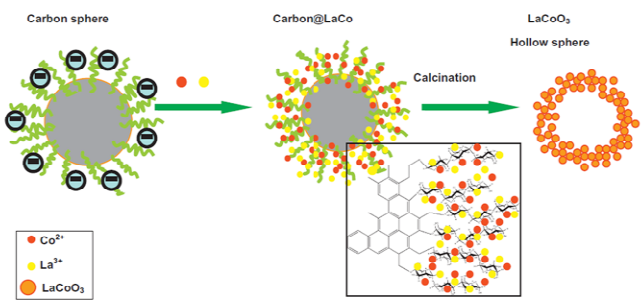

Fig. 18 Illustration of the formation process for perovskite-type $LaCoO_3$ hollow spheres. Reproduced with permission from ref. 105. Copyright 2013, Elsevier Inc.

3.3.2.3 Crystal structure

Zhang et al. prepared Cu-doped KNb_3O_8 photocatalysts using a simple solid-state method and observed that the doping of Cu affected the crystal structure, morphology and E_{bg}.[106] It was suggested that Cu doping can induce the formation of the compound $K_6Nb_{10.8}O_{30}$ with tungsten-bronze structure and that the relative content of $K_6Nb_{10.8}O_{30}$ in the Cu-doped samples increased with Cu doping amount. When the Cu doping amount reached 2 wt.%, the as-prepared sample mainly consisted of $K_6Nb_{10.8}O_{30}$.[106] Fig. 19 presents SEM images of the as-prepared samples undoped or doped with Cu. In general, the crystal morphology of KNb_3O_8 was flake-like and that of the crystal of $K_6Nb_{10.8}O_{30}$ assumed a quadrate column shape. According to Fig. 19, the crystal sizes increased and more uniform quadrate crystals formed with increasing Cu doping amount. This result indicates that the Cu doping promoted the increase of the crystal sizes and the uniformity of the shape. The Cu dopant increased the absorption of the Cu-doped KNb_3O_8 samples in the visible light region and the red-shift of the absorption edge of the samples.

The photocatalytic properties of the catalysts were evaluated using the degradation of acid red G. The results indicated that Cu doping significantly increased the photocatalytic activity of the KNb_3O_8 catalyst. After UV irradiation for 60 min, the photodegradation rate of acid red by the KNb_3O_8 catalyst was 63.03%. For the KNb_3O_8 catalysts doped with 0.3, 0.5, 1 and 2 wt.% Cu, the photodegradation rates of acid red G increased to 93.23, 93.06, 93.63 and 83.92%, respectively.[106] The authors considered that the enhanced photocatalytic activity could be attributed to three causes. First, the layered materials KNb_3O_8 used their interlayer space as reaction sites, where the electron-hole recombination process could be retarded by the physical separation of electron and hole pairs and Cu(II) ions likely entered into the interlayer spaces, which acted as receptors or transmitters of photogenerated electrons to inhibit the recombination and extend the lifetime of the charge carrier. Second, Cu doping induced the formation of the compound $K_6Nb_{10.8}O_{30}$. Both the CB bottom and the VB top of $K_6Nb_{10.8}O_{30}$ lay below the CB bottom and VB top of KNb_3O_8, respectively. Under UV-light irradiation, an electron at the CB bottom of KNb_3O_8 migrated to that of the $K_6Nb_{10.8}O_{30}$. Moreover, a hole at the VB top of the $K_6Nb_{10.8}O_{30}$ migrated to that of KNb_3O_8.[106] In this manner, the formed nanostructure heterojunction on $K_6Nb_{10.8}O_{30}$ and KNb_3O_8 led to a more efficient interelectron transfer, which played an important role for the enhanced photocatalytic activities. Third, the highly distorted surface NbO_6 octahedral sites played an important role in heterogeneous catalysis. Cu(II) ions could enter into NbO_6 octahedral sites and increase the photocatalytic effect of the catalyst by enhancing the distortion of the NbO_6 octahedral sites and the mobility of active oxygen in the crystal structure of the catalyst.

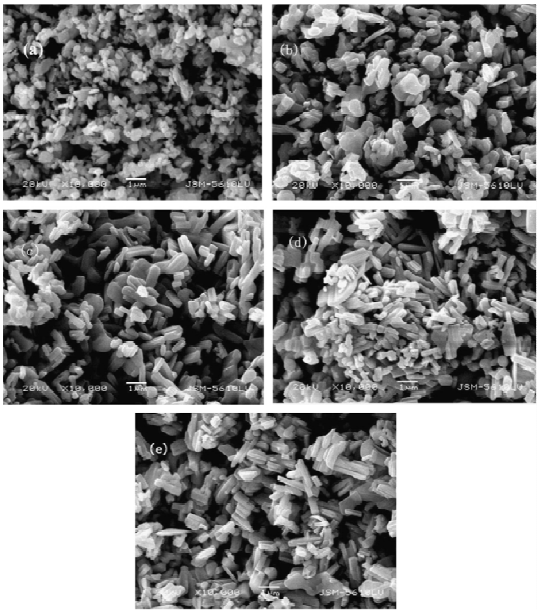

Fig. 19 SEM images of the as prepared samples: (a) KNb_3O_8; (b) 0.3 wt.% Cu-doped; (c) 0.5 wt.% Cu-doped; (d) 1 wt.% Cu-doped and (e) 2 wt.% Cu-doped. Reproduced with permission from ref. 106. Copyright 2011, Elsevier Inc.

This journal is © The Royal Society of Chemistry 2012

Table 2 Photocatalytic activity of the selected perovskite-based and P25 photocatalysts for degradation of organic dyes.

No.	Photocatalyst	BG (eV)	Dye types and/or concentration	Degradation rate (1-C/C_0, %)	Catalyst loading	Light type	Preparation method	Ref.
1	P25	3.2	RB, 20 μmol L^{-1}	3	5 g L^{-1}	λ>400 nm	Commercial	71
2	$LaFeO_3$(500)	/		24			Sol-gel	
3	$LaFeO_3$(600)			16				
4	$LaFeO_3$(700)			13				
5	$LaFeO_3$(800)			9				
6	$LaFeO_3$ nanocube	2.01	RB	76.81 at 180 min	1 g L^{-1}	λ>400 nm	Hydrothermal	72
7	$LaFeO_3$ nanorod	2.05		88.36 at 180 min				
8	$LaFeO_3$ nanosphere	2.1		90.8 at 180 min				
9	P25	3.2		5.1 at 180 min			Commercial	
10	$LaNiO_3$	2.26	MO, 10 mg L^{-1}	74.9 at 5 h	2 g L^{-1}	λ>400 nm	Sol-gel	93
11	$CeCo_{0.05}Ti_{0.95}O_{3.97}$	1.57	Nile Blue, 30 ppm	91 at 3 h	3 g L^{-1}	254-310 and 410-500 nm	Sol-gel	94
12	$NaTaO_3$	4.13	MB, 2×10^{-4} mol L^{-1}	60 at 200 min	50 mg	λ>420 nm	Hydrothermal	95
13	2.47 mol.% Cr doped $NaTaO_3$	3.95		70 at 200 min				
14	6.35 mol.% Cr doped $NaTaO_3$	3.28		~35 at 200 min				
15	P25	3.2	RB, 5×10^{-6} mol L^{-1}	75 at 150 min	2 g L^{-1}	λ>400 nm	Commercial	98
16	$K_2La_2Ti_3O_{10}$	3.63		10 at 150 min			SSR	
17	N-$K_2La_2Ti_3O_{10}$	3.59		20 at 150 min			SSR+NH_3 gas	
18	CN-$K_2La_2Ti_3O_{10}$	2.92		90 at 150 min			SSR+urea	
19	P25	3.2	MO, 0.02 g L^{-1}	~6 at 30 min	0.8 g L^{-1}	λ>400 nm	Commercial	99
20	$K_2La_2Ti_3O_{10}$	3.69		~2 at 30 min			SSR	
21	N-$K_2La_2Ti_3O_{10}$	3.44		~30 at 30 min			SSR+NH_3 gas	
22	$LaFeO_3$	/	MB, 10 mg L^{-1}	~50 at 90 min	0.5 g L^{-1}	λ>400 nm	Reverse microemulsion	100
23	$La_{0.9}Ca_{0.1}FeO_3$			~80 at 90 min				
24	$La_2Ti_2O_7$	/	MO, 1×10^{-5} mol L^{-1}	~55 at 90 min	1 g L^{-1}	UV, λ=254 nm	Polymeric complex	101
25	$La_{1.5}Pr_{0.5}Ti_2O_7$			~25 at 90 min				
26	$La_{1.5}Gd_{0.5}Ti_2O_7$			90 at 90 min				
27	$La_{1.5}Er_{0.5}Ti_2O_7$			~50 at 90 min				
28	$LaFeO_3$	2.36	MB, 10 mg L^{-1}	~100 at 90 min	2 g L^{-1}	λ>400 nm	Microwave-assisted route	102
29	P25	3.2		20 at 90 min			Commercial	
30	$LaFeO_3$	2.1	RB	>90 at 180 min	1 g L^{-1}	λ>400 nm	Hydrothermal	103
31	P25	3.2	MO, 10 mg L^{-1}	~85 at 100 min	0.2 g L^{-1}	UV	Commercial	105
32	$LaCoO_3$	2.07		~85 at 100 min			Surface-ion adsorption method	
33	P25	3.2	MB, 10 mg L^{-1}	~85 at 100 min			Commercial	
34	$LaCoO_3$	2.07		~85 at 100 min			Surface-ion adsorption method	
35	KNb_3O_8	3.06	Acid red G, 50 mg L^{-1}	63.03 at 60 min	1 g L^{-1}	UV, λ=253.7 nm	SSR	106
36	0.3 wt.% Cu doped KNb_3O_8	/		93.23 at 60 min				
37	2 wt.% Cu doped KNb_3O_8			83.92 at 60 min				

The photocatalytic activity of the selected perovskite-based and P25 photocatalysts for degradation of organic dyes are listed in Table 2. In addition to the choice of photocatalysts, the photocatalytic activity for degradation of organic dyes is also strongly dependent on the types and concentration of the dye and the loading of the catalyst in the solution. Under visible light irradiation, the investigated perovskite catalysts always show much better performance than the commercial TiO_2 (P25). For a $LaFeO_3$ catalyst, the calcination temperature, morphology, preparation methods have strong influence on its photocatalytic activity for degradation of organic dyes in solution. CN-$K_2La_2Ti_3O_{10}$ was found to be more active than the N-$K_2La_2Ti_3O_{10}$, which is higher than P25 under visible light irradiation for the degradation of RB. The successful doping of CN in $K_2La_2Ti_3O_{10}$ by urea using a SSR method suggests a facile way to prepare N-doped perovskites and also some non-

perovskite materials such as TiO_2. In addition, the selection of A-site element and the phase structure control are also essential for the achievement of high photocatalytic activity. When Cr^{3+} is used as a dopant for $NaTaO_3$, the amount of Cr^{3+} should be well controlled because excessive Cr^{3+} would lead to a sharp decrease in the photocatalytic activity. In addition, Cr^{3+} could function as A-site or B-site dopant depending on the amount, which may provide a new aspect to develop new photocatalysts with enhanced the photocatalytic activity. The $LaCoO_3$ prepared by a surface-ion adsorption method showed comparable activity with P25 under UV light irradiation for the degradation of MO and MB. Due to its lower BG, it should be expected that much higher activity under visible light irradiation should be obtained as compared with P25.

4. Perovskite materials in energy-related photovoltaic reactions (solar cells)

Within the past 2 years, the efficiencies of hybrid organic-inorganic perovskite solar cells have increased to over 15%. These solar cells are solution-processable, inexpensive and composed of earth-abundant materials, making them promising candidates for highly efficient and low-cost solar power generation systems. In this section, first of all, some strategies used to design perovskite light absorbers in solar cells are given and related perovskite designation is also presented in detail.

4.1 Strategies to design perovskite light absorbers in solar cells

4.1.1 Band gap engineering

Materials for solar light harvesting are diversified; however, the good candidates all have a common feature: broad and strong absorption over the visible to near infrared region of the solar spectrum. It is believed that semiconductors with a BG below 1.1 eV are suitable for solar light absorption. However, if the BG is too narrow, the cell will collect extra current with a reduction in the voltage. Through a trade-off of these two effects, the optimal BG is approximately 1.4 eV for a solar cell prepared from a single material. Researchers have observed that the BG of perovskite materials will decrease with (1) a decrease of the difference in the effective electronegativity between the metal (B site) cation and the anion, (2) a decrease of the electronegativity of X site anions, (3) an increase of the dimensionality of the BX_6 network, and (4) an increase of the angle of the B–X–B bonds.[107]

4.1.1.1 Decrease of the difference in electronegativity between B site cation and anion

Some perovskite oxides, such as alkaline-earth metal titanates ($ATiO_3$, A = Ca, Sr, Ba), have wide BGs (3-5 eV) due to the large difference in electronegativity between the oxygen and titanium atoms (3.5 vs. 1.5).[108] By modifying the composition by reducing the difference in electronegativity between oxygen and the B site element in the perovskite, a low BG of 2.7 eV was obtained for $BiFeO_3$ perovskite due to the higher electronegativity of Fe than Ti.[109] In addition, for the $CH_3NH_3PbI_3$ system, due to the smaller difference in electronegativity between I and Pb atoms (2.5 vs. 1.9), the BG value of $CH_3NH_3PbI_3$ was reported to be only approximately 1.55 eV, which is much lower than that of the $ATiO_3$ system.

4.1.1.2 Decrease of the electronegativity of anions

For $CH_3NH_3PbX_3$, experimental studies have demonstrated that absorption was shifted to the blue region by moving from I to Br to Cl. For example, $CH_3NH_3Pb(I_{1-x}Br_x)_3$ exhibited blue-shifted absorption compared with that of $CH_3NH_3PbI_3$ because the electronegativity of the I anion was lower than that of the Br anion.[110,111]

4.1.1.3 Increasing the dimensionality of the BX_6 network

The variation of the A site cation can affect the optical properties by deforming the BX_6^{4-} octahedron network. A larger or smaller A cation can cause the entire lattice to expand or contract and lead to a change of the B–X bond length, which has been demonstrated to be important in the determination of the BG. If the cation is over-sized, the three-dimensional (3D) perovskite structure is unfavorable, and more stable lower-dimensional layered or confined perovskites will be formed. For example, an ethylammonium-cation-based perovskite, which had been explored previously in solar cells, was demonstrated to form a perovskite with a wider BG due to a 2H-type structure.[112] Thus far, it has been demonstrated that small monovalent cations, such as Cs^+, methylammonium (MA^+), or formanidinium (FA^+), can form a 3D framework with the PbI_6 network.[113] Fujisawa et al. have demonstrated a self-assembled one-dimensional (1D) perovskite material methylviologen $(MV)Pb_2I_6$ as a light absorber for perovskite-based solar cells.[114] It was observed that $MVPb_2I_6$ had a higher BG of 2-3 eV due to the 1D structure.

4.1.1.4 Increasing the angle of B–X–B bonds

As mentioned above, the B–X–B bond angle has the greatest impact on tuning the BG for each individual metal. Using ABI_3 (B = Ge, Sn, Pb) as an example, the B–I–B bridging angles between the BI_6 octahedra are 166.27(8)° for Ge, 159.61(5)° for Sn, and 155.19(6)° for Pb.[115] In addition, with the downward selection of the metal cation, a decrease of the covalent character of the B–I bond was observed, meaning an increased difference between the electronegativity of the two atoms. Therefore, the BG of the perovskites follows the trend of $AGeI_3$ < $ASnI_3$ <$APbI_3$. It was reported that the doping Pb with Sn $CH_3NH_3PbI_3$ resulted in a reduced BG.[116]

4.1.2 Diffusion length of the electron-hole pair

The diffusion length plays a key role in the photovoltaic performance of perovskite solar cells, limiting the active layer thickness to a few hundred nanometers. To study the accumulation of a photogenerated charge and charge separation, tremendous efforts were devoted to characterize these different processes occurring in the perovskite layer by measuring the L_d in prepared samples or complete devices and the lifetime. Some researchers have reported the diffusion-length measurements performed on hybrid perovskites, which shed light on the dynamics of photoexcited species in these materials.[117,118] It was found that $CH_3NH_3PbI_{3-x}Cl_x$, had an L_d for electrons and holes exceeding 1 μm as compared with an L_d of approximately 100 nm was obtained with $CH_3NH_3PbI_3$.[117,118] This high value provided hope for the future study of

This journal is © The Royal Society of Chemistry 2012

hybrid perovskite solar cells by making the fabrication of devices with thicker active layers possible, where the absorption of light can be increased without affecting the collection efficiency of the generated charges.

4.1.3 Crystallinity and morphology control of the perovskite

In addition to the above-mentioned factors, the fabrication techniques of the perovskite layer also have a strong effect on the cell performance of the perovskite-based solar cells. The photovoltaic performance of the devices with perovskite light absorber is greatly dependent on the film morphology, which in turn is related to the deposition techniques and subsequent treatments employed. To improve the performance of the thin-film devices, a delicate control of their grain structures is required, and several advanced preparation methods such as spin coating, vapor-assisted solution process and surface passivation, etc. were developed recently.[119-125]

Currently, researchers are mainly focused on high performance via the selection and modification of perovskite-based light absorbers and related HTMs fabrication methods. In addition, inorganic perovskites have also been exploited as photoanodes in DSSCs with some excellent results available. In this section, we will focus on the development of perovskite materials in light absorbers and photoanodes based on the proposed strategies mentioned above and then provide some guidelines for the further improvement of perovskite-based solar cells. Shown in Fig. 20 are the schematics of the high-level summary of Section 4.

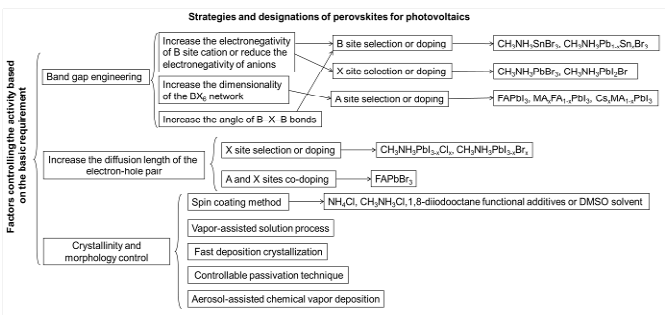

Fig. 20 The schematics of the high-level summaries of Section 4.

4.2 Development of $CH_3NH_3PbI_3$-based light absorbers

4.2.1 Basic structural and electronic properties

The structural and electronic properties of the perovskite $CH_3NH_3PbI_3$ materials have been well studied using theoretical calculations and Raman spectroscopy.[126-128] First-principle DFT calculations have been performed to study the structural and electronic properties of orthorhombic perovskite $CH_3NH_3PbI_3$ materials.[126] In Fig. 21, the atomic structures of orthorhombic perovskite $CH_3NH_3PbI_3$ crystals without (left) or with (right) PbI_6 octahedra are shown. These structures demonstrate that the main interaction between the organic groups and inorganic framework is through the ionic bonding between CH_3^+ cations and I^- anions. The different interaction strengths between I atoms with their adjacent atoms cause the formation of two types of I atoms in the Pb-I framework. The analysis of electronic properties also suggested that orthorhombic $CH_3NH_3PbI_3$ was a direct-BG crystal with the minimum BG at the G symmetry point. During light harvesting, I 5p electrons could be photo-excited to Pb 6p empty states. The theoretical study presents some guidelines for further theoretical studies on this type of organic-inorganic hybrid perovskite materials for sensitized solar cells. Quarti et al. have reported the resonant Raman spectrum of the widely used $CH_3NH_3PbI_3$ perovskite measured between 60 and 450 cm^{-1}, assigning its main vibrational features with the help of electronic structure calculations.[128] The measured spectrum assignment was assisted by DFT simulations of the Raman spectra of suitable periodic and model systems. Important markers of the inorganic component have been observed at 60 and at 94 cm^{-1}, which were mainly associated with the I-Pb–I bending and Pb–I stretching. The region between 100 and 200 cm^{-1} was instead associated librational motions of the CH_3NH_3 cations. Based on the electronic structure calculations, it was observed that the interactions between the organic cations and the inorganic counterpart affected the vibrational frequency and Raman intensity of the CH_3NH_3 torsional mode in $CH_3NH_3PbI_3$. The broad and unresolved band at 200-340 cm^{-1} was consequently assigned to the torsional mode of the CH_3NH_3 cations, and this mode was proposed as a possible marker of the orientational order of the organic cations in the material and thus of the entire crystal. The study could provide the required assignments for the interpretation of the Raman spectra of organohalide perovskites, which may be extremely useful to understand the properties of CH_3NH_3 and its applications in solar cells.

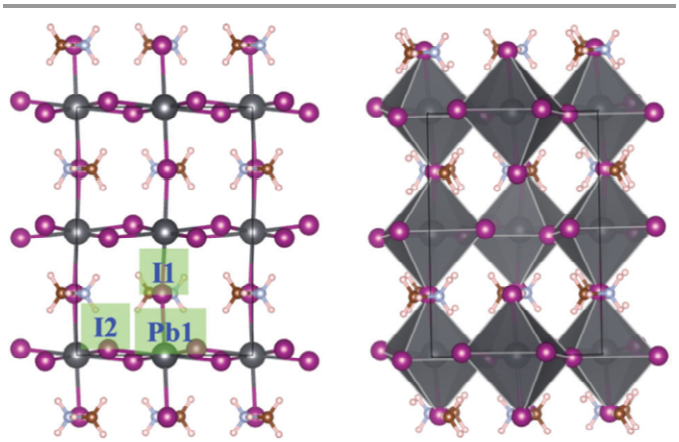

Fig. 21 Atomic structures of orthorhombic perovskite $CH_3NH_3PbI_3$ crystals without (left) or with (right) the $[PbI_6]$ octahedra. Key: grey-Pb, purple-I, light blue-N, brown-C and pink-H. Reproduced with permission from ref. 126. with permission from the PCCP Owner Societies, Copyright 2014.

4.2.2 Band gap engineering

4.2.2.1 Selection and doping of X-site elements

As mentioned above, the electronegativity of X-site elements has a strong effect on the E_{bg} of perovskite. In principle, doping of the X site of $CH_3NH_3PbI_3$ with Br could result in an increase in E_{bg}, which decreases the PCE of the solar cells. However, it was observed that the substitution of I with Br with the

formation of $CH_3NH_3PbBr_3$ improved the V_{oc} of the solar cells, although η was not increased or even reduced to some extent due to the increased BG.[111,129] For example, Kojima et al. observed that the replacement of I by Br dramatically improved V_{oc} from 0.61 to 0.96 V. The high V_{oc} of the bromide ($CH_3NH_3PbBr_3$) was associated with the higher CB of the bromide relative to that of the iodide. However, the PCE reduced from 3.8 to 3.2% with the replacement of Br because J_{sc} was greatly reduced in the $CH_3NH_3PbBr_3$-based cell, which could be attributed to the lower capability of light adsorption as well as the increased E_{bg} of $CH_3NH_3PbBr_3$.[111]

To achieve both high V_{oc} and generated photocurrent, partial replacement of I by Br may be a useful strategy.[130-132] $CH_3NH_3PbI_2Br$ was synthesized by Qiu et al. and used as a visible light absorber to sensitize 1D TiO_2 nanowire arrays (NWAs) for all-solid-state solar cells.[130] Higher V_{oc} (0.82 V vs. 0.74 V) and PCE (4.9% vs. 4.3%) values were achieved by Br-substitution in $CH_3NH_3PbI_3$. Aharon et al. also studied the effect of Br doping on the photo activity and operational stability of $CH_3NH_3PbI_3$ perovskite.[131] The hybrid perovskite was deposited by a two-step deposition technique, enabling control of the perovskite composition and its BG. The best hybrid $CH_3NH_3PbI_2Br$ perovskite solar cell achieved a PCE of 8.54%, higher than the values of $CH_3NH_3PbI_3$ (7.2%) and $CH_3NH_3PbBr_3$ (1.69%). In addition, an improved stability was achieved for this hybrid perovskite compared with that of $CH_3NH_3PbI_3$ without the Br substitution.

Hybrid organometallic halide perovskite $CH_3NH_3PbI_2Br$ nanosheets with a BG of 1.8 eV were prepared using a thermal decomposition process from a precursor containing PbI_2, CH_3NH_3Br and CH_3NH_3Cl.[132] This process affected not only the phase evolution of $CH_3NH_3PbI_2Br$ but also the morphologic shape and surface coverage of perovskite films on the planar substrate and then strongly affected the performance of the solar cells. The solar cell with $CH_3NH_3PbI_2Br$ nanosheets exhibited a PCE of 10% and a single-wavelength conversion efficiency of up to 86%. It was observed that CH_3NH_3Cl functions as a glue or soft template to control the initial formation of a solid solution with the main $CH_3NH_3PbI_2Br$ precursor components (i.e., PbI_2 and CH_3NH_3Br). BG tuning of mixed anion lead halide perovskites $CH_3NH_3Pb(I_{1-x}Br_x)_3$ ($0<x<1$) has been demonstrated by Kulkarni et al. using a sequential deposition process.[110] The PbI_2 film dipping time in halide precursors as well as the concentration of halide precursors was observed to play a crucial role in determining the composition and thus the E_{bg} of mixed halide perovskites. A systematic shift of the absorption band edge to shorter wavelengths was observed with increasing Br content in the perovskite, which results in the decrease in the photocurrent.

Chung et al. demonstrated that doping inorganic perovskite $CsSnI_3$ with 5% fluorine could dramatically improve the photocurrent density by nearly 40%.[133] Importantly, Mosconi et al. demonstrated that the mixed halide perovskite system consisted of two different structures, the stability of which decreased from I^- to F^- along column VIIA in the periodic table.[134] Therefore, it is difficult to stabilize I^-- and F^--based mixed halide perovskite systems, making F^- a non-ideal dopant for $CH_3NH_3PbI_3$ perovskite. Nagane et al. have reported an interesting strategy to incorporate F^- in the perovskite structure via partial substitution of I^- by BF_4^-.[135] Importantly, I^- and BF_4^- both have nearly the same ionic radius, making the incorporation of BF_4^- feasible in the structure. The BF_4^- substituted perovskite exhibited significant enhancement in electrical conductivity at low frequencies (one order of magnitude) and improved photo-response under AM1.5 illumination (more than four orders of magnitude) compared with the $CH_3NH_3PbI_3$ perovskite, although E_{bg} was increased to a relatively higher value. This study provides a new approach to improve the electricity and photo-response for the $CH_3NH_3PbI_3$ perovskite.

4.2.2.2 Selection and doping of B-site elements

The toxicity of lead is one concern about the use of $CH_3NH_3PbI_3$; thus, a key scientific challenge is to replace the lead with a less toxic metal. However, limited such studies in the literature have been reported.[116,136,137] The most viable replacements for Pb in the perovskite material are Sn and Ge because these metals have larger X-B-X angles as mentioned above, which are beneficial for reducing E_{bg}. However, the major problem with the use of these metals is their chemical instability in the required oxidation state. A recent study by Ogimi et al. reported a mixed metal, Sn-Pb, perovskite that enabled the tunability of the BG of the perovskite absorber by varying the Sn:Pb ratio, indicating that Sn could be a good choice for the metal ion, especially for lower BG solar cells.[116] The best performance was obtained using $CH_3NH_3Sn_{0.5}Pb_{0.5}I_3$ perovskite and a PCE of 4.18% with V_{oc} of 0.42 V, FF of 0.50 and J_{sc} of 20.04 mA cm^{-2} was reported. The edge of the incident photon to the current efficiency curve reached 1060 nm, which was red-shifted by 260 nm compared with that of the $CH_3NH_3PbI_3$ perovskite. However, the same study reported that the $CH_3NH_3SnI_3$ perovskite did not exhibit significant photovoltaic properties as shown in Fig. 22 and that a minimum content of Pb was needed to stabilize the Sn^{2+} oxidation state.

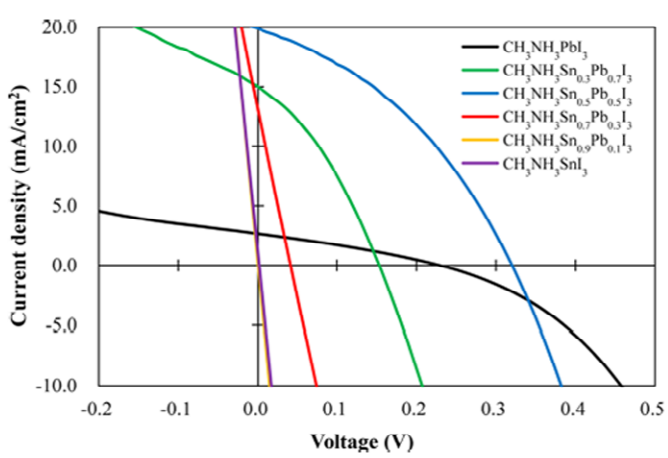

Fig. 22 I–V curves for $CH_3NH_3Sn_xPb_{(1-x)}I_3$ perovskite solar cells. Composition: $CH_3NH_3Sn_xPb_{(1-x)}I_3$/P3HT. Solar cells were measured under 100 mW/cm^2 (AM 1.5G) light illumination with masked area 0.4 mm × 0.4 mm. Reproduced with permission from ref. 116. Copyright 2014, American Chemical Society.

This journal is © The Royal Society of Chemistry 2012

Hao et al. studied the performance of perovskite solar cells based on alloyed perovskite solid solutions of methylammonium tin iodide and its lead analogue ($CH_3NH_3Sn_{1-x}Pb_xI_3$).[136] E_{bg} of the mixed Pb/Sn compounds did not follow a linear trend (Vegard's law) in between these two extremes of 1.55 and 1.35 eV but had a narrower BG (<1.3 eV), thus extending the light absorption into the near-infrared region (1050 nm). These results were confirmed via optical measurements of the materials, and for example, an optimal short-circuit photocurrent density over 20 mA cm^{-2} was obtained for the mixed alloy $CH_3NH_3Sn_{0.5}Pb_{0.5}I_3$ under AM 1.5G simulated sunlight of 100 mW cm^{-2}. The anomalous trend in the BG of $CH_3NH_3Sn_xPb_{1-x}I_3$ was the same as the trend observed in $Pb_{1-x}Sn_xTe$. In this system, a band inversion occurred with varying x, which was associated with a systematic change in the atomic orbital composition of the CBs and VBs. This result occurred because the CBM in SnTe had a similar orbital composition as the VBM in PbTe and vice versa, which could be attributed to the anomalous trend rather than the expected Vegard's law trend in E_{bg}. An in-depth understanding of this unique effect, which is responsible for being able to significantly extend the solar absorption spectrum of the perovskite-based systems, will require careful electronic band structure calculations. In addition, the Sn doping in $CH_3NH_3PbI_3$ could also affect the morphology of the thin film. Fig. 23 shows two representative SEM images of $CH_3NH_3PbI_3$ and $CH_3NH_3Sn_{0.5}Pb_{0.5}I_3$ films on mesoporous TiO_2 electrodes. The $CH_3NH_3PbI_3$ film was composed of interconnected nanoscale domains with sizes ranging from 200 to 500 nm with good film coverage. However, the $CH_3NH_3Sn_{0.5}Pb_{0.5}I_3$ film displayed superior film quality and coverage. Compared with the $CH_3NH_3PbI_3$ film, the contrast features apparent in the hybrid $CH_3NH_3Sn_{0.5}Pb_{0.5}I_3$ film suggest the formation of smaller crystallite domains, implying a more efficient film formation via favorable crystal growth of the mixed-metal perovskite. Fig. 23c presents elemental maps of Pb, Sn, and I in the $CH_3NH_3Sn_{0.5}Pb_{0.5}I_3$ film obtained via SEM-energy dispersive spectroscopy (EDS). It is apparent that Sn and Pb are homogeneously distributed throughout the film with no evident phase separation.

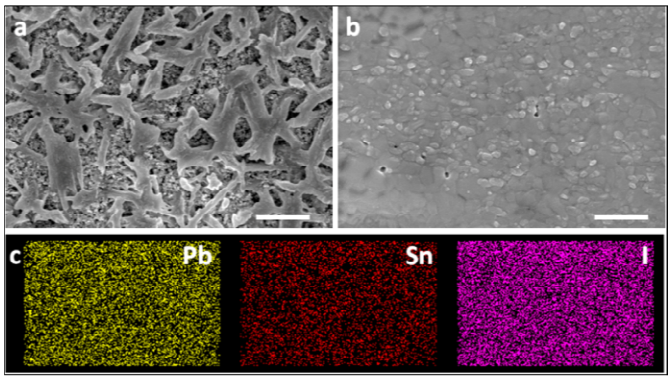

Fig. 23 Representative SEM images of the (a) $CH_3NH_3PbI_3$ and (b) $CH_3NH_3Sn_{0.5}Pb_{0.5}I_3$ films on top of the mesoporous TiO_2 electrodes. The scale bars represent 1 μm. (c) EDS elemental mapping of Pb, Sn and I in film (b). Reproduced with permission from ref. 136. Copyright 2014, American Chemical Society.

Very recently, Noel et al. employed a completely lead-free perovskite, $CH_3NH_3SnI_3$, for perovskite-based solar cells.[137] A PCE of greater than 6% was achieved under simulated full sunlight with a V_{oc} of 0.88 V and a BG of 1.23 eV. However, the stability of $CH_3NH_3SnI_3$ remains a challenge, and the main issue is now the stabilization of the material then the oxidation of the Sn is suppressed. By solving this issue, it can be expected that the performance of Sn perovskites will surpass those of the state-of-the-art Pb-based perovskites over the next few years, with a distinct toxicology advantage. Importantly, this finding demonstrates that Pb-based materials are not unique in delivering efficient perovskite solar cells.

4.2.2.3 Selection and doping of A-site elements

It was reported that in the $CH_3NH_3PbI_3$ system, the A cation did not play a major role in determining the band structure but acted to ensure charge compensation within the lattice. Nevertheless, the A cation could affect the optical properties by deforming the BX_6^{4-} octahedron network due to the variation of its size. A larger or smaller A cation can cause the entire lattice to expand or contract and lead to a change of the B–X bond length, which has been demonstrated to be important in determining E_{bg}. Based on the tolerance factor (t) calculation in the perovskite $APbI_3$ structure, A site cation radii range from 164 pm to 259 pm, corresponding to the t values ranging from 0.8 to 1.0, respectively, assuming Pb^{2+} = 119 pm and I^- = 220 pm. The $CH_3NH_3^+$ cation is suitable for the perovskite structure because of its suitable ionic radius of 180 pm. A reduced BG of the perovskite was obtained by replacing the MA component with a slightly larger cation, FA.[113,138-140] As shown in Fig. 24a, perovskites are defined as any compound that crystallizes in the ABX_3 structure, consisting of corner-sharing BX_6 octahedra with the A component neutralizing the total charge.[113] As demonstrated in Fig. 24b, cesium has a smaller effective ionic radius than MA, whereas that of FA is slightly larger. Fig. 24c presents the absorbance spectra of these materials; $CsPbI_3$ is observed to absorb to a shorter wavelength than $MAPbI_3$, whereas $FAPbI_3$ absorbs to a longer wavelength than $MAPbI_3$. It is suggested that as the A cation increases in ionic radius, the lattice expands while BG decreases, causing a red-shift in the absorption spectra. Therefore, $FAPbI_3$ is a potential candidate to produce even more efficient solar cells than $CH_3NH_3PbI_3$ ($MAPbI_3$). Very high currents could be generated under simulated sunlight, and specifically, high short-circuit currents of > 23 mA cm^{-2} and a PCE as high as 14.2% were achieved. $FAPbI_3$, as a new candidate for this class of solar cell, thus requires further attention.

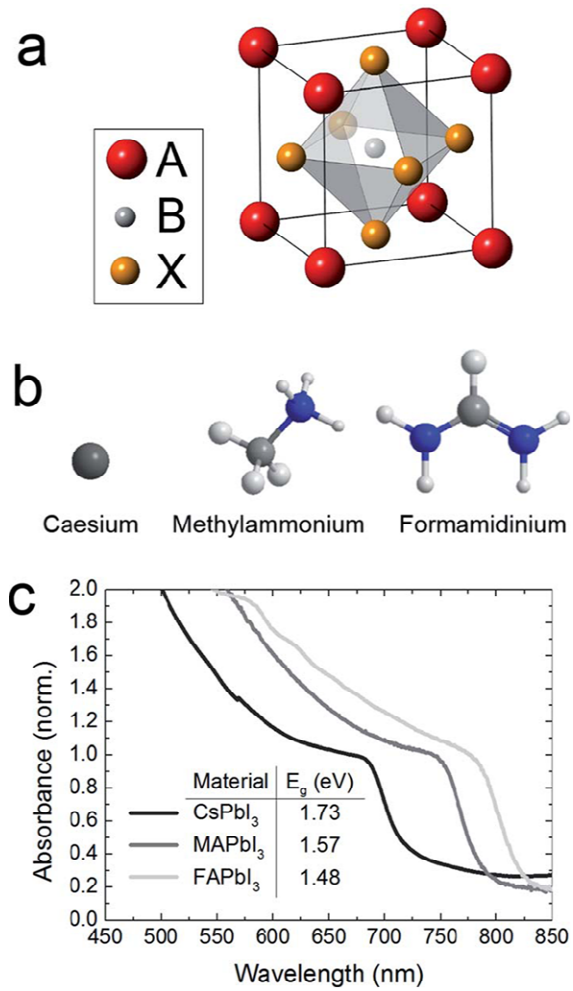

Fig. 24 Tuning perovskite BG by replacing the A cation. (a) The ABX_3 perovskite crystal structure. (b) The atomic structure of the three A site cations explored. (c) UV-Vis spectra for the $APbI_3$ perovskites formed, where A is either caesium (Cs), methylammonium (MA) or formamidinium (FA). Reproduced with permission from ref. 113. Copyright 2014, Royal Society of Chemistry.

Lee et al. observed that weak absorption at long wavelength was observed with $FAPbI_3$ perovskite, which could be overcome by the introduction of an extremely thin $CH_3NH_3PbI_3$ layer on top of the $FAPbI_3$ layer.[140] Consequently, an average PCE of 15.56% was achieved by a $FAPbI_3$ layer with a thin $CH_3NH_3PbI_3$ overlayer. The best PCE of 16.01% was obtained from this developed structure, suggesting that $FAPbI_3$ is a promising candidate for high-efficiency perovskite solar cells. However, some researchers focused on the replacement of MA in the A site as well as X-site doping of $CH_3NH_3PbI_3$, and some excellent results based on $FAPbBr_3$ and $FAPbI_{3-x}Cl_x$ were obtained.[141,142] For example, Hanusch et al. demonstrated a highly efficient $FAPbBr_3$ perovskite for solar cells.[141] This material exhibited much longer diffusion lengths of the photoexcited species than $CH_3NH_3PbI_3$. A PCE of 6.6% was obtained with $FAPbBr_3$ perovskite, which was more than 10 times higher than that of $CH_3NH_3PbI_3$ under the same conditions. Hence, $FAPbBr_3$ is a strong candidate as a wide BG absorber in perovskite solar cells.

Pellet et al. have demonstrated a perovskite with mixed A-site cations $(CH_3NH_3)_x(FA)_{1-x}PbI_3$ (x=0-1) for further improvement of the performance of perovskite-based photovoltaics.[143] Devices based on $FAPbI_3$ perovskite produced a PCE of 11.0% (a lower value than that of $CH_3NH_3PbI_3$ because of the presence of the yellow d-phase). The addition of 20% CH_3NH_3 to the FA completely avoided the undesirable formation of the d-phase while maintaining the red-shifted BG of $FAPbI_3$. This combination leads to an enhanced short-circuit current and thus superior devices to those based on only CH_3NH_3, and a PCE of 14.9% was obtained. The strategy of mixing organic ammonium compounds opens up new prospects for the further improvement of the photovoltaic efficiency of perovskite-sensitized solar cells by tuning the optical, electrical, and morphological properties of the semiconducting sensitizer. It was believed that the performance of pure $FAPbI_3$ would most likely surpass that of $CH_3NH_3PbI_3$-based mesoscopic solar devices if the formation of the yellow d-$FAPbI_3$ component could be fully avoided. Similarly, $FAPbI_3$ was successfully introduced into hole-conductor-free fully printable mesoscopic perovskite solar cells with a carbon counter electrode. Using the sequential deposition method, the $FAPbI_3$-based solar cell yielded an efficiency of 11.9%, which is superior to that of the $MAPbI_3$ solar cell of 11.4% due to broadening the light to 840 nm. By optimizing the FA and MA cation mixing ratio to 3:2, a PCE of 12.9% was achieved with this low-cost fully printable mesoscopic solar cell, which indicated a promising prospect for low-cost photovoltaic technology. Choi et al. demonstrated cesium-doping in methylammonium lead iodide perovskite ($Cs_xMA_{1-x}PbI_3$) light absorbers to improve the performance of perovskite-based solar cells. The $Cs_xMA_{1-x}PbI_3$ perovskite devices with an optimized 10 mol.% Cs doping concentration exhibited remarkable improvement in device efficiency from 5.51 to 7.68% due to increases in J_{sc} and V_{oc}.[144] This improvement should be attributed to the increased light absorption capability, improved film morphology and almost unchanged E_{bg}. The optical BG of $Cs_xMA_{1-x}PbI_3$ perovskite gradually increased from 1.52 eV for pure $MAPbI_3$ to 2.05 eV for pure $CsPbI_3$ with increasing Cs content, which implies that the optical BG can be easily tuned by controlling the amount of Cs in $Cs_xMA_{1-x}PbI_3$ perovskites.

4.2.3 Increase of the diffusion length of the electron-hole pair

It is well known that the recombination lifetime of the electron-hole pair is a crucial factor that contributes to the charge diffusion length of light-absorbing materials and hence affects their photovoltaic performance. In other words, longer charge diffusion lengths are associated with longer recombination lifetimes of electron-hole pairs, which is beneficial for improving the performance of perovskite light-absorber-based solar cells. For instance, for $CH_3NH_3PbI_3$ and $CH_3NH_3PbI_{3-x}Cl_x$, both perovskites have a similar light absorption range, whereas $CH_3NH_3PbI_{3-x}Cl_x$ has a longer recombination lifetime than $CH_3NH_3PbI_3$, followed by a longer diffusion length. The relatively large charge carrier diffusion lengths arise from the higher mobility and larger charge carrier lifetimes in these

 This journal is © The Royal Society of Chemistry 2012

materials. Therefore, light-generated electrons and holes can move ultra-long distances in the perovskite, resulting in the generation of photocurrent, instead of losing their energy as heat within solar cells. In addition, $CH_3NH_3PbI_{3-x}Cl_x$ does not require a mesoporous electron transport layer (e.g., TiO_2), unlike $CH_3NH_3PbI_3$. The long electron diffusion length enables $CH_3NH_3PbI_{3-x}Cl_x$ to work perfectly on insulating scaffolds and even in bulk films. A longer electron diffusion length facilitates a larger optimized thickness of the light-absorbing layer, where charge carriers can be extracted in a timely manner before the recombination. A thicker light-absorbing layer will eventually contribute to a more effective light utilization by employing more absorbers.

Specifically, Stranks et al. used transient absorption and photoluminescence-quenching measurements to determine the electron-hole diffusion lengths, diffusion constants, and lifetimes in $CH_3NH_3PbI_{3-x}Cl_x$ and $CH_3NH_3PbI_3$ perovskite absorbers.[84] It was observed that the diffusion length was larger than 1 μm in the $CH_3NH_3PbI_{3-x}Cl_x$ perovskite, which is an order of magnitude greater than the absorption depth. In contrast, the $CH_3NH_3PbI_3$ absorber had smaller electron-hole diffusion lengths of ~100 nm. Similarly, Xing et al.[83] also reported that the electron-hole diffusion lengths of $CH_3NH_3PbI_3$ absorber were approximately 100 nm by applying femtosecond transient optical spectroscopy to bilayers that interface this perovskite with either selective-electron or selective-hole extraction materials.

Recently, Wehrenfennig et al. investigated the charge carrier dynamics in vapor-deposited $CH_3NH_3PbI_{3-x}Cl_x$ using ultrafast THz spectroscopy, revealing the carrier mobility and recombination rates.[145] Under typical solar-cell operation conditions, the charge carrier lifetimes were limited by only mono-molecular decay processes, such as trap-mediated recombination, which have previously been observed to be exceptionally slow. The resulting charge diffusion length was observed to be 3 μm, highlighting the capability of dual-source evaporation as a fabrication route for organolead halide absorber layers in highly efficient planar-heterojunction solar cells.

Because of their longer diffusion lengths of electron-hole pairs, $CH_3NH_3PbI_{3-x}Cl_x$ series have recently attracted increasing attention.[146-150] Ma et al. synthesized $CH_3NH_3PbI_{3-x}Cl_x$ via a two-step sequential solution deposition process using a mixture of $PbCl_2$ and PbI_2 as the precursor to overcome the low solubility of pure $PbCl_2$ with easy morphology control and an achieved PCE of 11.7%.[146] Even though excellent photovoltaic performances have been achieved using $CH_3NH_3PbI_{3-x}Cl_x$, the formation of this mixed halide perovskite and the role of the chloride remains poorly investigated. Colella et al. studied the role of the chloride dopant on the transport and structural properties of $CH_3NH_3PbI_{3-x}Cl_x$ light absorbers.[147] These authors observed that independent of the ratio of components in the precursor solution, Cl incorporation in an iodide-based structure is possible only at relatively low concentration levels (below 3-4%). PCE increased from 3.85 to 6.15% with the doping of Cl. The strong difference in the halogen ionic radii interferes with the formation of a continuous solid solution. However, even if the BG of the material remains substantially unchanged, the Cl doping dramatically improves the charge transport within the perovskite layer, explaining the outstanding performance improvement of this material.

It was observed that the doping amount of Cl in $CH_3NH_3PbBr_3$ was much larger than that in $CH_3NH_3PbI_3$, which led to increased recombination lifetimes of electron-hole pairs. Zhang et al. observed that the mixed halide perovskites $CH_3NH_3PbBr_{3-x}Cl_x$ (x = 0.6-1.2) exhibited different optical properties.[151] In particular, the thin films prepared with these perovskites exhibited extraordinary photoluminescence emission intensities and prolonged recombination lifetimes, which are desirable for light-emitting and photovoltaic applications. The recombination lifetime of $CH_3NH_3PbBr_{3-x}Cl_x$ was determined by measuring the photoluminescence decay at the emission peak wavelengths. The time-resolved photoluminescence decay curves of $CH_3NH_3PbBr_{3-x}Cl_x$ with different Cl substitution ratios are presented in Fig. 25. $CH_3NH_3PbBr_{3-x}Cl_x$ exhibits a longer average recombination lifetime than $CH_3NH_3PbBr_3$. Especially for $CH_3NH_3PbBr_{2.4}Cl_{0.6}$, the average recombination lifetime can be extended up to 446 ns compared with 100 ns and 44 ns for $CH_3NH_3PbBr_3$ and $CH_3NH_3PbI_{3-x}Cl_x$, respectively. However, the corresponding average recombination lifetime of the $CH_3NH_3PbBr_{3-x}Cl_x$ perovskite decreased with a larger Cl substitution ratio for I.

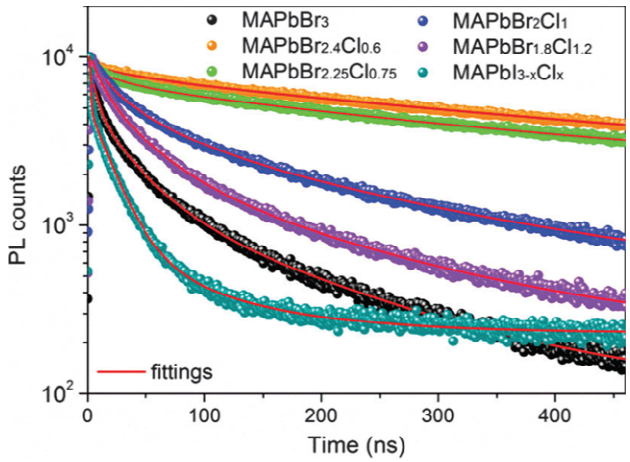

Fig. 25 Time-resolved photoluminescence decay detected at the peak wavelength of emission for various $CH_3NH_3PbX_3$ (X = Cl, Br, I) perovskites. Reproduced with permission from ref. 151. Copyright 2014, Royal Society of Chemistry.

In addition to the selection of the X-site element in the $CH_3NH_3PbX_3$ perovskite, the selection of the A-site element also had a strong effect on the recombination lifetimes and diffusion lengths of the electron-hole pairs. Hanusch et al. studied the recombination lifetimes of the electron-hole pairs of the $FAPbBr_3$ perovskite compared with those of $CH_3NH_3PbBr_3$.[141] The $FAPbBr_3$ films exhibited an unusually long decay lifetime of approximately 200 ns, much slower than the lifetime exhibited by $CH_3NH_3PbBr_3$ films (17 ns). Stranks

et al. attributed a comparable lifetime of approximately 200 ns for the $CH_3NH_3PbI_{3-x}Cl_x$ perovskite to a diffusion length of electrons and holes of more than 1 μm. In contrast, the $CH_3NH_3PbBr_3$ variant exhibited a similar lifetime to that of the non-Cl treated $CH_3NH_3PbI_3$ perovskite and therefore diffusion lengths closer to 100 nm. A high PCE of 7% was successfully obtained by $FAPbBr_3$ in a planar heterojunction architecture without the need for a mesoporous scaffold. The devices fabricated from $CH_3NH_3PbBr_3$ in the same configuration were observed to be charge collection limited, whereas the formamidinium variant exhibited diffusion lengths that were orders of magnitude longer and therefore was able to achieve a high charge collection efficiency.

4.2.4 Crystallinity and Morphology Control

The photovoltaic performance of the $CH_3NH_3PbI_3$ perovskite-based solar cells is greatly dependent on the crystallinity and film morphology, which is determined by the deposition techniques and subsequent treatments. To improve the performance of the thin-film perovskite-based solar cells, precise control of the surface structures is required, and several advanced preparation methods, such as spin coating, spray deposition, vapor-assisted solution process and surface passivation, have been developed recently.[121,152-156]

4.2.4.1 Spin coating method

The solution processability of the organic-inorganic perovskite material is one of its major advantages, and the simplest method of deposition requires only a simple heating step to convert the deposited precursor solution (consisting of the organic and inorganic components) into the crystalline perovskite film. Spin coating was used by Burschka et al.[85] to prepare the $CH_3NH_3PbI_3$ perovskite, and some parameters such as the temperature used in the annealing process, were carefully investigated by Dualeh et al.[122] In addition, to avoid PbI_2 crystals protruding from the surface of the substrate for a complete and fast conversion from PbI_2 to $CH_3NH_3PbI_3$, the spin-coating step of PbI_2 usually uses high spin speed or low concentration PbI_2 solution.[119,156] However, reliable deposition of high-quality films of phase-pure $CH_3NH_3PbI_3$ perovskites with full coverage and high crystallinity still remains a challenge. In addition, films produced by the conventional spin-coating methods were observed to be composed of large $CH_3NH_3PbI_3$ grains and many uncovered pin-hole areas.[123,124] This structure can be attributed to the slow crystallization because of the high boiling point of N,N-dimethylformamide (DMF, 153 °C) and crystal growth arising from a slow nucleation rate during the natural drying process in spin-coating. Therefore, tremendous efforts have been devoted to the modification of the spin coating process to improve the film morphology and achieve high crystallinity of the perovskite.[123,124,157] Some additives are added to the preparation process of the perovskite such as NH_4Cl, 1,8-diiodooctane (DIO), etc. [123,124] Zuo and Ding demonstrated that the NH_4Cl additive can improve the crystallinity and film morphology of the $CH_3NH_3PbI_3$ light-absorbing perovskite layer.[123] In comparison, another chloride additive of CH_3NH_3Cl was also examined for the aspects of perovskite film properties and photovoltaic performance. The X-ray diffraction (XRD) results suggested that the additives favored $CH_3NH_3PbI_3$ crystallization and that NH_4Cl was more effective than CH_3NH_3Cl. The morphology of the $CH_3NH_3PbI_3$ films prepared using different additives was investigated using SEM and atomic force microscopy (AFM).

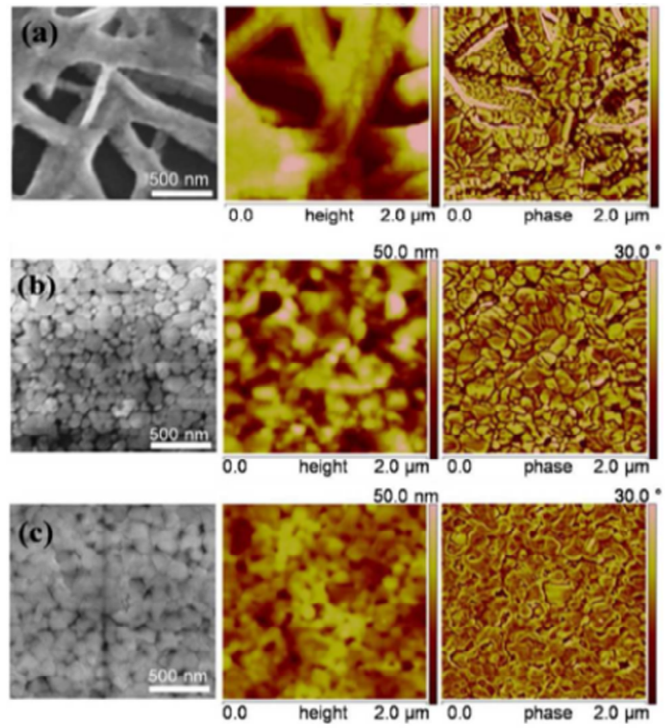

Fig. 26 SEM (left), AFM height (middle) and phase (right) images for $CH_3NH_3PbI_3$ films fabricated using no additive (a), 17.5 mg/mL CH_3NH_3Cl (b), 17.5 mg/mL NH_4Cl (c), respectively. Reproduced with permission from ref. 123. Copyright 2014, Royal Society of Chemistry.

Fig. 26 presents SEM and AFM images of $CH_3NH_3PbI_3$ films prepared using different additives.[123] The film prepared using no additives exhibited large voids and an extremely rough surface. (Fig. 26a) Nearly no voids were observed in the film prepared using the CH_3NH_3Cl additive, and pebble-like nanocrystals (70-200 nm) are distributed in the film. (Fig. 26b) The film prepared using the NH_4Cl additive contained uniform nanocrystals (Fig. 26c) and exhibited better coverage than the film prepared using the CH_3NH_3Cl additive. The film prepared using no additive exhibited a root-mean-square (RMS) roughness of 47.5 nm. The films prepared using the CH_3NH_3Cl and NH_4Cl additives were much smoother with RMS roughnesses of 15.3 nm and 5.2 nm, respectively. The improved crystallinity and morphology of the perovskite films fabricated using the NH_4Cl additive led to a remarkable enhancement in the device performance (a PCE of 9.93% and a FF of 0.8011). This work provided a very simple but effective approach to enhance the PCE of perovskite solar cells. Liang et al. reported a significantly enhanced PCE of the planar-heterojunction perovskite solar cells from 9.0% up to 11.8% by incorporating a small amount of DIO additives into the perovskite precursor solutions to improve the crystallization of

 This journal is © The Royal Society of Chemistry 2012

the perovskite thin films. It was observed that the incorporated additives facilitate homogenous nucleation and modulate the kinetics of growth during crystallization, as evidenced from the surface SEM images and XRD spectra. The enhanced crystallization facilitates the charge transfer efficiency between the charge transporting interlayers and the perovskite absorber.

To overcome the problem of incomplete conversion and uncontrolled particle sizes of perovskite on the mesoporous scaffolds, Wu et al. optimized the sequential deposition of $CH_3NH_3PbI_3$ perovskite by retarding the crystallization of PbI_2 by changing the solvent in the spin-coating process.[157] The use of strong coordinative dimethylsulfoxide (DMSO) instead of DMF as the solvent for PbI_2 resulted in extremely uniform and amorphous featured PbI_2 films, which were fully converted into $CH_3NH_3PbI_3$ perovskite crystals within 10 min. The resultant perovskite films consisted of a small distribution of crystal sizes and exhibited a flat surface morphology. The highly reproducible perovskite films enabled reproducible planar-structured perovskite solar cells with a PCE of 13.5% to be prepared. The reproducible high performance devices provided a platform for in-depth device studies and the further optimization of photovoltaic performances. Moreover, the strategy of retarding the crystallization of precursor films is worth further study and can be applied to fabricating new perovskites as well as other planar substrates. In addition, some researchers have systematically studied the effect of the CH_3NH_3I/PbI_2 precursor ratio on the perovskite film morphology and device performance.[153,158] A non-stoichiometric precursor solution was demonstrated to be critical to form stoichiometric perovskite films. The compositions of the perovskite films were very sensitive to the surface of the substrates and could be very different from that in precursor solutions.[153]

4.2.4.2 New and advanced technologies for the preparation of the perovskite layer

Unfortunately, there are several drawbacks in the spin-coating process for the preparation of $CH_3NH_3PbI_3$ perovskite. It was observed that for the organic part, longer organic chains made it more difficult to find a good solvent. For the inorganic part, solvent techniques always encounter some problems related to the solubility, strong solvent coordination or stability of the metal valence state. Vacuum evaporation is one of the most promising techniques to construct $CH_3NH_3PbI_3$ perovskite thin films with a precise control of the film property.[118] The resulting perovskites prepared by co-evaporation of two precursors ($PbCl_2$ and CH_3NH_3I) exhibited satisfactory film coverage and uniformity.[55,118] However, this technique demands high vacuum, which is too energy intensive and not suitable for mass production. In addition, the preparation of various perovskites using different organic components is expected to be limited in the vacuum evaporation process, and deposition without vacuum evaporation might be advantageous for low-cost solar cells. A low-temperature vapor-assisted solution process (VASP) based on the kinetically favorable reaction between the as-deposited film of PbI_2 and CH_3NH_3I vapor was demonstrated to produce polycrystalline perovskite thin films with full surface coverage, small surface roughness and grain sizes up to the microscale as well as 100% precursor transformation completeness.[120] The film was prepared via an in situ reaction of the as-deposited film of PbI_2 with CH_3NH_3I vapor (Fig. 27).[120] This method is conceptually different from the current solution process and vacuum deposition by avoiding the co-deposition of organic and inorganic species. The solar cells with the as-prepared films achieve a high PCE of 12.1% based on $CH_3NH_3PbI_3$ with the planar heterojunction configuration. The VASP method provides a simple, controllable and versatile approach to obtain high-quality perovskite films for solar cells and some other organic/inorganic hybrid optoelectronics. The charge transport behavior of the as-prepared films requires further study. Similarly, Lewis and Paul O'Brien have used aerosol-assisted chemical vapor deposition (AACVD) to produce $CH_3NH_3PbBr_3$ perovskite films on glass substrates.[154] The films produced using this method are comparable in quality to those prepared using the current methods for the deposition of the inorganic–organic perovskites such as spin coating.

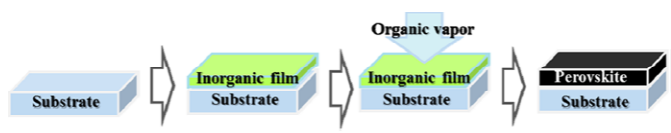

Fig. 27 Schematic illustration of perovskite film formation through vapor-assisted solution process. Reproduced with permission from ref. 120. Copyright 2014, American Chemical Society.

Combining the advantages of the spin-coating and vacuum-evaporation processes described above, Liang et al. created a two-step deposition (TSD) technique to prepare hybrid perovskites.[159] First, a layer of metal halide, MI_2 (M = IVB group metal), was deposited using vacuum evaporation or spin coating, followed by dipping the film into an organic salt solution. Bi et al. have used this TSD technique for preparing $CH_3NH_3PbI_3$ perovskite solar cells.[156] Considering the low-cost advantages associated with a non-vacuum preparation technique, spin coating is used for the first step. PCEs of 10.8 and 9.5% were obtained with ZrO_2 and TiO_2 under AM 1.5G illumination, respectively. Comparing TSD and the one-step spin-coating method in a TiO_2 solar cell, it is demonstrated that J_{sc} can be higher because of the greater amount of perovskite that can be deposited by the TSD method due to the better solubility. These results suggest that TSD is expected to be particularly useful for preparing films of organic-inorganic systems in which the organic and inorganic components have incompatible solubility characteristics or for systems in which the organic component is difficult to evaporate.[156] Shi et al. further modified the TSD process by adding the times of spin-coated PbI_2 to achieve $CH_3NH_3PbI_3$ perovskite thin film with high uniformity and coverage.[160] Incomplete coverage on the TiO_2 film with $CH_3NH_3PbI_3$ crystals was observed by spin-coating the PbI_2 solution for the first time, which is mainly attributed to the relatively rough surface of the prepared PbI_2 films. However, by spin-coating the PbI_2 solution for a second

time, the morphology of the PbI_2 film on TiO_2 was clearly ameliorated and complete coverage of $CH_3NH_3PbI_3$ on the TiO_2 film was observed. This study provides a useful method for the further development of perovskite-based solar cells. In addition, a mixed halide perovskite of $CH_3NH_3PbI_{3-x}Cl_x$ was recently synthesized by Ma et al. via two-step sequential solution deposition.[146] A mixture of PbI_2 and $PbCl_2$ was used rather than pure $PbCl_2$ as the precursor to ensure high loading in the mesoporous TiO_2 film, with easy morphology control, which results in a great enhancement of the light absorbance for the device and suppression of the electron-hole recombination by separating the bare TiO_2 and HTM layer. A PCE of 11.7% was achieved for the mesoscopic cell, which is much higher than that for the cell constructed via a spin-coating process.

As mentioned above, the PCEs have been improved to 15% using a two-step sequential deposition technique, involving spin-coating of PbI_2 followed by exposure to a solution of CH_3NH_3I to form $CH_3NH_3PbI_3$ or a dual-source vapor deposition technique to fabricate a planar heterojunction solar cell. To date, the $CH_3NH_3PbI_3$ layer in the most efficient planar solar cells has been fabricated by vapor deposition, a two-step sequential solution deposition, or a vapor-assisted two-step reaction process.[55,119,120] The vapor deposition process could increase the manufacturing cost, whereas the sequential two-step deposition procedure involves a longer overall processing time. Therefore, a faster, facile solution-processing technique that can regulate the perovskite crystallization process and produce high-quality films with controlled morphology is highly desirable for the construction of planar devices with superior performances. Xiao et al. reported a one-step, solvent-induced, fast deposition crystallization (FDC) method involving spin-coating of a DMF solution of $CH_3NH_3PbI_3$ followed immediately by exposure to chlorobenzene (CBZ) to induce crystallization to obtain flat, uniform $CH_3NH_3PbI_3$ thin films.[125] This simple approach involves the spin coating of a DMF solution of $CH_3NH_3PbI_3$ on a substrate, followed immediately by exposure of the wet film to a second solvent, such as CBZ, to induce crystallization. This FDC spin-coating method offers the advantage of single-step processing and short deposition times as the film formation is complete within 1 min. The FDC method for preparing the $CH_3NH_3PbI_3$ films is shown in Fig. 28.[125] First, a dense TiO_2 layer was deposited on a fluorine-doped tin oxide (FTO) coated glass using spray pyrolysis. A DMF solution of $CH_3NH_3PbI_3$ (45 wt.%) was then spin-coated on the TiO_2 layer. After a specific delay time (e.g., 6 s), a second solvent was quickly added to the substrate. The role of the second solvent was to rapidly reduce the solubility of $CH_3NH_3PbI_3$ in the mixed solvent and thereby promote fast nucleation and growth of the crystals in the film. An instant darkening of the film when the second solvent was added was taken as evidence of the formation of the desired material. In contrast, during the conventional spin-coating process, where no second solvent was added, the wet film dried slowly and a shiny-gray film was obtained. The films were then subjected to annealing at 100 °C for 10 min to evaporate any residual solvent and to further promote crystallization. Planar heterojunction solar cells constructed with these solution-processed thin films yielded an average PCE of 13.9% under standard AM 1.5 conditions.

Despite tremendous efforts in film-formation processes, useful guidelines for processing perovskite films remain less explored. Some researchers aim to exploit the surface/interfaces and grain boundaries (GBs) in the perovskite films that affect the carrier behavior within the relevant heterojunction. Accordingly, a technique will ultimately be developed to achieve delicate control over the film property that promotes the charge generation, transportation, and collection in the solar cell. A controllable passivation technique has been used for the preparation of perovskite films, which enables their compositional change and allows substantial enhancement in corresponding device performance.[121] It was observed that the presence of PbI_2 species in the GBs upon thermal annealing leads to a successful passivation that controls the carrier behavior along the heterojunctions. An appropriate amount of the PbI_2 species in the $CH_3NH_3PbI_3$ film led to improved carrier behavior, possibly due to reduced recombination in the GBs and the TiO_2/perovskite surface. Additionally, the GB property of the perovskite film behaved differently after the passivation. This controllable self-induced passivation technique represents an important step to understanding the polycrystalline nature of hybrid perovskite thin films and judiciously contributes to the development of perovskite solar cells. Future work focused on the nature of the GBs of perovskite materials to design a rational approach to passivate the film is needed. Very recently, Noel et al. demonstrated that treatment of organic-inorganic metal halide perovskite films with the Lewis bases thiophene and pyridine resulted in a significant decrease in the rate of non-radiative recombination in perovskite films.[161] These results are due to the electronic passivation of under-coordinated Pb atoms within the crystal. The Lewis base molecules bind to the under-coordinated Pb ions in the perovskite crystal, thus passivating these defect sites. Using this method of Lewis base passivation, the PCEs for solution-processed planar heterojunction solar cells were enhanced from 13% to 15.3% and 16.5% for the untreated, thiophene-treated and pyridine-treated solar cells, respectively.

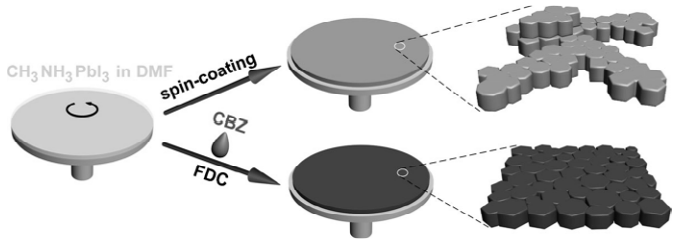

Fig. 28 Schematic illustration of the FDC process and conventional spin-coating process for fabricating perovskite films. Conventional spin-coating (top) results in a shiny gray film composed of non-uniform large crystals as a result of slow crystallization. In the FDC process (bottom), a second solvent (e.g. CBZ) introduced on top of the wet film during the spin-coating process induces fast crystallization of uniformly sized perovskite grains. Reproduced with permission from ref. 125. Copyright 2014, Wiley-VCH Verlag GmbH & Co. KGaA, Weinheim.

This journal is © The Royal Society of Chemistry 2012

4.2.5 Other issues concerning CH3NH3PbI3-based perovskite solar cells

4.2.5.1 Development of active hole-transporting materials to suppress electron-hole pair recombination

Perovskite solar cells generally consist of a conductive substrate, a compact TiO_2 layer, an organohalide lead perovskite light-absorption layer (single or combined with a porous scaffold), a hole-transporting material (HTM), and a metal cathode (Ag or Au). Studies have mainly focused on designing scaffold layers, optimizing the perovskite layer and exploring alternative structures. As one of the key components in perovskite solar cells, the HTM separates photo-excited electron-hole pairs and transports the holes to the external circuit. Recently, researchers have focused on the development of a HTM suitable for organohalide lead perovskites to achieve high performance. Appropriate HTMs for perovskite solar cells should primarily meet the following requirements: good hole mobility, a compatible HOMO (Highest Occupied Molecular Orbital) energy level relative to the perovskites and low cost for commercialization. Fluorine-doped $CsSnI_3$ was adopted by Kanatzidis and co-workers in 2012 as a p-type solid HTM in DSSCs with N719 (bis(tetrabutylammonium)[cis-di(thiocyanato)-bis(2,2'-bipyridyl-4-carboxylate-4'-carboxylic acid)-ruthenium (II)]) as the absorber.[133] This study was the first time that a perovskite material was used as the HTM in a solid-state DSSC with efficiencies reaching 10.2%, which revived the concept of all-solid-state inorganic solar cells and demonstrated that perovskite materials could be good HTM candidates.[133] The next breakthrough occurred in late 2012, when M. Grätzel and co-workers teamed with N. G. Park, who used $CH_3NH_3PbI_3$ as a light harvester in combination with the solid HTM spiro-MeOTAD on mesoporous TiO_2, leading to a PCE of 9.7%.[50] Spiro-MeOTAD was demonstrated to be an effective HTM for perovskite-based solar cells. For example, Bi et al. have studied the effect of HTMs on the performance of $CH_3NH_3PbI_3$-based solar cells, and the various HTMs include spiro-MeOTAD, poly(3-hexylthiophene-2,5-diyl) (P3HT) and 4-(diethylamino)-benzaldehyde diphenylhydrazone (DEH).[162] The PCEs are 8.5, 4.5 and 1.6% under AM 1.5G illumination for the spiro-MeOTAD, P3HT and DEH, respectively. Electron lifetime measurements revealed that the recombination of the separated charges in the device using spiro-MeOTAD as the HTM was more than 10 times slower than that in the device with P3HT and more than 100 times slower than that in the device with DEH. These results suggested that the nature of the HTM is essential for charge recombination and suggests that finding an optimal HTM for the perovskite solar cell includes controlling the perovskite/HTM interaction. However, spiro-MeOTAD alone in HTM is insufficient for obtaining high PCEs because of low conductivity and other problems. Adding different types of functional additives to spiro-MeOTAD can further improve the properties of HTM and ensure high-efficiency perovskite solar cells.[163-165] Zhang et al. used a stable ionic liquid N-butyl-N'-(4-pyridylheptyl) imidazolium bis(trifluoromethane) sulfonimide (BuPyIm-TFSI) as a dual-functional additive to simultaneously improve the electrical property of spiro-MeOTAD and suppress charge combination in perovskite solar cells.[163] The PCE greatly increased from 3.83% to 7.91% with this additive, which is comparable to that of the conventional spiro-MeOTAD containing lithium salt and 4-tert-butylpyridine (TBP). Moreover, using such a dual-functional additive can effectively simplify the components of the HTM and help reduce the production costs.

The highest costs of materials in perovskite-based solar cells come from spiro-MeOTAD, which is very expensive because of its multistep synthesis process. The current commercial price of high purity spiro-MeOTAD is more than ten times that of gold and platinum precious metals. Therefore, it is imperative, from a commercialization viewpoint, to develop efficient and cost-effective HTMs. Some new organic HTMs based on triptycene core, 3,4-ethylenedioxythiophene, quinolizino acridine, polythiophene and tetrathiafulvalene derivatives have recently been developed with high PCEs.[166-171] For example, Li et al. reported an electron-rich molecule based on 3,4-ethylenedioxythiophene (H101).[167] When H101 was used as the HTM in a perovskite-based solar cell, the PCE reached 13.8% under AM 1.5G solar simulation. This result is comparable with that obtained using the well-known HTM spiro-MeOTAD, further suggesting great potential to replace the expensive spiro-MeOTAD given its much simpler and less expensive synthesis. Despite the high cost, the most investigated wide-gap spiro-MeOTAD almost exhibited no absorption in the visible and near-IR region of the solar spectrum. In this respect, low BG donor-acceptor (D-A) polymers with strong absorptions in this spectral region should be designed for the HTM in perovskite-based solar cells. Low BG oligothiophenes incorporating *S*, *N*-heteropentacene central units were developed by Qin et al.[172] and used as an HTM in solid-state perovskite-based solar cells. In addition to appropriate electronic energy levels, these materials exhibit high photo absorptivity in the low energy region and could thus contribute to the light harvesting of the solar spectrum, which opens up a new avenue for the fabrication and material selection of perovskite-based devices. Solution-processed $CH_3NH_3PbI_3$-based devices using this HTM achieved PCEs of 9.5-10.5%.

Table 3 Photovoltaic performance of the selected perovskite light absorbers-based solar cells.

No.	Light absorber*	HTM	Preparation method and/or treatment	BG (eV)*	PCE (%)	V_{oc} (V)	FF	Ref.
1	$CH_3NH_3PbI_3$	spiro-MeOTAD	Spin coatig	1.5	9	0.888	0.62	50
2	$CH_3NH_3PbI_2Cl$	spiro-MeOTAD	Spin coatig	1.55	10.9	1.1	0.63	51
3	$CH_3NH_3PbI_{3-x}Cl_x$	spiro-MeOTAD	Spin coatig	/	12.3	1.02	0.67	54
4	$CH_3NH_3PbI_{3-x}Cl_x$	spiro-MeOTAD	Solution-processed	/	8.6	0.84	0.58	55
5	$CH_3NH_3PbI_{3-x}Cl_x$		Vapour-deposited	/	15.4	1.07	0.67	
6	$CH_3NH_3PbI_{3-x}Cl_x$	spiro-MeOTAD	Spin coatig	/	11.4	0.89	0.64	56
7	$MAPbI_3$			1.56	10.64	0.977	0.6113	
8	$MAPb(I_{0.88}Br_{0.12})_3$	/	Spin coatig	1.62	8.13	0.890	0.6531	110
9	$MAPb(I_{0.05}Br_{0.95})_3$			2.23	1.03	0.832	0.4981	
10	$CH_3NH_3PbBr_3$	/	Spin coatig	2.17	3.13	0.96	0.59	111
11	$CH_3NH_3PbI_3$			1.55	3.81	0.61	0.57	
12	$(CH_3CH_2NH_3)PbI_3$	/	Spin coatig	~2.2	2.4	0.66	0.704	112
13	$FAPbI_3$			1.48	14.2	0.94	0.65	
14	$FAPbBr_3$	spiro-MeOTAD	Spin coatig	2.23	1.9	1.02	0.65	113
15	$FAPbI_{0.8}Br_{2.2}$			~1.6	9.1	1.00	0.67	
16	$CH_3NH_3Sn_{0.5}Pb_{0.5}I_3$	P3HT	Spin coatig	1.17	4.18	0.42	0.5	116
17	$CH_3NH_3PbI_3$			1.55	0.18	0.23	0.29	
18	$CH_3NH_3PbI_{3-x}Cl_x$	spiro-MeOTAD	Spin coatig	/	12.2	0.97	0.45	118
19	$CH_3NH_3PbI_3$				4.2	0.71	0.7	
20	$CH_3NH_3PbI_3$	spiro-MeOTAD	Spin coatig	1.55	15.0	0.993	0.73	119
21	$CH_3NH_3PbI_3$	spiro-MeOTAD	Vapor-assisted solution process	1.55	12.1	0.94	0.682	120
22	$CH_3NH_3PbI_3$	spiro-MeOTAD	Self-induced passivation	1.5	12	0.959	0.6932	121
23	$CH_3NH_3PbI_3$	spiro-MeOTAD	Spin coatig annealing at 60 ºC	1.5	1.78	0.799	0.68	122
24	$CH_3NH_3PbI_3$		Spin coatig annealing at 100 ºC		11.66	0.938	0.68	
25	$CH_3NH_3PbI_3$		Spin coatig annealing at 200 ºC		0.56	0.589	0.67	
26	$CH_3NH_3PbI_3$	PEDOT:PSS	Spin coatig with NH_4Cl additive	1.59	9.93	0.88	0.8011	123
27	$CH_3NH_3PbI_3$		Spin coatig with CH_3NH_3Cl additive		8.16	0.92	0.694	
28	$CH_3NH_3PbI_3$		Spin coatig with no additive		0.04	0.37	0.2753	
29	$CH_3NH_3PbI_{3-x}Cl_x$	PEDOT:PSS	Spin coatig with DIO additive	~1.5	11.8	0.92	0.73	124
30			Spin coatig with no additive		9	0.9	0.62	
31	$CH_3NH_3PbI_3$	spiro-MeOTAD	Fast deposition-crystallization	1.55	13.9	0.98	0.68	125
32			Spin coatig		1.5	0.52	0.52	
33	$CH_3NH_3PbI_2Br$	spiro-MeOTAD	Spin coatig	1.8	4.87	0.82	0.59	130
34	$CH_3NH_3PbI_3$			1.55	4.29	0.74	0.54	
35	$CH_3NH_3PbI_2Br$	/	Two-step deposition technique based on spin coatig and dipping	1.58	8.54	0.77	0.68	131
36	$CH_3NH_3PbI_3$			1.51	7.2	0.77	0.6	
37	$CH_3NH_3PbBr_3$			2.12	1.69	0.79	0.46	
38	$CH_3NH_3SnI_3$	spiro-MeOTAD	Spin coatig	1.3	5.44	0.716	0.5007	136
39	$CH_3NH_3Sn_{0.5}Pb_{0.5}I_3$			1.17	7.27	0.584	0.6032	
40	$CH_3NH_3PbI_3$			1.55	8.31	0.863	0.6803	
41	$FAPbI_3$	spiro-MeOTAD	Spin coatig	1.47	4.3	0.97	0.687	138
42	$FAPbI_3$	P3HT	Spin coatig	1.43	3.7	0.55	0.41	139
43			In situ dipping technology	1.43	7.5	0.84	0.5	
44	$FAPbI_3$	spiro-MeOTAD	Spin coatig	1.47	16.01	1.032	0.74	140
45	$FAPbI_3$	spiro-MeOTAD	Spin coatig	2.26	6.5	1.35	0.73	141
46	$MAPbI_3$			2.34	0.4	1.48	0.48	
47	$FAPbI_{3-x}Cl_x$	P3HT	Spin coatig	1.492	6.6	0.65	0.51	142
48	$MA_{0.6}FA_{0.4}PbI_3$	spiro-MeOTAD	Spin coatig	1.53	13.4	0.992	0.692	143
49	$Cs_{0.10}MA_{0.90}PbI_3$	PEDOT:PSS	Spin coatig	1.54	7.68	1.05	0.73	144
50	$MAPbI_3$			1.52	5.51	0.89	0.70	
51	$CsPbI_3$			2.05	0.09	0.79	0.45	
52	$CH_3NH_3PbI_{3-x}Cl_x$	PEDOT:PSS	Spray deposition	1.55	11.1	0.92	0.72	155
53	$CH_3NH_3PbI_3$	spiro-MeOTAD	Two-step deposition	/	9.5	0.89	0.58	156
54	$CH_3NH_3PbI_3$	spiro-MeOTAD	Spin coatig with DMSO solvent	/	10.8-13.5	/	/	157
55			Spin coatig with DMF solvent		1.3-14.2			
56	$CH_3NH_3PbI_3$	/	Modified two-step deposition	1.61	10.47	0.948	0.69	160
57	$CH_3NH_3PbI_{3-x}Cl_x$	spiro-MeOTAD	Spin coatig with thiophene additive	/	15.3	1.02	0.68	161
58			Spin coatig with pyridine additive		16.5	1.03	0.72	
59		spiro-MeOTAD			3.83	0.63	0.50	
60	$CH_3NH_3PbI_3$	Spiro+BuPyImTFSI	Spin coatig	1.55	7.91	0.87	0.56	163
61		Spiro + Li + TBP			8.16	0.91	0.57	
62	$CH_3NH_3PbI_3$	CuI	Spin coatig	1.55	6.0	0.55	0.62	173
63	$CH_3NH_3PbI_3$	CuSCN	Spin coatig	/	12.4	1.016	0.62	174

*: MA=CH_3NH_3, FA= formamidinium, some BGs are calculated by the absorption edge in the UV-vis spectra.

This journal is © The Royal Society of Chemistry 2012

The developed HTMs are all organic compounds, which are likely to remain expensive due to the synthetic methods and high purity required for photovoltaic applications. Therefore, the design of new inorganic HTMs is suggested. Compared with organic HTMs, inorganic p-type semiconductors appear to be an ideal choice given their high mobility, stability, ease of synthesis and low cost. Copper iodide (CuI) was recently reported as a hole conductor in lead halide perovskite-based devices, exhibiting a PCE of 6.0%.[173] CuI has a higher FF than that of spiro-MeOTAD because of its higher electrical conductivity. However, the efficiency obtained with CuI remains lower than that for spiro-MeOTAD because of the exceptionally high voltages obtained in spiro-MeOTAD solar cells. Recently, Qin et al. demonstrated an effective and inexpensive inorganic p-type HTM, copper thiocyanate (CuSCN), on $CH_3NH_3PbI_3$ perovskite-based devices. Using a low-temperature solution-process deposition method, a PCE of 12.4% was achieved under AM 1.5G solar simulation. This work opens the door for integrating a class of abundant and inexpensive material for photovoltaic applications.[174]

4.2.5.2 Stability

The degradation of $CH_3NH_3PbI_3$ is often ignored, which is nonetheless a large concern for practical applications. Perovskite $CH_3NH_3PbI_3$ films were observed to be extremely sensitive to moisture in air.[119] Grätzel and co-workers demonstrated that the device fabrication should be performed under controlled atmospheric conditions with a humidity of <1%.[119] Niu et al. systematically studied the stability of $CH_3NH_3PbI_3$ films and also observed that $CH_3NH_3PbI_3$ was sensitive to moisture.[175] To improve the stability of $CH_3NH_3PbI_3$, alumina oxide was used as a post-modification material in all-solid-state perovskite solar cells. Al_2O_3 was able to protect this perovskite from degradation. Moreover, the solar cells post-modified with Al_2O_3 exhibited more brilliant stability than those prepared without modification when exposed to moisture. The Al_2O_3 layer could act as an insulator barrier to protect $CH_3NH_3PbI_3$ from degradation by moisture and suppress the electron recombination between TiO_2 and spiro-MeOTAD. The restrained electron recombination is caused by the coverage of Al_2O_3 on TiO_2 and $CH_3NH_3PbI_3$, which is verified by the decreased dark current and increased interface resistance in the dark. This study would open a new pathway to improve the long-term performance of all-solid-state solar cells.

4.3 Other perovskite-based light absorbers

Ferroelectric perovskites have recently attracted attention as candidates for use in photovoltaic devices due to their special properties such as the promotion of the desirable separation of photo-excited carriers and allowing voltages higher than the BG.[176-180] Ferroelectric oxides are also stable in a wide range of mechanical, chemical and thermal conditions and can be fabricated using low-cost methods such as sol-gel thin-film deposition and sputtering. Grinberg et al. described a family of single-phase solid oxide solutions made from low-cost and non-toxic elements using conventional solid-state methods: $[KNbO_3]_{1-x}[BaNi_{1/2}Nb_{1/2}O_{3-\delta}]_x$ (KBNNO). These oxides exhibit both ferroelectricity and a wide variation of BGs in the range of 1.1-3.8 eV.[181] In particular, the x = 0.1 composition has a direct BG of 1.39 eV at room temperature and exhibits a photocurrent density that is approximately 50 times larger than that of the classic ferroelectric $(Pb,La)(Zr,Ti)O_3$ material. The ideal match of the BG of KBNNO to the solar spectrum, its compositional tuning throughout the visible range and its photo-response properties open up the possibility of ferroelectric photovoltaic efficiency of above 3% in a thin-film device and the use of ferroelectric materials as solar absorber layers and carrier separators in practical photovoltaics. The capability of KBNNO to absorb 3 to 6 times more solar energy than the current ferroelectric materials suggests a route to viable ferroelectric semiconductor-based cells for solar energy conversion and other applications. It is also important for ferroelectric perovskites as visible-light-absorber for solar cells. Similar results have also been reported by Zhou et al.[182], and it was observed that KBNNO with compositions x=0.1–0.3 have quite narrow E_{bg} of below 1.5 eV, much smaller than the 3.2 eV BG of the parent $KNbO_3$ (KNO), which is due to the increasing Ni 3d electronic states within the gap of KNO. Furthermore, the KBNNO materials exhibit room-temperature ferromagnetism (RTFM) near a tetragonal-to-cubic phase boundary. Upon increasing x from 0 to 0.3, the magnetism of the samples develops from diamagnetism to ferromagnetism and paramagnetism, originating from the ferromagnetic–antiferromagnetic competition. These results are helpful in the deeper understanding of phase transitions, E_{bg} tunability, and magnetism variations in perovskite oxides and demonstrate that such materials could play a potential role in perovskite solar cells and multiferroic applications.

Table 3 listed the photovoltaic performance of the selected perovskite light absorbers-based solar cells. $CH_3NH_3PbI_3$ is the most investigated material up to now, however, it suffered from large BG and small diffusion length of the electron-hole pair. The BG can be tailored by A site, B site and X site doping and replacement and some excellent results are obtained. The B-site doping of a less toxic element Sn^{4+} for Pb^{2+} was used to modify the $CH_3NH_3PbI_3$ materials to reduce the BG; however, the performance has not been satisfactory to date. In addition, some divergences are observed in the efficiency of Sn-doped $CH_3NH_3PbI_3$ light absorber in the literatures and more research is urgent to study the photovoltaic performance of the Sn-doped $CH_3NH_3PbI_3$ in the future. The doping of the A site of formamidinium and the X site by Cl or Br could be used to increase the diffusion length of $CH_3NH_3PbI_3$. However, the incorporation of Br led to an increase in BG and then a sharp decrease in PCE was obtained. Thus, the content of Br should be well controlled in the future research. $CH_3NH_3PbI_{3-x}Cl_x$ was demonstrated as a highly efficient light absorber with both high V_{oc} and PCE. However, it was reported that only 3-4% Cl could be incorporated in the X site of $CH_3NH_3PbI_3$, resulting a relative high BG, which is comparable to $CH_3NH_3PbI_3$. The doping of the A site of formamidinium can result a higher PCE than $CH_3NH_3PbI_3$ and it is expected that some other organic cations with suitable radius will be widely developed in the

future. It was found that HTM also played an important role in the achievement of high PCEs. Spiro-OMeTAD is more active than some other organic HTMs such as P3HT, etc. Some inorganic HTMs such as CuI and CuSCN are developed to reduce the high cost of spiro-OMeTAD although the photovoltaic performance was not satisfied up to now. As shown in Table 3, spin coating is the most investigated method for the preparation of the perovskite layer in solar cells. However, poor crystallinity and non-uniform morphology are always obtained with the spin coating method. Some modifications for the spin coating method such as introducing functional additives of NH_4Cl, CH_3NH_3Cl, 1,8-diiodooctane, thiophene and pyridine and replacement of DMF solvent by DMSO are investigated and some convincing results are reported. A PCE as high as 16.5% was delivered based on spin coating method with pyridine additive. Some advanced methods, such as vapor-assisted solution process, fast deposition crystallization, controllable passivation technique, two-step deposition, spray deposition etc. have been developed, and among them, vapor-assisted solution process was considered as the most efficient one. However, the PCEs with new methods are generally lower than those of spin coating, which needed to be improved accompanied with improved morphology and crystallinity.

4.4 Perovskite-based photoanodes

4.4.1 A brief overview of the photoanodes

DSSCs have received much attention due to their low fabrication cost and the capability of varying many components. A DSSC is typically composed of a sensitizer, an electron-transporting phase, a hole-transporting phase and current-collecting substrates. To overcome the problem of low energy conversion efficiency, tremendous efforts have been devoted to several areas, including the use of nanostructures of oxides and additional compact blocking layers to allow effective injection and collection of photo-generated charge carriers and the use of panchromatic dyes or multi-dye systems to improve the light-harvesting capabilities. Among the various methods to enhance the efficiency of DSSCs, the photoanode is highly critical in determining the performance because this component allows the practical use of the charge carriers that are generated by light harvesting. The most commonly used material is TiO_2 with a wide BG of 3.2 eV, whereas most relevant studies have focused on the modification of the TiO_2 electrodes.[183-190] However, the sole use of TiO_2 could limit the selection of other components. For instance, small semiconductor quantum dots occasionally cannot be used as sensitizers for a TiO_2 electrode because their CB level is lower than that of TiO_2; therefore, the excited photoelectrons cannot be injected from the sensitizer to TiO_2. Although several other oxides or mixed oxides such as ZnO, SnO_2, Nb_2O_5 and Zn_2SnO_4 have also been reported as photoanodes for DSSCs,[191-198] these materials always exhibit lower photovoltaic performance compared with DSSCs with TiO_2. Therefore, it is of great importance to develop highly active photoanodes to replace TiO_2. As mentioned above, some perovskites with ABO_3 structure exhibited superior photoactivity compared with TiO_2, and their activity as well as band structure could be well controlled by suitable doping or replacement of the A site and/or B site and the preparation methods.[108,199-203]

4.4.2 Material development

Recently, there have been many reports on the photovoltaic properties of $BaSnO_3$-based DSSCs because $BaSnO_3$ perovskite is an n-type semiconducting material with a BG of approximately 3.1 eV.[199-202] For example, various preparation methods including co-precipitation, hydrothermal reaction and solid-state reaction were employed by Guo et al. to synthesize $BaSnO_3$ particles to optimize the photoelectric activities of electrode materials.[199] The light-to-electricity conversion of 1.1% is preliminarily reached on the DSSC made of the co-precipitation-derived $BaSnO_3$ particles. However, Li et al. also reported the synthesis of one-dimensional $BaSnO_3$ hollow architectures with a length of 1.5-5 μm as a photoelectrode of DSSCs using $BaCO_3$@SnO_2 core-shell nanorods as precursors.[200] It was observed that the absorption band of $BaSnO_3$ is in the UV region and that N719-sensitized $BaSnO_3$ films exhibit a clear photovoltaic response. However, the performance of the above $BaSnO_3$-based DSSCs is very poor with conversion efficiencies lower than 1.1%.

Very recently, highly crystalline $BaSnO_3$ nanoparticles were synthesized by Kim et al. using a simple liquid-phase reaction followed by a calcination process.[201] A PCE of 5.2% was achieved for a DSSC with the synthesized $BaSnO_3$ nanoparticles acting as the photoanode, which was fabricated without any functional layers or treatments. The formation process of these $BaSnO_3$ nanoparticles is summarized in Fig. 29. Initially, amorphous $BaSnO_3$ particles were precipitated before the particles gradually crystallized to form low-crystalline peroxo-precursor particles during the liquid-phase reaction; these precursor particles then formed highly crystalline $BaSnO_3$ perovskite nanoparticles through calcination.

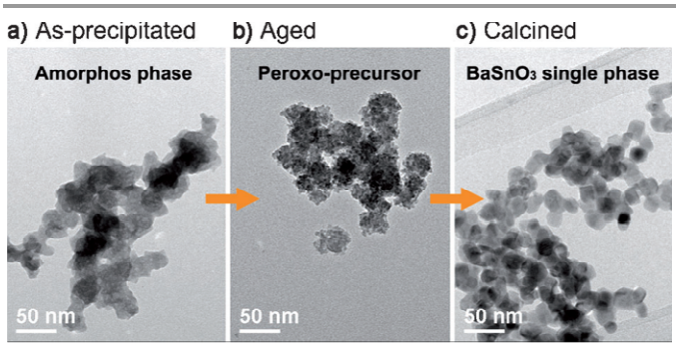

Fig. 29 The formation process of $BaSnO_3$ nanoparticles shown with TEM images of a) as-precipitated powders, b) precursor powders obtained at a liquid phase reaction time of 12 h, and c) calcined powders in air. Reproduced with permission from ref. 201. Copyright 2013, Wiley-VCH Verlag GmbH & Co. KGaA, Weinheim.

The thickness of the $BaSnO_3$ film was observed to strongly affect the photovoltaic performance. An obvious increase in efficiency was observed with increasing thickness of the $BaSnO_3$ film, and the highest efficiency was obtained at a

 This journal is © The Royal Society of Chemistry 2012

thickness of 43 μm; further increase in thickness did not have a positive effect. The highest photovoltaic performance, which was obtained from the DSSC based on the 43 μm-thick $BaSnO_3$ film, was attributed to its superior electron collection property, which indicates that $BaSnO_3$ has great potential for use as a photoanode material in DSSCs. Shin et al. studied the effect of $TiCl_4$ treatment on the physical, chemical and photovoltaic properties of $BaSnO_3$-based DSSCs.[202] The $TiCl_4$ treatment was observed to form an ultrathin TiO_2 layer on the $BaSnO_3$ surface. The formation of the TiO_2 shell layer improved the charge-collection efficiency by enhancing the charge transport and suppressing the charge recombination. The optimized treatment time to achieve a high efficiency of 5.5% compared with 4.5% for the bare $BaSnO_3$ was observed to be 3 min. The conversion efficiency could be further increased to 6.2% by increasing the thickness of the $BaSnO_3$ film, which is one of the highest reported efficiencies from non-TiO_2-based DSSCs. Further study is needed to completely understand the physical origin of such remarkable electron transport properties and to considerably enhance the photovoltaic performance of the $BaSnO_3$ cells.

In addition to the development of new perovskite photoanodes such as $BaSnO_3$, substitution of cations such as Ca^{2+}, Sr^{2+} and Ba^{2+} in the crystal lattice of TiO_2 to modify the electronic structure of TiO_2 to form a Ti-based perovskite, which was then applied as the photoanodes for solar cells, was also reported.[108,203] $MTiO_3$ (M = Ca, Sr and Ba) perovskite oxides with specific morphologies were fabricated in alkaline solution at low temperature via a soft chemical route for potential applications in solar cells.[74] The as-prepared $CaTiO_3$ exhibited a microtubular structure with a rectangular cross section, whereas the $SrTiO_3$ and $BaTiO_3$ exhibited assemblies consisting of aggregated particles in a compact fashion. Based on the experimental results, the authors proposed two types of growth mechanisms to study the formation processes of $CaTiO_3$, $SrTiO_3$ and $BaTiO_3$ microstructures, respectively. As shown in Fig. 30, the fabrication of microtubular $CaTiO_3$ underwent the initial dissolution of titanate nanofibers via the Ostwald ripening process for conversion into micrometer-sized fiber-bundles, whereas recrystallization occurred simultaneously until tubular microstructures were obtained. The formation of $SrTiO_3$ and $BaTiO_3$ microstructures involved ion exchange reaction and an in-situ growth process at the self-sacrifice of the titanate nanofiber framework based on the chemical reactivity. In addition, the $CaTiO_3$ microtubes exhibited better photoelectrochemical performance than the $SrTiO_3$ and $BaTiO_3$ microstructures, suggesting their potential applications in solar cells as photoanodes.

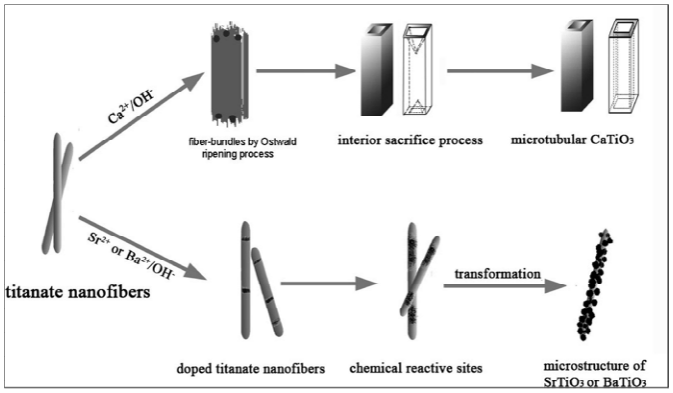

Fig. 30 Schematic illustration of the possible formation mechanism of $MTiO_3$ (M = Ca, Sr and Ba) perovskites with various morphologies. Reproduced with permission from ref. 108. Copyright 2009, American Chemical Society.

5. Conclusions and perspectives

In this review, we have discussed the recent progress in the field of photocatalysis and photovoltaic reactions based on perovskite-type functional materials. Our aims were to review the present research on the development of and strategies for the designation of the perovskite materials in photocatalysis and photovoltaics-related energy conversion and environmental treatment to provide some useful guidelines for future research. Although great progress has been made during recent decades, considerable research is needed to realize the widespread application of perovskites in the photocatalysis and photovoltaics-related energy conversion and environmental treatment to achieve a sustainable future.

5.1 Catalysts for water splitting reaction

For the hydrogen production from water splitting reaction, research is focused on the development of photocatalysts and strategies to improve photocatalytic activity. Because there is an activation barrier for surface chemical reactions that evolve H_2 and O_2, a photocatalyst with a 600 nm absorption edge would be optimal for this reaction. Therefore, more efficient photocatalytic materials with a BG as narrow as 2 eV must be developed. The main achievement, problems and perspectives are shown below.

1. The proper doping of the A, B and X sites in the perovskite is the most investigated method to reduce BG. Non-metal doping, in particular nitrogen doping, was observed to be an effective approach to improve the photoactivity of perovskite catalysts under visible light. Several candidates, such as $CaNbO_2N$, $SrNbO_2N$, $BaNbO_2N$, $LaNbON_2$, which have BGs of approximately 2 eV, have already been developed. However, among these catalysts, only $CaNbO_2N$ had considerable activity for water splitting. The different activities of various perovskites with similar BG should be attributed to the different energy positions of the VB and CB. It can be concluded that not only the value of the BG but also its absolute energy position should be optimized for the water splitting reaction.

2. The suppression of the electron-hole pair recombination is also essential for the achievement of high photocatalytic activity, and some strategies have been explored, such as A-site doping, the development of advanced synthesis methods such as hydrothermal method to reduce the particle size and forming a nanostructure in the surface of the catalysts. However, till now, limited elements have been investigated for the A site doping to form a nanostructure.

3. In the future research on the photocatalytic water-splitting reaction, in addition to the search for new photocatalysts and improvement of their preparation methods, an investigation of the reaction mechanisms should be focused in the future. There are some technological problems that must still be overcome, such as the design and materials for large-scale reactors, the supply of water and the environmentally benign separation of O_2 from explosive H_2 and O_2 mixtures. Extensive research is still needed to overcome these problems.

5.2 Catalysts for degradation of organic dyes

Based on the steps of degradation reactions of organic dyes, the key to improve the photocatalytic activity is to suppress electron-hole recombination and to reduce E_{bg}. The doping and selection of A and B sites as well as the doping of N in the X site are useful to reduce E_{bg}, and some advanced methods as well as A-site or B-site doping to reduce the particle size are effective for suppressing electron-hole recombination. The main achievement, problems and perspectives are shown below.

1. For example, the incorporation of 5 mol.% Co to the B site of $CeCo_xTi_{1-x}O_{3+\delta}$ perovskite catalysts led to a reduction in the BG from 2.15 eV to 1.57 eV. The E_{bg} decreased from 4.13 eV for the undoped $NaTaO_3$ sample to 3.14 eV for the 6.39 mol.% Cr^{3+} doped sample. It should be noted that, the amount of the doped element should be well controlled as excessive doping amount may have negative effect on the photocatalytic activity.

2. Many methods are suitable for the preparation of perovskite-based photocatalysts such as microwave, sol-gel, hydrothermal, ultrasonic irradiation-assisted self-combustion and surface-ion adsorption methods. Among these approaches, the hydrothermal and microwave techniques have attracted increasing attention for nanostructured catalysts and some excellent results have been reported. However, besides hydrothermal method, some other methods are limited to prepare a specific perovskite, which have not demonstrated as general methods for the perovskite synthesis.

3. In addition to the development of perovskite-based photocatalysts, several key technical constraints for some other aspects exist such as the need for a catalyst immobilization strategy to provide a cost-effective solid-liquid separation, improvement of the photocatalytic operation for wider pH, and effective design of a photocatalytic reactor system for higher utilization of solar energy to reduce the costs. In addition, the low efficiency design of current solar collecting technology has encouraged the developmental progress of photocatalytic technology in the water treatment industry.

5.3 Light absorbers for perovskite-based solar cells

Rapid progress in the development of perovskite solar cells has been attained in recent years. The strategies for the designation of perovskite light absorbers include band gap engineering, increasing the diffusion length to reduce the electron-hole pair recombination and improving the crystallinity and morphology of the perovskite film. The main achievement, problems and perspectives are shown below.

1. To date, there are few reports of other candidates from $CH_3NH_3PbI_3$-based materials that are suitable for solar cells. The B-site doping of a less toxic element Sn^{4+} for Pb^{2+} was used to modify the $CH_3NH_3PbI_3$ materials to reduce the BG; however, the performance has not been satisfactory to date. Many elements such as Co^{2+}, Fe^{2+}, Mn^{2+}, Pd^{2+} and Ge^{2+} can be incorporated through various structural adaptations with the guidance of the Goldschmidt tolerance factor to form a stable perovskite structure. The A-site doping of $CH_3NH_3PbI_3$ was limited to several organic cations, such as alkylammonium, formamidinium as well as methylviologen and the related reports are limited. In the future, the combination of A sites, B sites and/or I sites could be a useful method to develop highly active $CH_3NH_3PbI_3$-based light absorbers and $FAPb_{1-x}Sn_xI_{3-x}Cl_x$ may be a possible candidate for light absorbers in perovskite-based solar cells. In addition, theoretical calculations are needed to provide guidance to identify newer families of photovoltaic perovskites.

2. The doping of the A site of formamidinium and the I site by Cl or Br could be used to increase the diffusion length of $CH_3NH_3PbI_3$ to suppress the electron-hole recombination. In addition, the stability of the perovskite under wet conditions should be well addressed, although there were a few pre-treated methods to improve the stability. Well-designed doping processes and/or pre-treatment processes would also be effective ways to enhance the stability against moisture.

3. The HTM in the perovskite-based solar cells is currently the bottleneck for the realization of cost-effective and stable devices. The most investigated HTM is spiro-MeOTAD, which exhibits low conductivity and other problems, leading to a low PCE. Adding different types of functional additives such as BuPyIm-TFSI to spiro-MeOTAD can improve the PCE of the solar cells. In addition, due to the high cost of spiro-MeOTAD and some new organic HTMs, some inorganic HTMs, such as CuI and CuSCN, have been investigated, although the PCEs were relatively low. These works may bring a new aspect to the development of HTMs for perovskite-based solar cells.

4. The deposition methods of perovskite films have a strong effect on the crystallinity and morphology of the film and thus the performance of the solar cells. The simplicity of making solar-cell components via liquid-phase chemical reactions and depositing the materials by methods such as spraying, spin coating, screen-printing and ink-jet printing may make their use widespread in practical applications in the future.

5.4 Photoanodes for DSSCs

This journal is © The Royal Society of Chemistry 2012

Perovskite materials have also been investigated as photoanodes in solar cells. For the development of perovskite photoanodes, $BaSnO_3$ and some titanates have been used. For $BaSnO_3$, a PCE of 5.2% was achieved for a DSSC with the synthesized $BaSnO_3$ nanoparticles as the photoanode, which was fabricated without any functional layers or treatments; this value is higher than that of the previously investigated conventional $BaSnO_3$ anode. Further study is needed to understand the physical origin of such remarkable electron transport properties as well as the operation principles or mechanism of the $BaSnO_3$-based solar cells with improved performance. For the titanates, the selection of A-site elements is very important for the improvement of the photoactivity. Novel architectures should be widely used in this field because there are numerous opportunities for further improvements through systematically engineering high-electron-mobility electrodes, such as nanofibers, nanospheres, nanowires and nanocubes.

Acknowledgements

The authors would like to thank the Australia Research Council for supporting the project under contract FT100100134. Dr. Wei Wang also acknowledges Curtin University for a postdoctoral fellowship.

Notes and references

[a] Department of Chemical Engineering, Curtin University, Perth, WA 6845, Australia.
[b] State Key Laboratory of Materials-Oriented Chemical Engineering, Nanjing Tech University, Nanjing, 210009, China.
E-mail: zongping.shao@curtin.edu.au and shaozp@njtech.edu.cn.

1 S. Sadhishkumar and T. Balusamy, *Renew. Sust. Energ. Rev.*, 2014, **37**, 191-198.
2 G.Y. Chen, J. Seo, C.H. Yang and P.N. Prasad, *Chem. Soc. Rev.*, 2013, **42**, 8304-8338.
3 M. Kitano and M. Hara, *J. Mater. Chem.*, 2010, **20**, 627-641.
4 M.N. Chong, B. Jin, C.W.K. Chow and C. Saint, *Water Res.*, 2010, **44**, 2997-3027.
5 V.S. Reddy, S.C. Kaushik, K.R. Ranjan and S.K. Tyagi, *Renew. Sust. Energ. Rev.*, 2013, **27**, 258-273.
6 M. Ni, M.K.H. Leung, D.Y.C. Leung and K. Sumathy, *Renew. Sust. Energ. Rev.*, 2007, **11**, 401-425.
7 R. Abe, *J. Photoch. Photobio. C*, 2010, **11**, 179-209.
8 C.M. Teh and A.R. Mohamed, *J. Alloy Compd.*, 2011, **509**, 1648-1660.
9 U.I. Gaya and A.H. Abdullah. *J. Photoch. Photobio. C*, 2008, **9**, 1-12.
10 K. Fominykh, J.M. Feckl, J. Sicklinger, M. Döblinger, S. Böcklein, J. Ziegler, L. Peter, J. Rathousky, E.W. Scheidt, T. Bein and D. Fattakhova-Rohlfing, *Adv. Funct. Mater.*, 2014, **24**, 3123-3129.
11 Y. Cheng, C. Liu, H.M. Cheng and S.P. Jiang, *ACS Appl. Mater. Inter.*, 2014, **6**, 10089-10098.
12 W. Zhang, H.L. Tay, S.S. Lim, Y.S. Wang, Z.Y. Zhong and R. Xu, *Appl. Catal. B-Environ.*, 2010, **95**, 93-99.
13 M. Sharma, T. Jain, S. Singh and O.P. Pandey, *Sol. Energy*, 2012, **86**, 626-633.
14 J. Soldat, R. Marschall and M. Wark, *Chem. Sci.*, 2014, **5**, 3746-3752.
15 Y.H. Yang, Q.Y. Chen, Z.L. Yin and J. Li, *J. Alloy Compd.*, 2009, **488**, 364-369.
16 J. Hu, J.H. Ma, L.N. Wang and H. Huang, *J. Alloy Compd.*, 2014, **583**, 539-545.
17 H.P. Zhang, M.K. Lü, S.W. Liu, L.Y. Wang, Z.L Xiu, Y.Y. Zhou, Z.F. Qiu, A.Y. Zhang and Q. Ma, *Mater. Chem. Phys.*, 2009, **144**, 716-721.
18 W. Shockley and H.J. Queisser, *J. Appl. Phys.*, 1961, **32**, 510-519.
19 G. Conibeer, *Mater. Today*, 2007, **10**, 42-50.
20 B. O'Regan and M. Grätzel, *Nature*, 1991, **353**, 737-740.
21 G. Li, V. Shrotriya, J.S. Huang, Y. Yao, T. Moriarty, K. Emery and Y. Yang, *Nat. Mater.*, 2005, **4**, 864-868.
22 T. Todorov and D.B. Mitzi, Eur. *J. Inorg. Chem.*, 2010, 17-28.
23 E.H. Sargent, *Nat. Photonics*, 2012, **6**, 133-135.
24 J.H. Yang, D.E. Wang, H.X. Han and C. Li, *Acc. Chem. Res.*, 2013, **46**, 1900-1909.
25 W.J. Youngblood, S.A. Lee, M. Maeda and T.E. Mallouk, *Acc. Chem. Res.*, 2009, **42**, 1966-1973.
26 K. Maeda, T. Ohno and K. Domen, *Chem. Sci.*, 2011, **2**, 1362-1368.
27 P. Zhang, J.J. Zhang and J.L. Gong, *Chem. Soc. Rev.*, 2014, **43**, 4395-4422.
28 W.N. Zhao and Z.P. Liu, *Chem. Sci.*, 2014, **5**, 2256-2264.
29 M. Kitanoa, M. Matsuoka, M. Ueshima and M. Anpo, *Appl. Catal. A-Gen.*, 2007, **325**, 1-14.
30 E. Thimsen, S. Biswas, C.S. Lo and P. Biswas, *J. Phys. Chem. C*, 2009, **113**, 2014-2021.
31 K. Maeda and K. Domen, *J. Phys. Chem. C*, 2007, **111**, 7851-7861.
32 K. Maeda, *J. Photoch. Photobio. C*, 2011, **12**, 237-268.
33 A. Kudo and Y. Miseki, *Chem. Soc. Rev.*, 2009, **38**, 253–278
34 M. Kitano, M. Takeuchi, M. Matsuoka, J.M. Thomas and M. Anpo, *Catal. Today*, 2007, **120**, 133-138.
35 O. Khaselev and J.A. Turner, *Science*, 1998, **280**, 425-427.
36 F.L. Fu, W.J. Han, B. Tang, M. Hu and Z.H. Cheng, *Chem. Eng. J.*, 2013, **232**, 534-540.
37 R.T.P. Pint, L. Lintomen, L.F.L. Luz Jr. and M.R. Wolf-Maciel. *Fluid Phase Equilibr.*, 2005, **228-229**, 447-457.
38 M. Köck-Schulmeyera, M. Villagrasa, M.L.D. Alda, R. Céspedes-Sánchez, F. Ventura and D. Barceló, *Sci. Total Environ.*, 2013, **458-460**, 466-476.
39 I.K. Konstantinou and T.A. Albanis, *Appl. Catal. B-Environ.*, 2014, **49**, 1-14.
40 S. Dawood, T.K. Sen, *J. Chem. Proc. Engg.*, 2014, **1**, 1-11.
41 E. Forgacs, T. Cserháti and G. Oros, *Environ. Int.*, 2004, **30**, 953-971.
42 F. Han, V.S.R. Kambala, M. Srinivasan, D. Rajarathnam and R. Naidu, *Appl. Catal. A-Gen.*, 2009, **359**, 25-40.
43 F. Lin, Y.N. Zhang, L. Wang, Y.L. Zhang, D.E. Wang, M. Yang, J.H. Yang, B.Y. Zhang, Z.X. Jiang and C. Li, *Appl. Catal. B-Environ.*, 2012, **127**, 363-370.
44 J. Huang, H. Zhang, X.G. Zhou and X.H. Zhong, *Mater. Chem. Phys.*, 2013, **138**, 755-761.
45 Priyanka, V.C. Srivastava, *Ind. Eng. Chem. Res.*, 2013, **52**, 17790-17799.

46 X.Z. Li and F.B. Li, *Environ. Sci. Technol.*, 2001, **35**, 2381-2387.
47 C.Y. Yi, F. Giordano, N. Cevey-Ha, H.N. Tsao, S.M. Zakeeruddin and M. Grätzel, *ChemSusChem*, 2014, **7**, 1107-1113.
48 J.A. Chang, S.H. Im, Y.H. Lee, H.J. Kim, C.S. Lim, J.H. Heo and S.I. Seok, *Nano Lett.*, 2012, **12**, 1863-1867.
49 J. Burschka, A. Dualeh, F. Kessler, E. Baranoff, N.L. Cevey-Ha, C.Y. Yi, M.K. Nazeeruddin and M. Grätzel, *J. Am. Chem. Soc.*, 2011, 133, 18042-18045.
50 H.S. Kim, C.R. Lee, J.H. Im, K.B. Lee, T. Moehl, A. Marchioro, S.J. Moon, R. Humphry-Baker, J.H. Yum, J.E. Moser, M. Grätzel and N.G. Park, *Sci. Rep.*, 2012, **2**, 591.
51 M.M. Lee, J. Euscher, T. Miyasaka, T.N. Murakami and H.J. Snaith, *Science*, 2012, **338**, 643-647.
52 H.S. Kim, S.H. Im and N.G. Park, *J. Phys. Chem. C*, 2014, **118**, 5615-5625.
53 H.S. Kim, I. Mora-Sero, V. Gonzalez-Pedro, F. Fabregat-Santiago, E.J. Juarez-Perez, N.G. Park and J. Bisquert, *Nat. Commun.*, 2013, **4**, 2242.
54 J.M. Ball, M.M. Lee, A. Hey and H.J. Snaith, *Energy Environ. Sci.*, 2013, **6**, 1739-1743.
55 M.Z. Liu, M.B. Johnston and H.J. Snaith, *Nature*, 2013, **501**, 395-398.
56 G.E. Eperon, V.M. Burlakov, P. Docampo, A. Goriely and H.J. Snaith, *Adv. Funct. Mater.*, 2014, **24**, 151-157.
57 V.M. Goldschmidt, *Ber. Dtsch. Chem. Ges.*, 1927, **60**, 1263-1268.
58 C.H. Li, K.C.K. Soh and P. Wu, *J. Alloy Compd.*, 2004, **372**, 40-48.
59 C.Li, X.G. Lu, W.Z. Ding, L.M. Feng, Y.H. Gao and Z.M. Guo, *Acta Crystallogr. Sect. B: Struct. Sci.*, 2008, **B64**, 702-707.
60 L.Q. Jiang, J.K. Guo, H.B. Liu, M. Zhu, X. Zhou, P. Wu and C.H. Li, *J. Phys. Chem. Solids*, 2006, **67**, 1531-1536.
61 V. Rodríguez-González, X.L. García-Montelongo, L.L. Garza-Tovar, S.W. Lee and L.W. Torres-Martínez, *Res. Chem. Intermed*, 2009, **35**, 187-196.
62 K. Maeda and K. Domen, *J. Catal.*, 2014, **310**, 67-74.
63 K. Onozuka, Y. Kawakami, H. Imai, T. Yokoi, T. Tatsumi and J.N. Kondo, *J. Solid State Chem.*, 2012, **192**, 87-92.
64 B. Wang, S.M. Wang, L.X. Gong and Z.F. Zhou, *Ceram. Int.*, 2012, **38**, 6643-6649.
65 Z.X. Wei, Y. Wang, J.P. Liu, C.M. Xiao and W.W. Zeng, *Mater. Chem. Phys.*, 2012, **136**, 755-761.
66 W.J. Yin, H.W. Tang, S.H. Wei, M.M. Al-Jassim, J. Turner and Y.F. Yan, *Phys. Rev. B*, 2010, **82**, 045106.
67 J.P. Zou, L.Z. Zhang, S.L. Luo, L.H. Leng, X.B. Luo, M.J. Zhang, Y. Luo and G.C. Guo, *Int. J. Hydrogen Energy*, 2012, **37**, 17068-17077.
68 B. Siritanaratkul, K. Maeda, T. Hisatomi and K. Domen, *ChemSusChem*, 2011, **4**, 74-78.
69 P. Li, S.X. Ouyang, G.C. Xi, T. Kako and J.H. Ye, *J. Phys. Chem. C*, 2012, **116**, 7621-7628.
70 H. Kato, K. Asakura and A. Kudo, *J. Am. Chem. Soc.*, 2003, **125**, 3082-3089.
71 S.D. Li, L.Q. Jing, W. Fu, L.B. Yang, B.F. Xin and H.G. Fu, *Mater. Res. Bull.*, 2007, **42**, 203-212.
72 S. Thirumalairajan, K. Girija, N.Y. Hebalkar, D. Mangalaraj, C. Viswanathan and N. Ponpandian, *RSC Adv.*, 2013, **3**, 7549-7561.
73 J.W. Liu, G. Chen, Z.H. Li and Z.G. Zhang, *Int. J. Hydrogen Energy*, 2007, **32**, 2269-2272.
74 H. Kato, H. Kobayashi and A. Kudo, *J. Phys. Chem. B*, 2002, **106**, 12441-12447.
75 H.J. Zhang, G. Chen, Y.X. Li and Y.J. Teng, *Int. J. Hydrogen Energy*, 2010, **35**, 2713-2716.
76 R. Konta, T. Ishii, H. Kato and A. Kudo, *J. Phys. Chem. B*, 2004, **108**, 8992-8995.
77 J.N. Yun, Z.Y. Zhang, J.F. Yan and W. Zhao, *Thin Solid Films*, 2013, **542**, 276-280.
78 D.W. Hwang, H.G. Kim, J.S. Lee, J. Kim, W. Li, S.H. Oh, *J. Phys. Chem. B*, 2005, **109**, 2093-2102.
79 M. Machida, K. Miyazaki, S. Matsushima, M. Arai, *J. Mater. Chem.*, 2003, **13**, 1433-1437.
80 M. Machida, J. Yabunaka and T. Kijima, *Chem. Mater.*, 2000, **12**, 813-817.
81 J. Yin, Z.G. Zou and J.H. Ye, *J. Phys. Chem. B*, 2003, **107**, 61-65.
82 S. Balaz, S.H. Porter, P.M. Woodward and L.J. Brillson, *Chem. Mater.*, 2013, **25**, 3337-3343.
83 C.L. Paven-Thivet, A. Ishikawa, A. Ziani, L.L. Gendre, M. Yoshida, J. Kubota, F. Tessier and K. Domen, *J. Phys. Chem. C*, 2009, **113**, 6156-6162.
84 A. Kudo, R. Niishiro, A. Iwase and H. Kato, *Chem. Phys.*, 2007, **339**, 104-110.
85 A. Iwase, H. Kato and A. Kudo, *ChemSusChem*, 2009, **2**, 873-877.
86 S.N. Tijare, M.V. Joshi, P.S. Padole, P.A. Mangrulkar, S.S. Rayalu and N.K. Labhsetwar, *Int. J. Hydrogen Energy*, 2012, **37**, 10451-10456.
87 J.Y. Shi, G.J. Liu, N. Wang and C. Li, *J. Mater. Chem.*, 2012, **22**, 18808-18813.
88 K. Inaba, S. Suzuki, Y. Noguchi, M. Miyayama, K. Toda and M. Sato, *Eur. J. Inorg. Chem.*, 2008, 5471-5475.
89 N. Nuraje, X.N. Dang, J.F. Qi, M.A. Allen, Y. Lei and A.M. Belcher, *Adv. Mater.*, 2012, **24**, 2885-2889.
90 W.F. Zhang, J.W. Tang and J.H. Ye, *Chem. Phys. Lett.*, 2006, **418**, 174-178.
91 C.W. Lee, D.W. Kim, I.S. Cho, S. Park, S.S. Shin, S.W. Seo and K.S. Hong, *Int. J. Hydrogen Energy*, 2012, **37**, 10557-10563.
92 C.C. Hu and H. Teng, *Appl. Catal. A-Gen.*, 2007, **331**, 44-50.
93 Y.Y. Li, S.S. Yao, W. Wen, L.H. Xue and Y.W. Yan, *J. Alloy Compd.*, 2010, **491**, 560-564.
94 D.Q. Fei, T. Hudaya and A.A. Adesina, *Catal. Commun.*, 2005, **6**, 253-258.
95 Y.G. Su, S.W. Wang, Y. Meng, H. Han and X.J. Wang, *RSC Adv.*, 2012, **2**, 12932-12939.
96 M. Yang, X.L. Huang, S.C. Yan, Z.S. Li, T. Yu and Z.G. Zou, *Mater. Chem. Phys.*, 2010, **121**, 506-510.
97 H. Zhu, J. Tao and X. Dong, *J. Phys. Chem. C*, 2010, **114**,2873-2879.
98 V. Kumar, Govind and S. Uma, *J. Hazard. Mater.*, 2011, **89**, 502-508.
99 Y.F. Huang, Y.L. Wei, S.H. Cheng, L.Q. Fan, Y.B. Li, J.M. Lin and J.H. Wu, *Sol. Energy Mater. Sol. Cells*, 2010:94:761-766.
100 F.T. Li, Y. Liu, R.H. Liu, Z.M. Sun, D.S. Zhao and C.G. Kou, *Mater. Lett.*, 2010, **64**, 223-225.
101 Z.H. Li, H. Xue, X.X. Wang and X.Z. Fu, *J. Mol. Catal. A-Chem.*, 2006, **260**, 56-61.

This journal is © The Royal Society of Chemistry 2012

102 P.S. Tang, Y. Tong, H.F. Chen, F. Cao and G.X. Pan, *Curr. Appl. Phys.*, 2013, **13**, 340-343.
103 S. Thirumalairajan, K. Girija, I. Ganesh, D. Mangalaraj, C. Viswanathan, A. Balamurugan and N. Ponpandian, *Chem. Eng. J.*, 2012, **209**, 420-428.
104 W.Y. Jung, S.S. Hong, *J. Ind. Eng. Chem.*, 2013, **19**, 157-160.
105 S.S. Fu, H.L. Niu, Z.Y. Tao, J.M. Song, C.J. Mao, S.Y. Zhang, C.L. Chen and D. Wang, *J. Alloy Compd.*, 2013, **576**, 5-12.
106 G.K. Zhang, J. Gong, H.H. Gan and F. Lü, *J. Alloy Compd.*, 2011, **509**, 9791-9797.
107 P. Gao, M. Grätzel and M.K. Nazeeruddin, *Energy Environ. Sci.*, 2014, **7**, 2448-2463.
108 Y. Li, X.P. Gao, G.R. Li, G.L. Pan, T.L. Yan and H.Y. Zhu, *J. Phys. Chem. C*, 2009, **113**, 4386-4394.
109 S.R. Basu, L.W. Martin, Y.H. Chu, M. Gajek, R. Ramesh, R.C. Rai, X. Xu and J.L. Musfeldt, *Appl. Phys. Lett.*, 2008, **92**, 091905.
110 S.A. Kulkarni, T. Baikie, P.P. Boix, N. Yantara, N. Mathews and S. Mhaisalkar, *J. Mater. Chem. A*, 2014, **2**, 9221-9225.
111 A. Kojima, K. Teshima, Y. Shirai and T. Miyasaka, *J. Am. Chem. Soc.*, 2009, **131**, 6050-6051.
112 J.H. Im, J. Chung, S.J. Kim and N.G. Park, *Nanoscale Res. Lett.*, 2012, **7**, 353.
113 G.E. Eperon, S.D. Stranks, C. Menelaou, M.B. Johnston, L.M. Herz and H.J. Snaith, *Energy Environ. Sci.*, 2014, **7**, 982-988.
114 J. Fujisawa and G. Giorgi, *Phys. Chem. Chem. Phys.*, 2014, **16**, 17955-17959.
115 J.L. Knutson and J.D. Martin, *Inorg. Chem.*, 2005, **44**, 4699-4705.
116 Y. Ogomi, A. Morita, S. Tsukamoto, T. Saitho, N. Fujikawa, Q. Shen, T. Toyoda, K. Yoshino, S.S. Pandey, T.L. Ma and S. Hayase, *J. Phys. Chem. Lett.*, 2014, **5**, 1004-1011.
117 G.H. Xing, N. Mathews, S.Y. Sun, S.S. Lim, Y.M. Lam, M. Grätzel, S. Mhaisalkar and T.C. Sum, *Science*, 2013, **342**, 344-347.
118 S.D. Stranks, G.E. Eperon, G. Grancini, C. Menelaou, M.G.P. Alcocer, T. Leijtens, L.M. Herz, A. Petrozza and H.J. Snaith, *Science*, 2013, **342**, 341-344.
119 J. Burschka, N. Pellet, S.J. Moon, R. Humphry-Baker, P. Gao, M.K. Nazeeruddin, M. Grätzel, *Nature*, 2013, **499**, 316-319.
120 Q. Chen, H.P. Zhou, Z. Hong, S. Luo, H.S. Duan, H.H. Wang, Y.S. Liu, G. Li and Y. Yang, *J. Am. Chem. Soc.*, 2014, **136**, 622-625.
121 Q. Chen, H.P. Zhou, T.B. Song, S. Luo, Z.R. Hong, H.S. Duan, L.T. Dou, Y.S. Liu and Y. Yang, *Nano Lett.*, 2014, **14**, 4158-4163.
122 A. Dualeh, N. Tétreault, T. Moehl, P. Gao, M.K. Nazeeruddin and M. Grätzel, *Adv. Funct. Mater.*, 2014, **24**, 3250-3258.
123 C.T. Zuo and L.M. Ding, *Nanoscale*, 2014, **6**, 9935-9938.
124 P.W. Liang, C.Y. Liao, C.C. Chueh, F. Zuo, S.T. Williams, X.K. Xin, J.J. Lin and A.K.Y. Jen, *Adv. Mater.*, 2014, **26**, 3748-3754.
125 M.D. Xiao, F.Z. Huang, W.C. Huang, Y. Dkhissi, Y. Zhu, J. Etheridge, A. Gray-Weale, U. Bach, Y.B. Cheng and L. Spiccia, *Angew. Chem. Int. Ed.*, 2014, **53**, 9898-9903.
126 Y. Wang, T. Gould, J.F. Dobson, H.M. Zhang, H.G. Yang, X.D. Yao and H.J. Zhao, *Phys. Chem. Chem. Phys.*, 2014, **16**, 1424-1429.
127 G. Giorgi, J. Fujisawa, H. Segawa and K. Yamashita, *J. Phys. Chem. C*, 2014, **118**, 12176-12183.
128 C. Quarti, G. Grancini, E. Mosconi, P. Bruno, J.M. Ball, M.M. Lee, H.J. Snaith, A. Petrozza and F.D. Angelis, *J. Phys. Chem. Lett.*, 2014, **5**, 279-284.
129 E. Edri, S. Kirmayer, D. Cahen and G. Hodes, *J. Phys. Chem. Lett.*, 2013, **4**, 897-902.
130 J.H. Qiu, Y.C. Qiu, K.Y. Yan, M. Zhong, C. Mu, H. Yan and S.H. Yang, *Nanoscale*, 2013, **5**, 3245-3248.
131 S. Aharon, B.E. Cohen and L. Etgar, *J. Phys. Chem. C*, 2014, **118**, 17160-17165.
132 Y.X. Zhao and K. Zhu, *J. Am. Chem. Soc.*, 2014, **136**, 12241-12244.
133 I. Chung, B. Lee, J.Q. He, R.P.H. Chang and M.G. Kanatzidis, *Nature*, 2012, 485, 486-489.
134 E. Mosconi, A. Amat, M.K. Nazeeruddin, M. Grätzel and F.D. Angelis, *J. Phys. Chem. C*, 2013, **117**, 13902-13913.
135 S. Nagane, U. Bansode, O. Game, S. Chhatre and S. Ogale, *Chem. Commun.*, 2014, **50**, 9741-9744.
136 F. Hao, C.C. Stoumpos, R.P.H. Chang and M.G. Kanatzidis, *J. Am. Chem. Soc.*, 2014, **136**, 8094-8099.
137 N.K. Noel, S.D. Stranks, A. Abate, C. Wehrenfennig, S. Guarnera, A.A. Haghighirad, A. Sadhanala, G.E. Eperon, S.K. Pathak, M.B. Johnston, A. Petrozza, L.M. Herz and H.J. Snaith, *Energy Environ. Sci.*, 2014, **7**, 3061-3068.
138 T.M. Koh, K.W. Fu, Y.N. Fang, S. Chen, T.C. Sum, N. Mathews, S.G. Mhaisalkar, P.P. Boix and T. Baikie, *J. Phys. Chem. C*, 2014, **118**, 16458-16462.
139 S.P. Pang, H. Hu, J.L. Zhang, S.L. Lv, Y.M. Yu, F. Wei, T.S. Qin, H.X. Xu, Z.H. Liu and G.L. Cui, *Chem. Mater.*, 2014, **26**, 1485-1491.
140 J.W. Lee, D.J. Seol, A.N. Cho and N.G. Park, *Adv. Mater.*, 2014, **26**, 4991-4998.
141 F.C. Hanusch, E. Wiesenmayer, E. Mankel, A. Binek, P. Angloher, C. Fraunhofer, N. Giesbrecht, J.M. Feckl, W. Jaegermann, D. Johrendt, T. Bein and P. Docampo, *J. Phys. Chem. Lett.*, 2014, **5**, 2791-2795.
142 S.L. Lv, S.P. Pang, Y.Y. Zhou, N.P. Padture, H. Hu, L. Wang, X.H. Zhou, H.M. Zhu, L.X. Zhang, C.S. Huang and G.L. Cui, *Phys. Chem. Chem. Phys.*, 2014, **16**, 19206-19211.
143 N. Pellet, P. Gao, G. Gregori, T.Y. Yang, M.K. Nazeeruddin, J. Maier and M. Grätzel, *Angew. Chem. Int. Ed.*, 2014, **53**, 3151-3157.
144 H. Choi, J. Jeong, H.B. Kim, S. Kim, B. Walker, G.H. Kim and J.Y. Kim, *Nano Energy*, 2014, **7**, 80-85.
145 C. Wehrenfennig, M.Z. Liu, H.J. Snaith, M.B. Johnston and L.M. Herz, *Energy Environ. Sci.*, 2014, **7**, 2269-2275.
146 Y.Z. Ma, L.L. Zheng, Y.H. Chung, S.S. Chu, L.X. Xiao, Z.J. Chen, S.F. Wang, B. Qu, Q.H. Gong, Z.X. Wu and X. Hou, *Chem. Commun.*, 2014, **50**, 12458-12461.
147 S. Colella, E. Mosconi, P. Fedeli, A. Listorti, F. Gazza, F. Orlandi, P. Ferro, T. Besagni, R. Rizzo, G. Calestani, G. Gigli, F.D. Angelis and R. Mosca, *Chem. Mater.*, 2013, **25**, 4613-4618.
148 A. Abrusci, S.D. Stranks, P. Docampo, H.L. Yip, A.K. Jen and H.J. Snaith, *Nano Lett.*, 2013, **13**, 3124-3128.
149 F.D. Giacomo, S. Razza, F. Matteocci, A. D'Epifanio, S. Licoccia, T.M. Brown and A.D. Carlo, *J. Power Sources*, 2014, **251**, 152-156.
150 T. Leijtens, G.E. Eperon, S. Pathak, A. Abate, M.M. Lee and H.J. Snaith, *Nat. Commun.*, 2013, **4**, 2885.
151 M. Zhang, H. Yu, M.Q. Lyu, Q. Wang, J.H. Yun and L.Z. Wang, *Chem. Commun.*, 2014, **50**, 11727-11730.
152 J.H. Im, C.R. Lee, J.W. Lee, S.W. Park and N.G. Park, *Nanoscale*, 2011, **3**, 4088-4093.

153 Q. Wang, Y.C. Shao, Q.F. Dong, Z.G. Xiao, Y.B. Yuan and J.S. Huang, *Energy Environ. Sci.*, 2014, **7**, 2359-2365.
154 D.J. Lewis and P. O'Brien, *Chem. Commun.*, 2014, **50**, 6319-6321.
155 A.T. Barrows, A.J. Pearson, C.K. Kwak, A.D.F. Dunbar, A.R. Buckley and D.G. Lidzey, *Energy Environ. Sci.*, 2014, **7**, 2944-2950.
156 D.Q. Bi, S.J. Moon, L. Häggman, G. Boschloo, L. Yang, E.M.J. Johansson, M.K. Nazeeruddin, M. Grätzel and A. Hagfeldt, *RSC Adv.*, 2013, **3**, 18762-18766.
157 Y.Z. Wu, A. Islam, X.D. Yang, C.J. Qin, J. Liu, K. Zhang, W.Q. Peng and L.Y. Han, *Energy Environ. Sci.*, 2014, **7**, 2934-2938.
158 B. Conings, L. Baeten, C.D. Dobbelaere, J. D'Haen, J. Manca and H.G. Boyen, *Adv. Mater.*, 2014, **26**, 2041-2046.
159 K.N. Liang, D.B. Mitzi and M.T. Prikas, *Chem. Mater.*, 1998, **10**, 403-411.
160 J.J. Shi, Y.H. Luo, H.Y. Wei, J.H. Luo, J. Dong, S.T. Lv, J.Y. Xiao, Y.Z. Xu, L.F. Zhu, X. Xu, H.J. Wu, D.M. Li and Q.B. Meng, *ACS Appl. Mater. Inter.*, 2014, **6**, 9711-9718.
161 N.K. Noel, A. Abate, S.D. Stranks, E.S. Parrott, V.M. Burlakov, A. Goriely and H.J. Snaith, *ACS Nano* 2014, **8**, 9815-9821.
162 D.Q. Bi, L. Yang, G. Boschloo, A. Hagfeldt and E.M.J. Johansson, *J. Phys. Chem. Lett.*, 2013, **4**, 532-1536.
163 H. Zhang, Y.T. Shi, F. Yan, L. Wang, K. Wang, Y.J. Xing, Q.S. Dong and T.L. Ma, *Chem. Commun.*, 2014, 50, 5020-5022.
164 W.H. Nguyen, C.D. Bailie, E.L. Unger and M.D. McGehee, *J. Am. Chem. Soc.*, 2014, **136**, 10996-11001.
165 W.Z. Li, H.P. Dong, L.D. Wang, N. Li, X.D. Guo, J.W. Li and Y. Qiu, *J. Mater. Chem. A*, 2014, **2**, 13587-13592.
166 A. Krishna, D. Sabba, H.R. Li, J. Yin, P.P. Boix, C. Soci, S.G. Mhaisalkar and A.C. Grimsdale, *Chem. Sci.*, 2014, **5**, 2702-2709.
167 H.R. Li, K.W. Fu, A. Hagfeldt, M. Grätzel, S.G. Mhaisalkar and A.C. Grimsdale, *Angew. Chem. Int. Ed.*, 2014, **53**, 4085-4088.
168 P. Qin, S. Paek, M.I. Dar, N. Pellet, J. Ko, M. Grätzel and M.K. Nazeeruddin, *J. Am. Chem. Soc.*, 2014, **136**, 8516-8519.
169 W.B. Yan, Y.L. Li, W.H. Sun, H.T. Peng, S.Y. Ye, Z.W. Liu, Z.Q. Bian and C.H. Huang, *RSC Adv.*, 2014, **4**, 33039-33046.
170 J. Liu, Y.Z. Wu, C.J. Qin, X.D. Yang, T. Yasuda, A. Islam, K. Zhang, W.Q. Peng, W. Chen and L.Y. Han, *Energy Environ. Sci.*, 2014, **7**, 2963-2967.
171 N.J. Jeon, J. Lee, J.H. Noh, M.K. Nazeeruddin, M. Grätzel and S.I. Seok, *J. Am. Chem. Soc.*, 2013, **135**, 19087-19090.
172 P. Qin, H. Kast, M.K. Nazeeruddin, S.M. Zakeeruddin, A. Mishra, P. Bäuerle and M. Grätzel, *Energy Environ. Sci.*, 2014, **7**, 2981-2985.
173 J.A. Christians, R.C.M. Fung and P.V. Kamat, *J. Am. Chem. Soc.*, 2014, **136**, 758-764.
174 P. Qin, S. Tanaka, S. Ito, N. Tetreault, K. Manabe, H. Nishino, M.K. Nazeeruddin and M. Grätzel, *Nat. Commun.*, 2014, **5**, 3834.
175 G. Niu, W. Li, F. Meng, L. Wang, H. Dong and Y. Qiu, *J. Mater. Chem. A*, 2014, **2**, 705-710.
176 B. Kang, B.K. Rhee, G.T. Joo, S. Lee and K.S. Lim, *Opt. Commun.*, 2006, **266**, 203-206.
177 M. Ichiki and R. Maeda, *Appl. Phys. Lett.*, 2004, **84**, 395-397.
178 T. Choi, S. Lee, Y.J. Choi, V. Kiryukhin and S.W. Cheong, *Science*, 200, **324**, 63-66.
179 F.G. Wang, I. Grinberg and A.M. Rappe, *Phys. Rev. B*, 2014, **89**, 235105.
180 L. Jiang, I. Grinberg, F.G. Wang, S.M. Young, P.K. Davies and A.M. Rappe, *Phys. Rev. B*, 2014, **90**, 075153.
181 I. Grinberg, D.V. West, M. Torres, G.Y. Gou, D.M. Stein, L.Y. Wu, G.N. Chen, E.M. Gallo, A.R. Akbashev, P.K. Davies, J.E. Spanier and A.M. Rappe, *Nature*, 2013, **503**, 509-512.
182 W.L. Zhou, H.M. Deng, P.X. Yang and J.H. Chu, *Appl. Phys. Lett.*, 2014, **105**, 111904.
183 C.S. Chou, M.G. Guo, K.H. Liu and Y.S. Chen, *Appl. Energy*, 2012, **92**, 224-233.
184 Y.Y. Zhang, X.J. Li, M.Z. Feng, F.L. Zhou and J.Z. Chen, *Surf. Coat. Tech.*, 2010, **205**, 2572-2577.
185 D. Hwang, S.M. Jo, D.Y. Kim, V. Armel, D.R. MacFarlane and S.Y. Jang, *ACS Appl. Mater. Inter.*, 2011, **3**, 1521-1527.
186 L.J. Meng, C. Li and M.P. Santos, *J. Inorg. Organomet. Polym.*, 2013, **23**, 787-792.
187 C.S. Chou, F.C. Chou and J.Y. Kang, *Powder Technol.*, 2012, **215-216**, 38-45.
188 J. Chae, D.Y. Kim, S. Kim and M. Kang, *J. Ind. Eng. Chem.*, 2010, **16**, 906-911.
189 H. Wang, H.Y. Li, J.S. Wang, J.S. Wu, D.S. Li, M. Liu and P.L. Su, *Electrochim. Acta*, 2014, **137**, 744-750.
190 S.M. Yang, H.Z. Kou, H.J. Wang, K. Cheng and J.C. Wang, *Electrochim. Acta*, 2009, **55**, 305-310.
191 C.Y. Lin, Y.H. Lai, H.W. Chen, J.G. Chen, C.W. Kung, R. Vittal and K.C. Ho, *Energy Environ. Sci.*, 2011, **4**, 3448-3455.
192 F. Xu, M. Dai, Y.N. Lu and L.T. Sun, *J. Phys. Chem. C*, 2010, **114**, 2776-2782.
193 S.F. Shaikh, R.S. Mane and O.S. Joo, *RSC Adv.*, 2014, **4**, 35919-35927.
194 Y.F. Wang, K.N. Li, W.Q. Wu, Y.F. Xu, H.Y. Chen, C.Y. Su and D.B. Kuang, *RSC Adv.*, 2013, **3**, 13804-13810.
195 J.Z. Ou, R.A. Rani, M.H. Ham, M.R. Field, Y. Zhang, H.D. Zheng, P. Reece, S. Zhuiykov, S. Sriram, M. Bhaskaran, R.B. Kaner and K. Kalantar-zadeh, *ACS Nano*, 2012, **6**, 4045-40853.
196 R. Ghosh, Brennaman MK, Uher T, Ok MR, Samulski ET, McNeil LE, Meyer TJ, Lopez R. *ACS Appl. Mater. Inter.*, 2011, **3**, 3929-3935.
197 M.M. Jaculinea, C.J. Raj, H.J. Kim, A.J. Rajendran and S.J. Das, *Mater. Sci. Semicond. Process.*, 2014, **25**, 52-58.
198 S.S. Shin, D.W. Kim, D. Hwang, J.H. Suk, L.S. Oh, B.S. Han, D.H. Kim, J.S. Kim, D. Kim, J.Y. Kim, K.S. Hong, *ChemSusChem*, 2014, **7**, 501-509.
199 F.A. Guo, G.Q. Li and W.F. Zhang, *Int. J. Photoenergy,* 2010, 105878.
200 B.H. Li, Y.W. Tang, L.J. Luo, T. Xiao, D.W. Li, X.Y. Hu and M. Yuan, *Appl. Surf. Sci.*, 2010, **257**, 197-202.
201 D.W. Kim, S.S. Shin, S. Lee, I.S. Cho, D.H. Kim, C.W. Lee, H.S. Jung and K.W. Hong, *ChemSusChem*, 2013, **6**, 449-454.
202 S.S. Shin, J.S. Kim, J.H. Suk, K.D. Lee, D.W. Kim, J.H. Park, I.S. Cho, K.S. Hong and J.Y. Kim, *ACS Nano*, 2013, **7**, 1027-1035.
203 K.X. Jin, Y.F. Li, Z.L. Wang, H.Y. Peng, W.N. Lin, A.K.K. Kyaw, Y.L. Jin, K.J. Jin, X.W. Sun, C. Soci and T. Wu, *AIP Adv.*, 2012, **2**, 042131.

This journal is © The Royal Society of Chemistry 2012